THESIS FOR THE DEGREE OF DOCTOR OF PHILOSOPHY

Aqueous Metal-ion Batteries

Safe and Sustainable by Design

MARTIN KARLSMO

Department of Physics

CHALMERS UNIVERSITY OF TECHNOLOGY

Gothenburg, Sweden 2024

Aqueous Metal-ion Batteries
Safe and Sustainable by Design
MARTIN KARLSMO
ISBN 978-91-8103-042-6

Doktorsavhandlingar vid Chalmers tekniska högskola
Ny serie nr 5500
ISSN 0346-718X

Department of Physics
Chalmers University of Technology
SE-412 96 Gothenburg
Sweden
Telephone + 46 (0)31-772 1000

Cover: Splashing water by DALL·E 3

Printed by Chalmers digitaltryck
Gothenburg, Sweden 2024

Aqueous Metal-ion Batteries
Safe and Sustainable by Design

Martin Karlsmo
Department of Physics
Chalmers University of Technology

Abstract

Aqueous metal-ion batteries (AMIBs) are promising candidates for technically low-to-medium-demanding electrical applications and could in principle be used in tandem with high-performant lithium-ion batteries (LIBs) to save resources and invested capital. By using organic materials and avoiding the scarce, costly, and toxic transition metals found in LIBs (*e.g*. Ni/Co/Cu), the technology may become lower cost, more environmentally benign, and safer than today's alternatives, which altogether rhymes well with EU's critical raw materials directive highlighting risks of shortages and price spikes for traditional LIB materials.

In this thesis we explore the possibility of assembling unconventional AMIBs and hybrid supercapacitors by considering both the active and passive materials of the electrochemical cell. Sodium based technologies are the starting point, the materials used are primarily organic, and there is a pervading theme of finding remedies for the active material dissolution issue of aqueous electrolytes. The latter is addressed without resorting to common routes *e.g*. saturating the electrolyte with expensive fluorinated/perchlorate salts or incorporating organic co-solvents. Instead, other types of electrolyte concepts are suggested – with the intention to maintain the low-cost and sustainable aspects of aqueous batteries, new kinds of electrodes are made, and novel electrochemical full cells are created and studied with a wide range of analytical techniques to assess the behaviour, interplay, and performance of the cells and their constituents.

Keywords: aqueous electrolyte, aqueous battery, organic materials, all-organic, sodium-ion battery, hybrid supercapacitor, sodium-ion capacitor, PTCDA, PTCDI, Prussian blue

List of Publications

This thesis is based on the following papers:

I **High-performant all-organic aqueous sodium-ion batteries enabled by PTCDA electrodes and a hybrid Na/Mg electrolyte**
M. Karlsmo, R. Bouchal, and P. Johansson.
Angewandte Chemie International Edition **2021**, 60, 24709-24715.
https://doi.org/10.1002/anie.202111620

II **Sustainability and technical performance of an all-organic aqueous Na-ion hybrid supercapacitor**
M. Karlsmo and P. Johansson.
Batteries & Supercaps **2022**, 5, e202200306.
https://doi.org/10.1002/batt.202200306

III **Exploring the electrochemistry of PTCDI for aqueous lithium-ion batteries**
M. Karlsmo*, J. Brown*, A. Grimaud and P. Johansson.
Energy Storage Materials **2024**, 66, 103218.
https://doi.org/10.1016/j.ensm.2024.103218
*Shared first authorship

IV **Le Chatelier's principle enables stable and sustainable aqueous sodium/magnesium-ion batteries**
M. Karlsmo, T. Hosaka, and P. Johansson.
Journal of Materials Chemistry A **2024**, 12, 4029-4036.
https://doi.org/10.1039/D3TA06826A

V **A guanidium salt as a chaotropic agent for aqueous battery electrolytes**
J. Brown, J. Forero-Saboya, B. Baptiste, M. Karlsmo, G. Rousse, and A. Grimaud.
Chemical Communications **2023**, 59, 12266-12269.
https://doi.org/10.1039/D3CC03769J

List of publications not included in this thesis

VI **2021 Roadmap for sodium-ion batteries**
N. Tapia-Ruiz, A. R. Armstrong, H. Alptekin, M. A. Amores, H. Au, J. Barker, R. Boston, W. R. Brant, J. M. Brittain, Y. Chen, M. Chhowalla, Y-S. Choi, S. I. R. Costa, M. C. Ribadeneyra, S. A. Cussen, E. J. Cussen, W. I. F. David, A. V. Desai, S. A. M. Dickson, E. I. Eweka, J. D. Forero-Saboya, C. P. Grey, J. M. Griffin, P. Gross, X. Hua, J. T. S. Irvine, P. Johansson, M. O. Jones, M. Karlsmo, E. Kendrick, E. Kim, O. V. Kolosov, Z. Li, S. F. L. Mertens, R. Mogensen, L. Monconduit, R. E. Morris, A. J. Naylor, S. Nikman, C. A. O'keefe, D. M. C. Ould, R.G. Palgrave, P. Poizot, A. Ponrouch, S. Renault, E. M. Reynolds, A. Rudola, R. Sayers, D. O. Scanlon, S. Sen, V. R. Seymour, B. Silván, M. T. Sougrati, L. Stievano, G. S. Stone, C. I. Thomas, M-M. Titirici, J. Tong, T. J. Wood, D. S. Wright, and R. Younesi.
Journal of Physics: Energy **2021**, 3, 031503**.**
https://doi.org/10.1088/2515-7655/ac01ef

VII **Ten Ways to Fool the Masses when Presenting Battery Research**
P. Johansson, S. Alvi, P. Ghorbanzade, M. Karlsmo, L. Loaiza, V. Thangavel, K. Westman, and F. Årén.
Batteries & Supercaps **2021**, 4, 1785-1788**.**
https://doi.org/10.1002/batt.202100154

Contribution Report

I **I** designed the study and did all the measurements with the guidance and support of **R. Bouchal**. **I** did the formal analysis, validation, visualization, wrote the original draft, and together with **R. Bouchal** reviewed & edited the manuscript throughout the writing process. **R. Bouchal** participated in validating the results. **P. Johansson** was responsible for the general conceptualization, project administration, supervision of **me**, resources, and reviewed & edited the manuscript.

II **I** designed the study and did all the measurements, formal analysis, validation, visualization, and wrote the original draft. **P. Johansson** was responsible for the general conceptualization, project administration, supervision of **me**, resources, and reviewed & edited the manuscript.

III **I** designed the study with **J. Brown** and we did all the measurements except EQCM-R, formal analysis, validation, visualization, and wrote the original draft. **E. Bendadesse** did the EQCM-R measurements and participated in the subsequent analysis. **J-M. Tarascon** synthesized the LMO. **P. Johansson** and **A. Grimaud** were responsible for the general conceptualization, project administration, supervision, resources, and reviewed & edited the manuscript.

IV **I** designed the study and except from some of the Mn-PBA characterization did all the measurements, formal analysis, validation, visualization, and wrote of the original draft. **T. Hosaka** synthesized the Mn-PBA, did parts of the Mn-PBA characterization, participated in validating the results, and reviewed & edited the manuscript. **P. Johansson** was responsible for the general conceptualization, project administration, supervision of **me**, resources, and reviewed & edited the manuscript.

V **J. Brown** and **A. Grimaud** conceptualized the idea. **J. Brown** and **J. Forero-Saboya** devised and carried out the synthesis procedure, **J. Brown** did the IR and ESW measurements, **B. Baptiste** solved the crystal structure, and **I** carried out the viscosity measurements. All authors contributed to the analysis and wrote the manuscript together.

List of abbreviations

AC	Activated carbon
ALIB/ASIB/APIB/AMgIB	Aqueous lithium/sodium/potassium/magnesium-ion battery
AMIB	Aqueous metal-ion battery
AM	Active material
ATR	Attenuated total reflection
CE	Counter electrode
CB	Carbon black
CC	Current collector
CMC	Carboxymethyl cellulose
CV	Cyclic voltammetry
EIS	Electrochemical impedance spectroscopy
EOL	End-of-life
ESW	Electrochemical stability window
FSI	bis(fluorosulfonyl)imide
FTIR	Fourier-transform infrared
GC	Galvanostatic cycling
Gdm/$[Gdm]^+$	Guanidine/guanidinium
HER	Hydrogen evolution reaction
HSC	Hybrid supercapacitor
IoT	Internet-of-Things
LFP	Lithium iron phosphate, $LiFePO_4$
LIB/SIB/PIB/MgIB	Lithium/sodium/potassium/magnesium-ion battery
LMO	Lithium manganese oxide, $LiMn_2O_4$
LSV	Linear sweep voltammetry
NTP	Sodium titanium phosphate, $NaTi_2(PO_4)_3$
OER	Oxygen evolution reaction
OTF	Trifluoromethanesulfonate
PBA	Prussian blue analogue
PTCDA	Perylene-3,4,9,10-tetracarboxylic dianhydride
PTCDI	Perylene-3,4,9,10-tetracarboxylic acid diimide
PTFE	Polytetrafluoreten
PVdF	Polyvinylidene difluoride
RE	Reference electrode
SOC	State-of-charge
TFSI	bis(trifluoromethanesulfonyl)imide
WE	Working electrode
WISE/WIBE	Water-in-salt/bisalt electrolyte
XRD	X-ray diffraction

Table of Contents

1 | Introduction

Due to Europe's and United States' high energy consumption, in combination with the rapid economic growth in China in the past decades – emerging as the world's largest developing nation and energy consumer [1] – the electric consumption and carbon dioxide emissions are making all-time highs (Figure 1a) [2]. Meanwhile, to comply with the greenhouse gas emission goals set by the UN by 2030 [3], western governments are phasing out fossil fuels and are pushing for an increased amount of electrification, creating an ever-increasing demand for reliable and sustainable energy storage technologies.

Among various energy storage systems, rechargeable batteries offer one of the best combinations of energy efficiency, energy density, flexibility, and simple maintenance [4,5]. The current dominant technology, the lithium-ion battery (LIB), has since 1991 supplied energy for performance-requiring electrical applications and its versatility has undeniably been a success factor. Excellence does, however, often come with high costs, and LIBs are no exception. Costly materials & manufacturing (while rapidly declining [6]), ethically problematic resource origins [7], and safety concerns [8,9], all make LIBs non-ideal, yet it is arguably a most necessary technology with overall gains in combating pollution and fossil fuel consumption, not the least for electromobility [10,11].

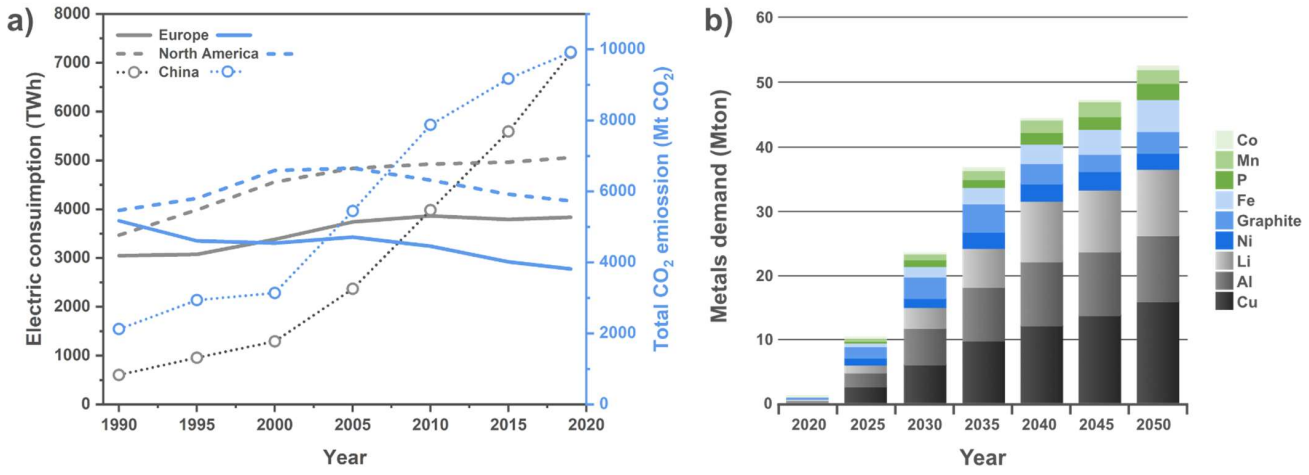

Figure 1. a) Electric consumption and total CO_2 emission by region from the International Energy Agency and b) annual metals demand from LIBs under Net Zero Scenario from BloombergNEF.

These electric vehicles and moreover portable devices have propelled battery R&D over the past decades, and today next generation batteries (post-LIBs) are gaining an increasing amount of attention with an even more diverse application market. Sodium-ion batteries (SIBs) and hybrid supercapacitors (Na-HSCs) are such aspiring candidates without most of the above resource issues and they offer both decreased cost, improved power performance, and the former at least have prospects of similar gravimetric energy densities [12]. By also implementing organic materials and aqueous electrolytes, a very cost-effective and sustainable energy storage device can be constructed as the cobalt & nickel-containing electrodes, copper & aluminium current collectors (CCs), and electrolytes with toxic salts & flammable organic solvents all are avoided [9,13]. This would render a device with low voltage (≤2 V), but not every application requires cell chemistries optimized for high voltage and high energy density. Some applications would in fact benefit from lower voltages, *e.g.*, Internet-of-Things (IoT) could do without built-in voltage converters if the electric source was at *ca.* 1.2-1.5 V [14,15], while larger scale (MWh-TWh) stationary installations, on- or off-grid, with completely different usage patterns might rather benefit from key performance indicators such

as safety, cost, and environmental impact – not only with respect to the materials but also to the battery production and total energy throughput [16,17]. The creation of such batteries/HSCs furthermore aligns with the EU's critical raw materials directive [18], raising awareness of potential future shortages and price spikes of *e.g.* cobalt, natural graphite, lithium, nickel, manganese, and copper, all of which comprise traditional LIBs, highlighting the need for new cell chemistries as the metals demand continues to grow (Figure 1b) [19].

R&D efforts to accomplish functional aqueous metal-ion batteries (AMIBs)/HSCs have, until now, never really incorporated a holistic view. Since 2015, extreme concentrations of primarily fluorine/perchlorate-based salts have been applied, creating a so-called "water-in-salt" electrolyte (WISE), to minimize the water concentration to overcome the issues of active material dissolution and low cell voltage [20] – simultaneously defeating the very purpose of aqueous batteries. We argue to fairly be promoted as sustainable, not only should the active materials be of such character, but the binder, separator, CCs, and electrolyte salt(s) should as well. By choosing the materials carefully, this approach would also alter the recycling and circular process. Ideally, not only are the cost and environmental impact greatly reduced as assembled, but more importantly, end-of-life (EOL) can be handled as *e.g.* organic waste and the battery could be thrown among food leftovers or in the compost to biodegrade.

1.1 Scope

This thesis focuses on and explores the possibility of combining organic materials and more benign transition metals (Fe/Mn) to construct unconventional AMIBs and HSCs with low-to-medium salt concentrated aqueous electrolytes, aimed primarily for IoT or stationary energy storage, with a focus on sodium based technologies and electrolytes. Although recent trends have been to incorporate co-solvents and polymerizing additives to the electrolyte, we refrain from such measures and instead aim to find alternative remedies for the chronic electrode active material dissolution issue with liquid aqueous media. We set out to study the behavior and interplay of different electrolytes, electrodes, and electrochemical full cells, with a wide range of analytical techniques; physico-chemical characterization, spectroscopy, diffraction, and most prominently electrochemical methods to assess the assembled cells and its constituents. Finally, we want to emphasize that even though this thesis has a sustainability focus, no such investigations were carried out (*e.g.* life cycle assessments), but it is rather argued for in terms of material choices and by the very design.

2 | Batteries & hybrid supercapacitors

"A container consisting of one or more cells, in which chemical energy is converted into electric energy and used as a source of power" is the Oxford Dictionary battery definition [21]. This definition can also be interpreted to include HSCs as they have one redox active Faradaic electrode, storing chemical energy, paired with one non-Faradaic electrode attracting charges electrostatically at the electrode surface.

2.1 Working principles and charge storage mechanisms

To avoid confusion, the anode/cathode terminology will not be used herein. Instead, the higher redox potential electrode in the redox couple will be referred to as the positive electrode and the lower will be referred to as the negative electrode, denoted as “negative electrode||positive electrode”. The fundamental concept of rechargeable batteries and HSCs is to physically separate these electrodes, and by connecting them through an electrical circuit electrons are allowed to flow externally while ions are shuttled in the electrolyte between the electrodes inside the device. To charge the cell, an electric source is applied, and electrons will flow through the external circuit. For charge neutrality to remain, ions will migrate in the electrolyte through the separator, from the positive to the negative electrode. At 100% state-of-charge (SOC), *i.e.* fully charged, a SIB’s hard carbon electrode has been filled, intercalated, and the metal oxide has been emptied, deintercalated, by cations. During discharge the ions and electrons flow back in a reversed manner performing useful work in the external circuit (Figure 2). One cycle has now passed, and the ion shuttling process is ready to be repeated back and forth in a rocking-chair motion.

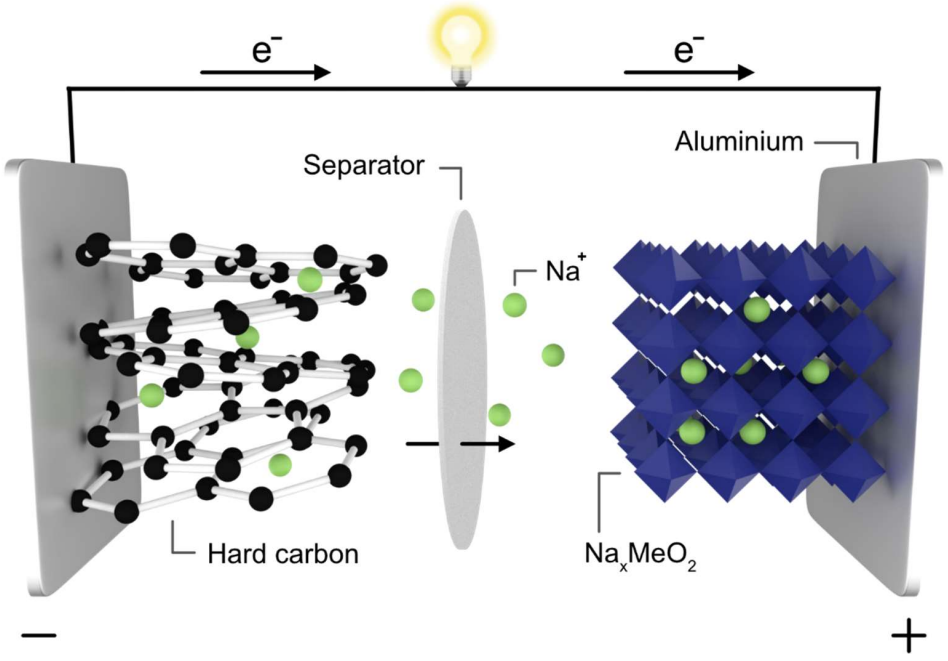

Figure 2. A SIB during discharge. Image originally by Dr. Matthew Sadd, edited and used with permission.

The typical SIBs are assembled using electrodes of hard carbon and layered transition-metal oxides (Na_xMeO_2, Me = Mn, Ti, Cu, Fe, Ni, Co *etc.*), both in contact with thin polymeric separators, wet with electrolytes made of the salt $NaPF_6$ dissolved in mixtures of ethylene carbonate and linear carbonates. The electrodes, composites of an active material, a conductive additive, and a binder, are coated on Al CCs which connects and closes the external circuit. With a $NaMnO_2$ positive electrode, the redox reaction would ideally occur as follows:

$$NaC_x + MnO_2 \rightarrow C_x + NaMnO_2, \quad (Eq.1)$$

which can be divided into an oxidation reaction

$$NaC_x \rightarrow C_x + Na^+ + e^-, \quad (Eq.2)$$

and a reduction reaction

$$Na^+ + e^- + MnO_2 \rightarrow NaMnO_2. \quad (Eq.3)$$

The amount of charge a battery cell can provide thereof relies on how many Na^+ the electrodes can accommodate and it is referred to as the capacity (Q) (C = As = $\frac{1000}{3600}$ mAh). In an ideal world, all the current in the external circuit originates from the redox reaction(s), and then $Q = I \cdot t$, where I (A) is the current and t (s) is the discharge time. The specific gravimetric capacity (mAh g^{-1}), capacity per electrode mass, from now on capacity, usually has more practical relevance and $NaMnO_2$ is able to theoretically accommodate 244 mAh g^{-1}.

If the redox reactions described above are to happen in an uninterrupted fashion, there needs to be a continuous flux of ions from the bulk electrolyte to the proximity of the electrode surface. This mass transport is primarily driven by diffusion, but also migration and convection, and the former can be described by Fick's first law [22]. In the one-dimensional case, for a certain species j,

$$J_j = -D_j \frac{\partial C_j(x)}{\partial x}, \quad (Eq.4)$$

where D_j is the diffusion coefficient, C_j is the concentration, and J_j (mol s^{-1} cm^{-2}) is the flux caused by diffusion, or in other words, the rate of mass transfer per unit of area normal to the direction of transfer. As this happens, an electrode potential will appear at the electrolyte-electrode interface, commonly referred to in the context of a redox couple M^+/M, where M^+ is the dissolved metal-ion and M is the solid metal/metal oxide. The movement of these charged species originate from the spontaneous redox reactions, accommodated by the electrodes, and the redox potential (used interchangeably with electrode potential [23,24]) could be described as the tendency of a chemical species to be reduced/oxidized; the affinity of gaining/losing electrons. A higher redox potential therefore means a higher affinity of gaining electrons.

In an electrochemical cell, the difference in electrode potential of the two electrodes, $E_{positive}$ (V) and $E_{negative}$ (V), is defined as the cell potential/voltage ΔV_{cell} (V). One often also encounters 'nominal voltage' which in refers to the average ΔV_{cell} of a cell throughout a discharge. Furthermore, the change in Gibbs free energy (ΔG) of the reaction is a function of the cell potential, according to:

$$\Delta G = -nF\Delta V_{cell} = -nF\left(E_{positive} - E_{negative}\right), \quad (Eq.5)$$

where n is the number of moles of electrons transferred and F is the Faraday constant ≈ 96485 C mol^{-1}. The energy (J) of the cell is then a function of the cell potential and capacity,

$$energy = \int \Delta V_{cell}(Q) dQ. \quad (Eq.6)$$

The convention is also for energy to be given in the energy per mass or volume, *i.e.* specific gravimetric energy or volumetric energy density. The specific gravimetric energy density (from now on energy density) E (Wh kg^{-1}) of a battery can be calculated according to

$$E = \frac{\int I\Delta V_{cell}(t)dt}{3.6m} \qquad (Eq.7)$$

from a discharge potential plot, where I (mA) is the discharge current, t (s) is the corresponding discharge time, and m (g) is the weight. The considered m often varies, but to be able to compare it is important to specify whether it is on active material-, cell-, or pack-level. Here, commercial SIBs by Faradion hold 160 Wh kg^{-1} and 290 Wh l^{-1} at the cell level [25].

HSCs on the other hand make use of the fast double layer charge storage mechanism at one of the electrodes [26]. During operation, by withdrawing/pushing electrons from/in the electrode, the electrode becomes charged, and oppositely charged electrolyte ions will form a surface layer to compensate. According to the Stern model [27], developed from prior models by Helmholtz and Guoy-Chapman, an inner compact Stern layer and an outer diffuse layer will form and screen charges off the surface (Figure 3). So far, this is considered the most accurate model and capacitances for flat surfaces can be gathered with high accuracy. It does, however, fall short of describing the real charge distribution of nanoporous supercapacitor electrodes, and there is still a lack of complete understanding how the ions behave in such small and confined spaces.

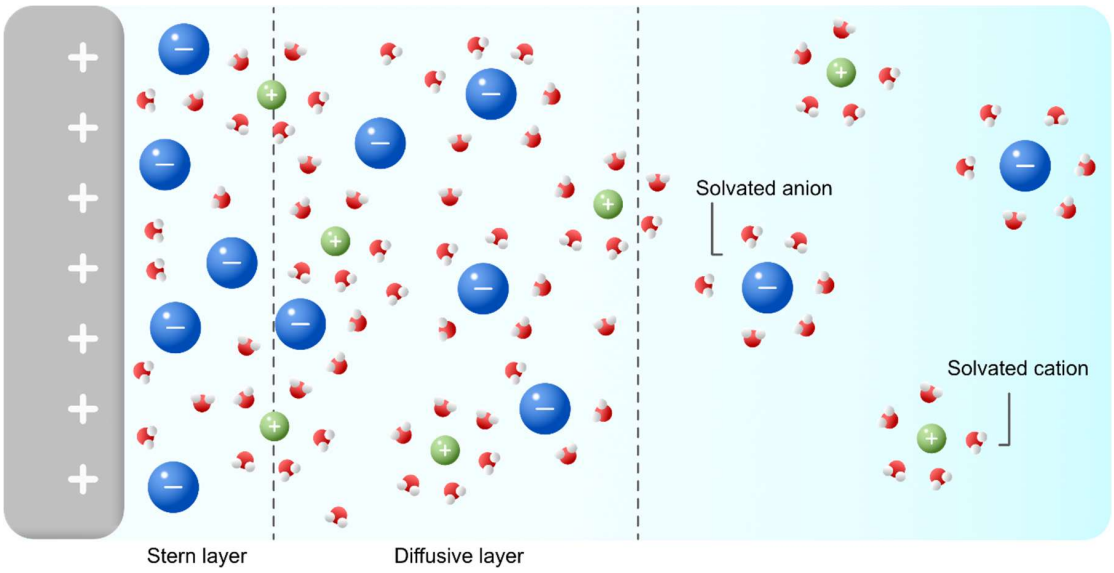

Figure 3. Stern model.

The performance measures for HSCs are calculated slightly different as compared to batteries. Here, specific gravimetric capacitance (C_{sp}) *can* be, and are sometimes used, instead of capacity,

$$C_{sp} = \frac{I}{m\left(\frac{d\Delta V_{cell}}{dt}\right)}. \qquad (Eq.8)$$

E and the specific gravimetric power density (from now on power density) (P) (W kg^{-1}) are thereafter calculated as follows,

$$E = \frac{C_{sp} \cdot V^2}{7.6}, \quad (Eq. 9)$$

and

$$P = \frac{E}{\Delta t} \cdot 3600, \quad (Eq. 10)$$

where V (V) is the discharge voltage range and Δt (s) is the discharge time.

The double layer mechanism is limited to the electrode surface area, compared with bulk electrode volume for Faradaic materials, which limits the number of charges stored and thus the energy density, but it opens the possibility for high power densities if paired with a redox-active electrode with fast charge-storage properties. This configuration can therefore achieve both relatively high energy densities and power densities as both Faradaic and non-Faradaic processes are employed simultaneously [28].

2.2 Sodium-ion batteries

The research field of next generation batteries is ever increasing and a substantial amount of work has been put into the 6th most abundant element in the crust of Earth, sodium [29,30]. SIBs were originally studied alongside LIBs in the 1970s and 1980s but were more or less abandoned the coming three decades due to the rapid advances of LIBs. During the past decade, however, the spotlight has been brought back to SIBs because of an increased sustainability awareness and in pursuit of more cost-effective energy storage solutions [12]. Several companies, including Northvolt with Altris, Faradion, CATL, Tiamat, Novasis Energies, and Natron Energy are developing SIBs [12,31], and recent years have demonstrated their practical viability for E-bikes, Sydney Water's Bondi Sewage Pumping Station, and a 30 kW/100 kWh energy storage power station in China [32,33].

SIBs offer better power densities (1000 *vs*. 400 W kg^{-1}), the prospect of similar gravimetric energy densities (currently 160 *vs.* 250 Wh kg^{-1}), but lower volumetric energy densities (290 *vs*. 700 Wh l^{-1}) as compared to LIBs [12]. The larger Na^+ (r_{Na+} = 1.02 Å, r_{Li+} = 0.76 Å) can also make insertion/extraction more difficult, and the host electrode sometimes undergoes significant volume changes which can lead to structural degradation that reduces the cycle life and performance of the battery [34]. However, the advantages of SIBs are manifold; mineral resources containing sodium are practically unlimited, geographically well distributed and therefore attainable at low cost [13]; neither natural graphite nor cobalt are needed for the electrodes; SIBs can be made with Al CCs on both sides, enabling 0 V cell discharge without CC dissolution, decreasing the material and shipping cost substantially [35]; and valuable knowledge and infrastructure already gathered and available for LIBs can easily be carried over to SIB manufacturing [36]. As a consequence, a considerable amount of intercalation materials have been explored, and at the positive side layered transition-metal oxides, polyanionic materials, Prussian blue analogues (PBAs), and organic materials have proven to perform well [12]. At the negative side, hard carbon is the most common, but Ti-based oxides, alloys, and 2D transition-metal dichalcogenides have also been applied. Finally, a standard SIB electrolyte is yet to be established, but apart from the LP30 sodium analogue (1 M $NaPF_6$ in EC:DMC), some promising routes include NaTFSI with reduced toxicity and high thermal stability and the non-fluorinated NaBOB, not the least combined with the non-flammable trimethyl phosphate [37].

2.3 Aqueous electrolytes

Even though the rapid success and commercialization of LIBs and SIBs, their organic electrolytes are costly, highly flammable, and hazardous with their ability to form toxic gases [9,38]. The salt synthesis using/producing fluorine itself is also non-environmentally friendly, costly, and potentially dangerous [8,39]. Owing to this, the aqueous electrolyte concept with water as solvent is thoroughly being explored for metal-ion batteries and HSCs, holding promise of greatly benefitting the cost, safety, and sustainability – not only in terms of raw materials but also due to the minimal requirements for manufacturing environments and limited management and protection system needed. The unique dielectric and fluid properties of water furthermore generates high ionic conductivities and low viscosities, important for higher power applications and indeed very suitable for HSCs.

Pioneering work in 1994 sets the date for the first aqueous battery using intercalation materials ($VO_2(B)||LiMn_2O_4$ with 5 M $LiNO_3$) [40], and since then a plethora of cell chemistries have been investigated. For a long time, SO_4^{2-} and NO_3^- were the most commonly used anions in the electrolyte for both aqueous lithium-ion batteries (ALIBs) and aqueous sodium-ion batteries (ASIBs), and for the latter 1 M $Na_2SO_{4(aq)}$ were typically employed with an electrochemical stability window (ESW) of *ca*. 2 V, a high ionic conductivity (100 mS cm^{-1}), a low viscosity (1.2 mPa·s), and compatibility with many electrode materials [41]. Resorting to aqueous electrolytes, however, does come with inherent challenges [42]. Many electrode active materials suffer from dissolution in aqueous electrolytes, leading to poor cycling stability, and moreover, the electrolytes' ESWs are most often set by the water splitting reactions, the hydrogen evolution reaction (HER) and the oxygen evolution reaction (OER), which limits the pool of available materials and the nominal cell voltage. A low cell voltage also implies a low energy density (Eq. 7), which can be interpreted as problematic as energy density typically is seen as one of the key performance indicators for energy storage technologies.

This rather niche subfield was reborn in 2015 when the community shifted from the typical 1 M electrolyte concentration to WISEs, introduced by Suo *et al*. [20]. By their definition the dissolved salt should outnumber water by volume and mass, and it has been highly effective in suppressing material dissolution and widening the ESW [43]. These WISEs/water-in-bisalt electrolytes (WIBE) are typically based on large sulfonamide or perchlorate anions, and the effect of suppressed electrode solubility can be explained by: *i*) the lower water concentration, *ii*) transport limitations by the higher viscosity (10-100x), *iii*) certain anions forming a hydrophobic protecting layer and *iv*) sometimes also decompose, forming a solid electrolyte interphase (SEI) that passivates the electrode [44], analogous to metal oxide layers in ambient air. The ESW is broadened by *i-iv*, but also due to: *v*) more tightly bound water molecules, now almost exclusively coordinated in the first solvation shells of the dissolved salt ions. Albeit their effectiveness, these electrolytes, which often have >20 m of fluorinated/perchlorate salts, come with drawbacks, including high costs, relatively low ionic conductivities which deteriorates the rate performance, high corrosivity, poor wettability, and they often require purging to remove oxygen and afterwards require a controlled environment; defeating many of the unique selling points of aqueous electrolytes [45]. There are a few low-cost Ac^-- and Cl^--based WISEs/WIBEs, yet, the alkaline environment of Ac^- is not compatible with some PBAs and Cl^- tend to be highly corrosive [46–49].

Anions play an important role in how aqueous solutions behave. This was observed very early on in macromolecular science where *e.g.* Franz Hofmeister characterized salts in terms of their minimum concentration to precipitate proteins from the electrolyte [50]. Some ions turn out to increase the solubility of solutes/proteins (salt in) while others decrease it (salt out). By arranging the ions in the order of most salting-out to the left and most salting-in to the right, the so called Hofmeister series is created (Figure 4).

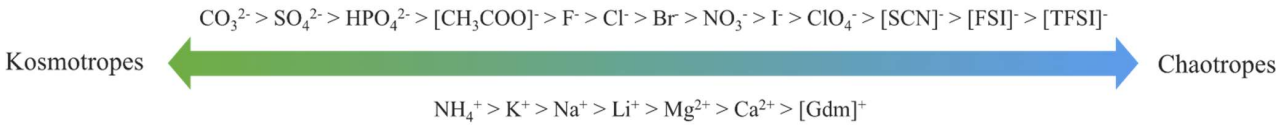

Figure 4. Typical Hofmeister series.

Later on, ions were grouped into kosmotropic structure makers, and chaotropic structure breakers, where the former are said to have the ability to order the hydrogen bonding network of the water molecules beyond their first solvation shell, whereas the latter do not possess this ability [51,52]. The high charge density of kosmotropes makes them more hydrated than chaotropes, salting-out proteins, but also more prone to ion pairing in solution which strengthens the hydrogen bonding network. Some recent studies goes against the notion that ions have an influence beyond the first solvation shell(s), but it is still an open question [53]. There seem to have been plenty of debate on the topic and a remaining 'elephant in the room' is the nature of the solute itself, which obviously has crucial role [54]. The series is empirical in nature, it depends on the experimental parameters and criteria used to define it and therefore the order is not entirely defined, but nevertheless it can be a useful tool when studying the effect of anions in aqueous electrolytes.

Adding organic compounds to the electrolyte, either as so 'co-solvents' or as non-solvent additives, are other types of electrolyte formulations lately proposed to reduce the salt concentration while maintaining the WISE effects. Here, polymers, small molecules, and organic solvents have been added, which effectively seem to minimize the free (non-ion-coordinating) water [55–61], and even enabling 2.5 V ALIBs [62,63]. Introducing additional components does, however, often compromise the favourable ionic conductivities and viscosities that is characteristic of aqueous electrolytes and can in some cases come with high cost. Moreover, with water weight percentages as low as 5% and with solidified polymer electrolytes, the aqueous and liquid nature of the electrolyte comes into question [56,64]. Therefore, we believe new electrolyte concepts are needed to address the issues of material dissolution, narrow ESWs, and costly salts/additives for AMIBs/HSCs.

2.4 Faradaic electrode materials

At the positive electrode side, some promising candidates which can reversibly accommodate Na^+ using aqueous electrolytes are polyanionic compound-containing units $(XO_4)^{n-}$ (X = P, S, Mo, etc.) with open 3D frameworks that allow fast conduction, Mn-based oxides with tunnel networks, organic materials, and PBAs with unique open framework-structures and often high redox potentials (Figure 5). Below, the capacity retention, X% capacity left of the initial capacity at cycle Y with a C-rate of Z, is written as X%@Y with ZC, and the capacity, energy density, and power density are based on the active material mass.

One of the earliest Faradaic positive electrodes, $Na_{0.44}MnO_2$, was investigated by Whitacre *et al*. in 2010 [65] with a relatively low capacity (45 mAh g^{-1}) using 1 M $Na_2SO_{4(aq)}$, and the AC||$Na_{0.44}MnO_2$ HSC showed an excellent cycling stability (*ca*. 97%@1000 with 4C). Another similar HSC, AC||λ-MnO_2 rendered 78 mAh g^{-1} and outstanding capacity retention (>100%@5000 with 6C) with the same electrolyte [66]. From now on 1 M $Na_2SO_{4(aq)}$ is used unless stated otherwise. Furthermore, Zhang *et al.* investigated the polyanionic $Na_3V_2(PO_4)_3$ (NVP) with roughly 70 mAh g^{-1} in the first cycle [67]. Many vanadium compounds, however, suffer from dissolution of V, resulting in large irreversible capacity losses and poor cycling stability [68], and here Zhang's electrode only retained <20%@50 with 10C. To try overcome this

issue, one of the V was substituted and $Na_2VTi(PO_4)_3$ managed to provide a higher initial capacity (93 mAh g^{-1}) and better capacity retention (77%@500 with 1C), although the latter is still not up to par [69]. $Na_3MnTi(PO_4)_3$ on the other hand showed promising stability with 58 mAh g^{-1} and 98%@100 with 1C (symmetric full cell) [70].

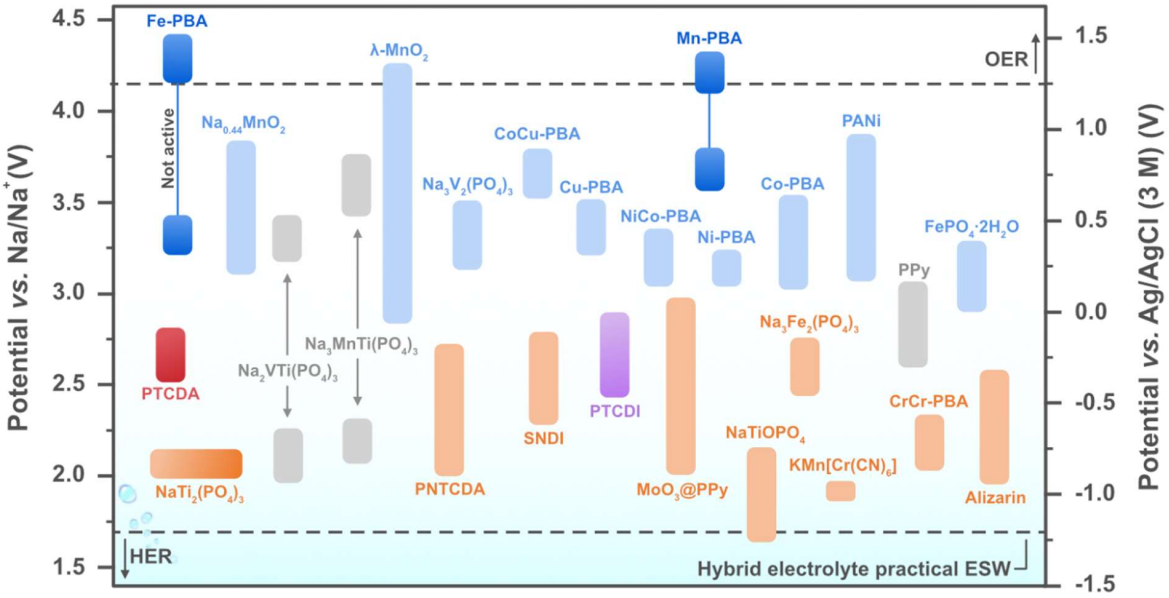

Figure 5. A selection of electrode materials used in aqueous Na-ion energy storage devices.

PBAs often display high capacity, high redox potential, and good cycling stability [71]. The larger sodium ions also fit better and more readily intercalates/deintercalates in the PBA structure, compared to Li^+, enabling good power performance and making them suitable for HSCs [72]. To name a few, Ni-, Co-, Cu-, and Cr-PBAs have been investigated with capacities up to 130 mAh g^{-1} using SO_4^{2-}-, NO_3^--, and ClO_4^--based aqueous electrolytes [26,73–77]. However, as aqueous devices are meant to be low-cost and environmentally friendly alternatives, scarce and costly transition-metal electrodes are not ideal, remembering the critical raw materials [18]. PBAs with more benign transition metals such as Fe and Mn have also been explored [78,79]. They accommodate *ca.* 110 mAh g^{-1} and 120-130 mAh g^{-1} split over two redox plateaus, respectively [76,80]. Reaching the high potential plateaus is, however, problematic, as they are situated slightly outside the ESW of most low-medium concentrated aqueous electrolytes. To be able to make use of both requires modifying the electrolyte to expand the ESW, meaning extreme amounts of salts or electrolyte additives, or applying HSC scan rates (>1 A g^{-1} or >10C) to avoid severely impacted Coulombic efficiencies due to unwanted OER. These PBAs are also prone to metal dissolution during cycling, which we herein aim to find more cost-effective solutions for to achieve stable cycling [**IV**].

The negative electrodes for ASIBs have most often been based on $NaTi_2(PO_4)_3$ (NTP) as active material [81]. The redox potential of NTP (around -0.8 V *vs.* Ag/AgCl (3 M)) is almost perfectly situated to maximally use the ESW, and due to its high capacity (120-130 mAh g^{-1}) it is the state-of-the-art ASIB negative electrode, where further advances have been relatively scarce [41]. Pristine NTP has poor electrical conductivity and cycling stability, but adding a carbon coating significantly improves both [82]. A lot of work has been done to further improve the cycling stability, *e.g.* He *et al.* synthesized hollow-structured NTP encapsulated in cross-linked porous N-doped carbon nanofiber with an great capacity retention

(97%@3000 with 5.5 A g^{-1} ≈ 41C) with a 1 M $NaClO_{4(aq)}$ "quasi-solid-state" gel electrolyte [83], while Zhang *et al.* cycled their NTP/C composite||AC Na-HSC at more reasonable rates, retaining 88%@2000 with 200 mA g^{-1} using a deaerated 1 M $Na_2SO_{4(aq)}$ [84]. More in depth investigations revealed that NTP and the lithium analogue $LiTi_2(PO_4)_3$ undergo chemical oxidation in its charged state in an oxygen-rich environment, rather than the wanted electrochemical process, and it seems to be the cause of the severe capacity fading [85,86]. Therefore, the question remains if NTP can perform well in liquid non-purged electrolytes.

Apart from NTP, metal oxide composites like MoO_3@PPy (33 mAh g^{-1}) [87], Mn-based PBAs (33 mAh g^{-1}) [74], and different organic materials have been applied. The latter have been given a fair bit of attention due to their promising qualities and the possibility to be produced by renewable sources such as biomass, as only using organic materials would alleviate most of the environmental and ethical concerns of the commercialized LIBs [88]. Such materials offer flexibility in design where the molecules can be tailored to achieve specific electrochemical properties depending on their structure and functional groups [89]. Unlike inorganics which often irreversibly transform, converted into several phases, and experience slow crystal lattice diffusivity with high charge density multivalent cations, organic materials tend to have simple and fast redox processes without any severe structural changes, with reversible electrochemical processes for ions of different sizes and charges [90]. Moreover, since both n-type, p-type, and bipolar (can be both n- and p-type) redox active organic materials exist, electrodes at both the negative and positive side can be constructed, and it is not uncommon for these batteries to come in the dual-ion class where anions also participate in the redox chemistry. A final attractive feature of most organic materials is their ability to biodegrade, which significantly simplifies the EOL as compared to the intricate recycling process of today's batteries [91].

Several small molecules are compatible with aqueous electrolytes and have been used as active materials, and in the cases when they tend to dissolve polymerization is an effective tool, as long as the inactive backbone weight fraction remains low. For example, the biomolecule alizarin, SNDI, 3CN-DPZ and several polyimides have been investigated as organic negative electrodes [92–97]. Yet, none of them offer any appreciable capacity in combination with long-term stability at battery C-rates. ≥10C were almost always applied, and slower (0.2-1C) discharge times is not only required by many practical applications, but cycling fast means less time spent at the electrolyte ESW edges, which could hide impaired Coulombic efficiencies and cycling stability issues. Still, it should be emphasized that these materials are very suitable choices for HSCs, and a perfect match with highly conducting aqueous electrolytes.

Perylene-type molecules are a family of organic compounds with excellent charge transport properties and cycling stability, *e.g.* perylene-3,4,9,10-tetracarboxylic acid diimide (PTCDI) [98] and perylene-3,4,9,10-tetracarboxylic dianhydride (PTCDA) [99–101] were originally applied as positive electrodes for non-aqueous LIBs/SIBs, and later on as negative electrodes with aqueous electrolytes [102–108]. They are essentially small units of graphene, and for aqueous electrolytes common remedies, again, have been to apply WISEs and/or high C-rates to overcome the issue of active material dissolution. Despite PTCDI's previous successful implementation in ASIBs, aqueous potassium-ion batteries (APIBs), and aqueous magnesium-ion batteries (AMgIBs) [102–105], its use in ALIBs remains unexplored. Similarly, PTCDA was used with APIBs, AMgIBs, and hydronium-ion batteries, but never with sodium-ion conducting electrolytes [106–108]. Herein, we therefore explore the electrochemistry and the possibility to use PTCDI for ALIBs and PTCDA for ASIBs/Na-HSCs, while avoiding extreme amounts of fluorinated/perchlorate salts in the electrolyte, with the aim to find negative electrodes with high cycling stability [**I-IV**].

2.5 Electrochemical full cells

The final step on the sustainability ladder is arguably to limit all parts of the energy storage device to sustainable materials, preferably mainly/entirely from renewable resources [109]. So far, it seems the battery community has stuck with the passive materials known to work well, and where most of the research, understandably, have been focused on the active materials. Yet to be promoted as *e.g.* all-organic, not only should the active materials be of such character (the current convention), but we also argue the passive binders, separators, CCs should as well, especially if one is to consider biodegradability at EOL. Indeed, there are great possibilities to create all-organic batteries/HSCs due to the versatility of organic materials; instead of the costly and most commonly used binder PVdF, that is fluorinated and requires the costly, toxic, and carcinogenic solvent N-methyl-2-pyrrolidone [110], it is possible to use carboxymethyl cellulose (CMC) with water in the electrode slurry. The slurry can subsequently be coated onto carbon-based substrates instead of expensive metal foils demanding mining [111]. Finally, the glass fibre or polyolefin based (oil-derived) separators laden with large environmental footprints can be replaced with cellulose filter papers [112]. To the best of our knowledge, this has not been done before and while it would render a rather unconventional device, it still has the same working principles and would come with severely less environmental impact & resource requirements.

These devices are, as mentioned earlier, assembled either with one or two Faradaic electrodes. The former is advantageously chosen if a higher power density is sought after, paired with a non-Faradaic electrode to create a HSC. In a patent from 1954 H.I. Becker describes what will become the most commonly used non-Faradaic electrode material for electric double-layer capacitors (EDLCs) and HSCs; AC [113]. The success of AC is a result of its extremely high specific surface area (*ca.* 500-3000 m^2 g^{-1}), high conductivity, low cost, and compatibility with most electrolytes [114]. The EDLC charge storage mechanism does, however, limit the capacity of AC to *ca.* 30-45 mAh g^{-1} [84,115], and therefore they are not suitable for energy density requiring applications. Other carbon based non-Faradaic electrodes have been applied to create EDLCs/HSCs, but due to intricate synthesis routes they are rarely commercially available. For example, carbon microspheres were used together with the polyimide PNTCDA to create a very high performant 'all organic' Na-HSC, assembled with PTFE binder, glass fibre separators, stainless steel CCs, and 17 m $NaClO_{4(aq)}$ having 65 Wh kg^{-1}, 20 kW kg^{-1} and 86%@1000 with 1 A g^{-1} [95]. The authors do, however, attribute the excellent performance to the high electrolyte concentration, which increases the Na^+ activity and thereby enhances the reaction kinetics, as PNTCDA in 5 m and 10 m $NaClO_{4(aq)}$ did not perform as well. With the more holistic mindset in mind, we in paper **II** explore the concept of creating an *all*-organic aqueous Na-HSC with PTCDA and AC, and furthermore evaluate its biodegradable abilities.

Moving on to the actual batteries there are few that are all-organic and aqueous, but one that performs well is a PNTCDA||PTPAn chemistry with a PTFE binder, Ti/Ni CCs, and 21 m $LiTFSI_{(aq)}$ having 53 Wh kg^{-1} and 85%@700 with 0.5 A g^{-1} [116]. Considering regular AMIBs, there are frankly more that have been studied than possible to mention, so to limit ourselves we will also here focus on ASIBs. Some of the earlier examples include NTP||NVP with 36 Wh kg^{-1} and an awful capacity retention due to V dissolution [117], whereas $Na_3MnTi(PO_4)_3$ had 40 Wh kg^{-1} in a symmetric configuration and 98%@100 with 1C [70]. NVP was later used with a 17 m $NaClO_4$ + 2 m sodium trifluoromethanesulfonate (NaOTF) hybrid electrolyte, also in a symmetric cell, significantly improving the performance (70 Wh kg^{-1}, 87.5%@100 with 1C) [118]. Furthermore, the popular PBAs have been used to create many ASIBs, *e.g.* NTP||Ni-PBA had 43 Wh kg^{-1} and 88%@250 with 5C using a N_2 purged 1.0 M $Na_2SO_{4(aq)}$ [119], and when applied with WISEs/WIBEs these batteries tend to be the state-of-the-art, with energy densities reaching 80 Wh kg^{-1} and relatively stable long-term cycling [76,120] (Figure 6). To slightly expand the scope from only organic materials, we in paper **III** and **IV** allow ourselves to incorporate the more benign metals Fe/Mn in the positive electrodes,

while keeping the holistic mindset for the rest of the battery constituents with the aim to create more sustainable and lower cost AMIBs.

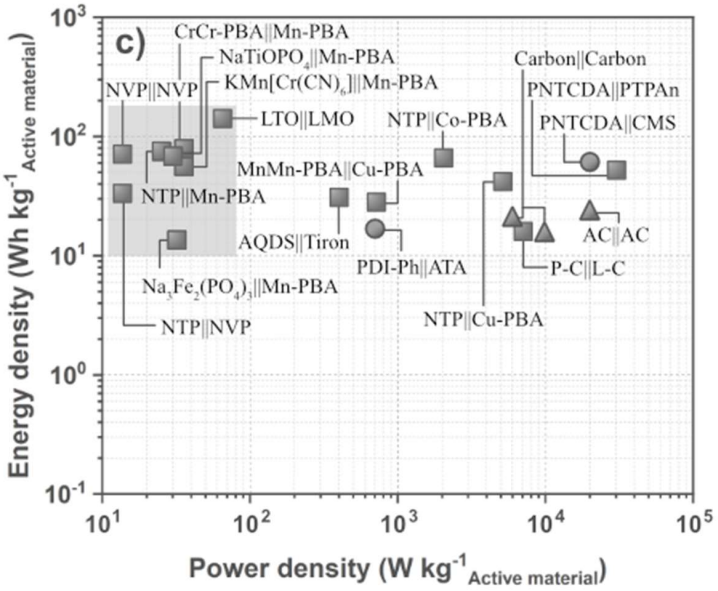

Figure 6. Ragone plot of aqueous metal-ion: batteries (square), HSCs (circle), and supercapacitors (triangle). The grey area papers did not report a powder density.

3 | Experimental

Empiricism and the scientific method date to ancient Greece but were more widely advocated in the 16-17th Centuries by philosophers such as Francis Bacon, Thomas Hobbes, and David Hume. This intellectual movement which culminated in the Enlightenment arguably set the Western world on a trajectory towards scientific advances, societal prosperity, and a standard of living earlier kings would have dreamt of. It is therefore a privilege for a battery PhD student – standing on the shoulders of giants – to continue the scientific tradition and to perform experimental work. This chapter sets out to describe said work; the materials and cells used and created, and moreover the physico-chemical, material, and electrochemical analyses applied to characterize the properties of the electrolytes, the electrode materials, and the assembled cells.

3.1 Materials synthesis

To synthesize guanidine bis(trifluoromethanesulfonyl)imide (GdmTFSI), 0.0104 mol lithium bis(trifluoromethanesulfonyl)imide (LiTFSI) (99.9% extra dry, Solvionic) and 0.0052 mol guanidine sulfate (Gdm_2SO_4) (99%, Sigma-Aldrich) were dissolved in the minimum volume of water in separate vials, after which the LiTFSI solution is added dropwise under stirring into the Gdm_2SO_4 forming a cloudy solution. This solution is dried, forming a white precipitate containing a mixture of GdmTFSI and Li_2SO_4. Acetone (10 ml, extra dry, Alfa Aesar) is added to the mixture and stirred for 1 h, after which this mixture is filtered. The filtrate, containing GdmTFSI, is rotary evaporated under vacuum to form a cloudy ionic liquid which, once cooled, crystallizes to form the final product, and this is finally dried under vacuum overnight with a yield of 97%.

$LiMn_2O_4$ (LMO) active material powder was prepared according to [121] by heating at 800°C a stoichiometric mixture of Li_2CO_3 (5% excess) and MnO_2 in air for 24 h, followed by two successive grinding and identical annealing sequences. The samples were cooled at a rate of 2°C min^{-1} until 300°C to ensure the proper oxygen stoichiometry.

Mn-PBA was synthesized by a chelate-assisted precipitation method according to a previous study [122]. In short, 4 mmol $Na_4Fe(CN)_6 \cdot 10H_2O$ and 4 mmol $MnCl_2 \cdot 4H_2O$ were dissolved separately in 100 ml 0.2 M sodium citrate solutions. The two solutions were mixed by dropping the $MnCl_2$ solution at 0.5 ml min^{-1} into the $Na_4Fe(CN)_6$ solution with magnetic stirring under N_2 atmosphere at room temperature. After stirring for 15 h, the precipitate was centrifuged, filtered, and washed thoroughly with 400 ml of deionized water. The final product was obtained after vacuum drying at 100 °C for 24 h.

3.2 Electrolyte preparation, electrode fabrication & cells

Sodium sulfate (Na_2SO_4) (anhydrous, ≥99%), magnesium sulfate ($MgSO_4$) (anhydrous, ≥99.5%), manganese(II) sulfate monohydrate ($MnSO_4 \cdot H_2O$) (≥99%), lithium sulfate (Li_2SO_4) (anhydrous, 99.5%), magnesium acetate tetrahydrate ($MgAc_2 \cdot 4H_2O$) (≥98%), Gdm_2SO_4, sodium acetate (NaAc) (anhydrous, ≥99.5%), and sodium nitrate ($NaNO_3$) (≥99%), all purchased from Sigma-Aldrich, as well as sodium bis(fluorosulfonyl)imide (NaFSI) (99.9%, Solvionic), sodium bis(trifluoromethanesulfonyl)imide (NaTFSI) (99.5%, Solvionic), LiTFSI, and GdmTFSI, were used to create the electrolytes. The hybrid electrolytes and the triple electrolyte (1.9 m Na_2SO_4 + 2.4 m $MgSO_4$ + 0.3 m $MnSO_4$) were prepared by

first dissolving Na_2SO_4 or LiTFSI in ultra-pure water (Millipore® Direct-Q® Purification, 18.2 MΩ·cm at 25°C), before adding the 2nd salt, and for the latter finally also $MnSO_4$, all in magnetically stirred vials at *ca.* 50°C.

An electrode preparation usually starts with a slurry in which the materials are mixed, before being coated onto a CC. In this thesis, the graphite foil (SGL Carbon) CC-supported electrodes were made by mixing AMs (PTCDA (97%, Sigma-Aldrich), PTCDI (≥94%, Thermo Fisher Scientific), Mn-PBA, Fe-PBA (Fennac, Altris), NTP (CIC energiGUNE) and washed AC (see below) (Darco G-60, 600 $m^2 g^{-1}$, J.T. Baker) with carbon black (CB) (Ketjenblack EC-300J or Super-P, Alfa Aesar), a conductive additive, using a pestle and mortar, before being added into aqueous solutions of 3 wt% carboxymethyl cellulose (CMC) (Sigma-Aldrich) binder, and stirred for 12 h. The slurries were then cast onto graphite foil using a Doctor blade (200-400 µm wet thickness) followed by vacuum drying at 60°C for 12 h. 10-14 mm Ø electrodes were punched out with an electrode weight ratio AM:CB:CMC of 75:15:10 and with 0.8-4 mg cm^{-2} active material loading. Working electrodes (half-cells), positive electrodes (full cell), and negative electrodes (full cell) typically have 0.8-2 mg cm^{-2} loading, while counter electrodes for half-cells were made heavier.

In most cases, free-standing AC counter electrodes (CEs) were used for the half-cells, and they were made by first stirring AC for 12 h in 1 M $HNO_{3(aq)}$, before washing with excessive amounts of ultra-pure water in a vacuumed Büchner funnel, followed by vacuum drying at 100°C for 12 h. The dried AC was mixed with CB and 3-4 ml ethanol and put on a stirring hot plate, following the procedure described by Brousse *et al.* [123]. While stirring, PTFE (60 wt% aqueous dispersion, Sigma-Aldrich) was slowly added, and the solution was thereafter left until the solvent had evaporated. The resulting paste was kneaded and spread with a few ml of ethanol until it became a firm homogeneous film. The free-standing electrodes were dried in an oven at 80°C for 12 h with a resulting thickness of *ca.* 400 µm, an active material loading of 10-12 mg cm^{-2}, and a 75:15:10 AC:CB:PTFE weight ratio.

The freestanding PTCDI, $LiFePO_4$ (LFP, Umicore), and LMO electrodes were prepared using the Bellcore method. Active material, carbon super P (Csp, Timcal), and poly(vinylidene fluoride)-co-hexafluoropropylene (PVdF-HFP) (Solvay) in a ratio of 73:9:18 were hand ground and mixed in acetone to form a slurry. Dibutyl phthalate (DBP, 99% Sigma-Aldrich) was added as a plasticizer and the slurry was heated at 50°C under stirring. Then, the as-prepared slurry was poured into a 7 cm^2 petri dish and left to dry to form a film. The film was washed three times in diethyl ether (99% min, Alfa Aesar) and dried at 60°C under vacuum. Resulting loadings were generally: PTCDI = 4-6 mg cm^{-2}, LFP = 20 mg cm^{-2} and LMO = 4-6 mg cm^{-2}.

3-electrode Swagelok cells (Figure 7) were assembled and used in both the half-cell and the full cell configurations, to enable monitoring of all electrode potentials, with Whatman cellulose filter separators (Grade 44, Sigma-Aldrich), and glassy carbon rods (HTW Hochtemperatur-Werkstoffe GmbH) to avoid corrosion. Coin-cells (CR2032) were also used for 2-electrode full cell and half-cell characterizations to ensure a more controlled environment and a constant applied pressure. They were mostly used for the long-term cycling stability tests.

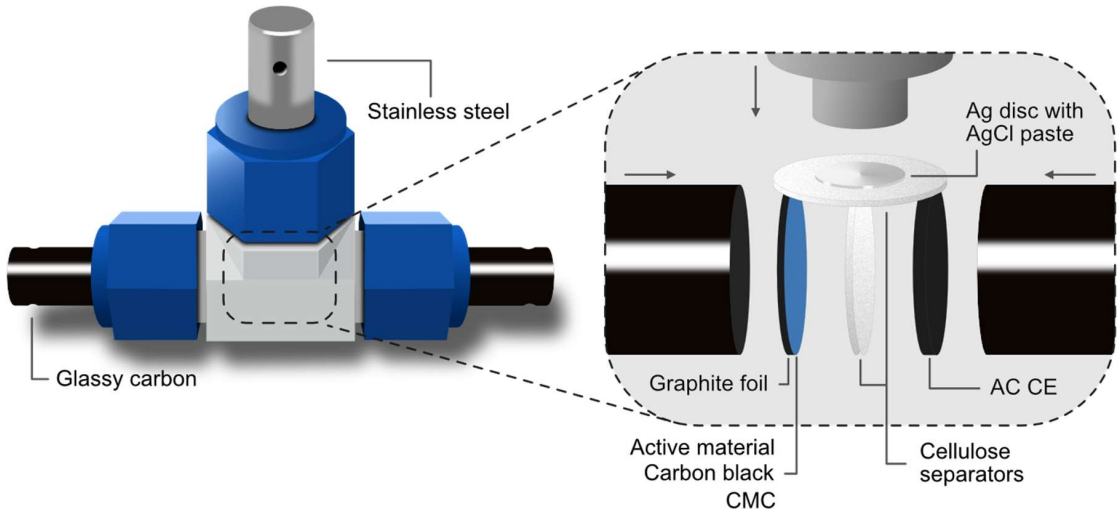

Figure 7. A typical half-cell setup using a 3-electrode Swagelok cell.

The potential is difficult to measure on an absolute scale, and it is therefore often given relative to a known redox couple. Herein, we use a Ag/AgCl pseudo reference electrode (Ag/AgCl from here on) (RE) (5 mm Ø, 0.127 mm silver foil, Alfa Aesar/AgCl ink, ALS Japan) *ca*. 0.34 V *vs.* Ag/AgCl (3.4 M KCl, Leakless Ag/AgCl Reference Electrode, eDAQ) since Ag/AgCl is a well-known and commonly used redox couple for aqueous electrolytes. Moreover, the electrochemical techniques described in the coming chapters; cyclic voltammetry (CV), linear sweep voltammetry (LSV), galvanostatic cycling (GC), and electrochemical impedance spectroscopy (EIS), were all done at room temperature (*ca* 22°C) on a Biologic VMP3 multichannel potentiostat/galvanostat, or for the GC also on a Scribner Associates Incorporated 580 Battery Test System.

LSV was carried out using a beaker cell (Figure 8) with a flat, polished, glassy carbon WE (1.2 mm Ø), a platinum wire CE, and an Ag/AgCl (3 M NaCl) or Ag/AgCl (3.4 M KCl, Leakless) submerged in 2 ml electrolyte. Voltammograms were gathered at a scan rate of 1 mV s^{-1} and the current density limit for the ESW was set to 1 mA cm^{-2}. The ESW gathered from this cell naturally differs from a practical cell, but it is used to standardize the ESW and enable a better comparison between different electrolytes – especially comparing different cations, as few (if any) active materials are redox active and compatible with all of the commonly used metal-ion electrolytes (Li, Na, K, Mg, Ca, *etc*.).

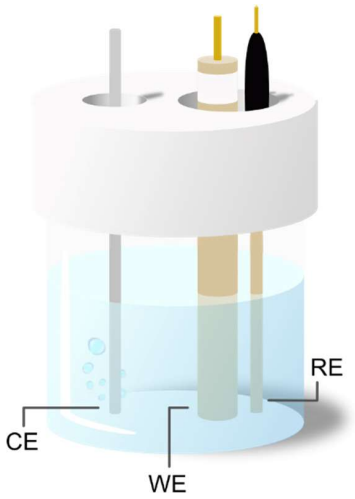

Figure 8. LSV cell set-up.

For the *in situ* electrochemical quartz crystal microbalance (EQCM-R) measurements, a NMP based slurry (73:18:9 PTCDI:Csp:PVdF wt%) was prepared and sonicated to ensure homogenous particle dispersion. The solution was sprayed onto golden 9 MHz QCM resonators (BioLogic) and during the spraying process heated to 150°C to evaporate the solvent, followed by heating to 200°C for 30 min to melt the binder for good film cohesion. The resonators, acting as the WE was mounted in an airtight EQCM cell developed previously [124], with a Pt-rod coated Bellcore LFP CE, a Ag/AgCl (saturated K_2SO_4) RE, and 2 ml electrolyte. The electrochemistry was carried out using a S2 Biologic SP200 workstation coupled with a SEIKO QCM922A microbalance permitting resonance frequency (f) monitoring during cycling, at scan rates of 5 mV s^{-1} between −1.0 V and 0.15 V *vs*. Ag/AgCl. The Sauberey equation was used when $\Delta f/\Delta R_m >$ 25 Hz/Ω [124,125]:

$$\Delta m = -\frac{A\sqrt{\rho_g \mu_g}}{f_0^2}\Delta f = -C_f \Delta f, \qquad (Eq.11)$$

where A is the piezoelectrically active area (0.196 cm^2), ρ_q is the quartz density (2.648 g cm^{-2}), μ_q is the quartz crystal shear modulus (2.947 × 1011 g cm^{-1} s^{-2}), and C_f is the sensitivity coefficient/calibration constant (1.23 ± 0.03 ng Hz^{-1}) determined previously [125]. The estimation of the mass per electron (*MPE*) is taken from the slope in a Δm *vs.* ΔQ plot, where $MPE = \frac{nF\Delta m}{\Delta Q \Delta}$ and F is the Faraday constant and n is the number of electrons.

3.3 Physico-chemical characterization

3.3.1 Densitometry and viscometry

With an Anton Paar DMA 4500 M densitometer the densities (ρ) of the electrolytes were measured using the oscillating U-tube method. In short, a U-shaped tube is set in motion by a piezoelectric actuator and depending on the mass of the electrolyte the tube is filled with, the tube resonates at different eigenfrequencies. By having a fixed volume, the ρ can easily be derived. Adjacent to the densitometer, a

Rolling-ball Lovis 2000 ME viscometer is coupled, working in conjunction. By filling a glass capillary with electrolyte and a metal ball, the speed of the ball is then measured as it rolls through the tilted capillary at varying angles. By having a small, spherical ball with smooth surfaces, the Reynolds number will be low, resulting in laminar flow, and the drag force on the ball can be approximated by Stokes' law,

$$F_d = 6\pi r\eta v, \qquad (Eq.12)$$

derived by solving the Navier-Stokes equations at the Stokes flow limit, where r is the ball radius, η is the electrolyte viscosity, and v the ball velocity. To solve for η, the gravitational force acting on the ball F_g is set to the drag force F_d, and by avoiding bubbles in the capillary, the ρ and η can be measured simultaneously at varying temperatures. Finally, they are usually depicted using Arrhenius plots (Figure 9) in which their temperature dependencies are visualized.

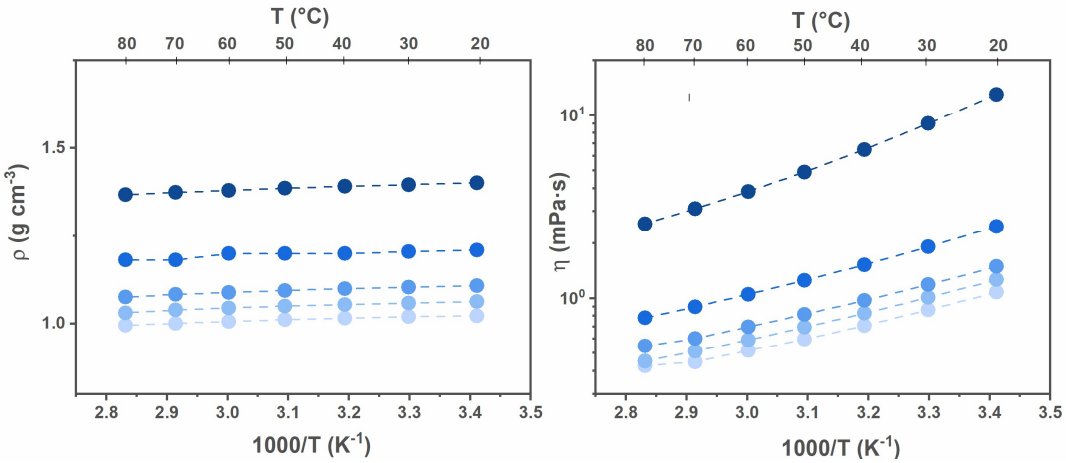

*Figure 9. Density and viscosity Arrhenius plots of Na_2SO_4 based aqueous electrolytes [**I**].*

3.3.2 Ionic conductivity

The ionic conductivities (σ) were measured using a Mettler-Toledo SevenCompact S230 conductivity meter with a 12 mm InLab® 710 Cond probe with 4 Pt poles conductivity cell (±0.5%), temperature controlled by a home-built thermoelectric set-up. The σ of an electrolyte originates from the ionic species physically migrating in the solvent, where the main transport mechanism, diffusion, arises from the concentration gradient caused by the electrodes acting as cation sources/sinks during charge and discharge. Moreover, cations such as Na^+ and Mg^{2+} have a strong affinity to water molecules which result in solvation/hydration shells around the ion in aqueous solutions. This intermolecular structure is relatively stable and will diffuse as one large unit during transport, a so-called vehicular transport mechanism [126]. The system can be approximated by the Stokes-Einstein relation for the diffusion coefficient [22],

$$D_j = \frac{k_b T}{6\pi r\eta} \qquad (Eq.13)$$

where r is the radius of the solvation shell (hydrodynamic/Stokes radius) and k_B the Boltzmann constant ≈ 1.380694×10^{-23} J K^{-1}. Similar to the ρ and η, σ is also often visualized using an Arrhenius plot (Figure 10a).

Another commonly used metric, the molar conductivity (Λ) of the electrolyte, can be calculated by dividing the measured σ by the molar concentration (M). Since dilute concentrations are accompanied by fewer ion

associations, the conductivity offered by one mol salt is usually higher for lower concentrations, as the relative amount of active charge carriers is higher, or in other words, the ionicity (α) is higher. By combining the η and the Λ of the electrolyte, an empirical rule by P. Walden concerning ions in solutions suggests that the product of the above is approximately constant for the same ions in different solvents [127],

$$\eta\Lambda = k. \qquad (Eq.14)$$

The Walden product k is a temperature-dependent constant and quantifies the ion motion relative to the media fluidity and the ionicity, where the latter is defined as

$$\alpha = \frac{\Lambda}{\Lambda_{N.E.}}. \qquad (Eq.15)$$

Here, $\Lambda_{N.E}$ is the molar conductivity calculated by the Nernst-Einstein relation without ionic correlations,

$$\Lambda_{N.E.} = \frac{F^2}{RT}(v_+ z_+^2 D_+ + v_- z_-^2 D_-), \qquad (Eq.16)$$

and F is the Faraday constant, R is the gas constant ($= k_b \cdot N_A$), T is the temperature, v_+ and v_- are the number of cations and anions per electrolyte formula unit, z_+ and z_- are the valences of the cations and anions, and D_+ and D_- are the diffusion coefficients of the cations and anions, respectively [128]. By inserting the Stokes-Einstein diffusion coefficient (Eq. 13) in the Nernst-Eisenstein relation (Eq. 16) the Walden product is now expressed as a function of the ionicity, the hydrated ion size, and the ion valency:

$$k = \eta\Lambda = \alpha\frac{F^2}{6\pi}\left(\frac{v_+ z_+^2}{r_+} + \frac{v_- z_-^2}{r_-}\right). \qquad (Eq.17)$$

By plotting Λ vs. η in a log-log scale, a Walden plot is made and the relationship between the electrolytes' molar conductivities and viscosities can be deciphered, by qualitatively visualizing their ionicities and classifying their ion conducting behaviour (Figure 10b). Far below the ideal KCl line are non-ionic, under the ideal line are poor-ionic, on the ideal line are good-ionic, and upper left, above the KCl line, are superionic liquids [129].

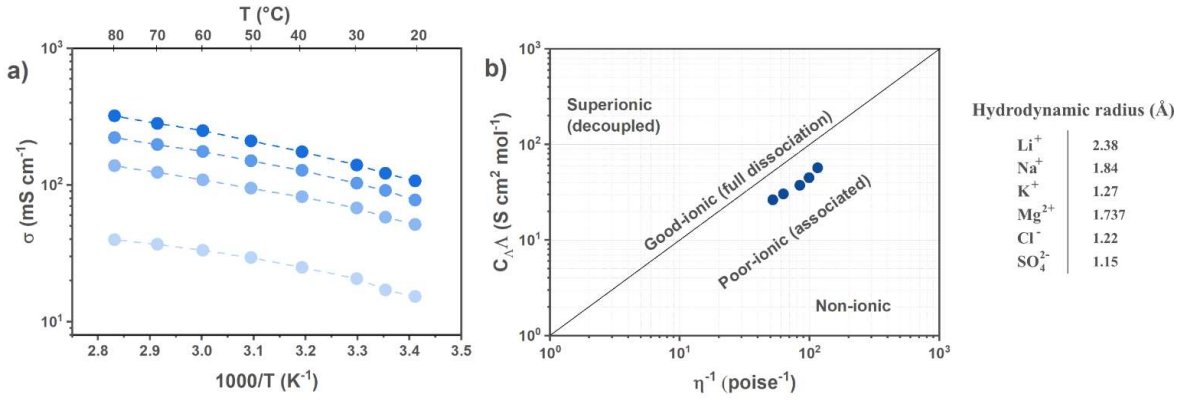

*Figure 10. a) Ionic conductivity Arrhenius plot, b) a Walden plot of Na_2SO_4 based aqueous electrolytes, and hydrodynamic radii in aqueous solution [**I**].*

Comparing electrolytes with mono- and divalent salts, however, is not trivial. It is possibly not even the intended use of the Walden rule. Nevertheless, Yang *et al*. applied a methodology for a more fair comparison when ions of different charge are present, where the ideal line of each electrolyte is shifted by a prefactor $C_A = k/k_{KCl}$, using k from Eq. 17 where $k_{KCl} = [\nu_+=1, z_+^2=1, \nu_-=1, z_-^2=1,] = \alpha F^2(2/r_i)/6\pi$ and assuming similar hydrodynamic radii (r_i) [128]. The hydrodynamic radii can vary a lot, however, and therefore we also use them in the calculations (Figure 10b) [130–132].

3.4 Spectroscopy & diffraction

3.4.1 Raman spectroscopy

Raman spectroscopy provides information about the microscopic structure and the intermolecular interactions, and it uses electromagnetic radiation to study vibrational (and rotational) transitions in molecules. These transitions appear in the 10^4 – 10^2 cm^{-1} (infrared) region and emerge from vibrations of the nuclei in the molecules [133]. During operation, a monochromatic laser illuminates the sample and the external electric field of the incident beam interacts with the electron cloud of a sample. A vibrational state is temporarily raised to a "virtual state", energetically situated between the highest vibrational and next highest electronic state (Figure 11). This transition is not quantized and the inelastic scattered photons, the Raman scattering, are shifted up or down in energy (anti-Stokes or Stokes). Or in other words, as depicted in Figure 9, Raman spectroscopy measures relative frequencies scattered by the sample, whereas *e.g.* infrared spectroscopy (IR) measures the absolute frequencies. The shift holds information about the vibrational modes, "structural fingerprints", corresponding to the molecular vibrations happening in the particular sample. The molecule must undergo a change in polarizability during the vibration for it to be Raman active, where polarizability refers to how easily the electrons are distorted from their original position.

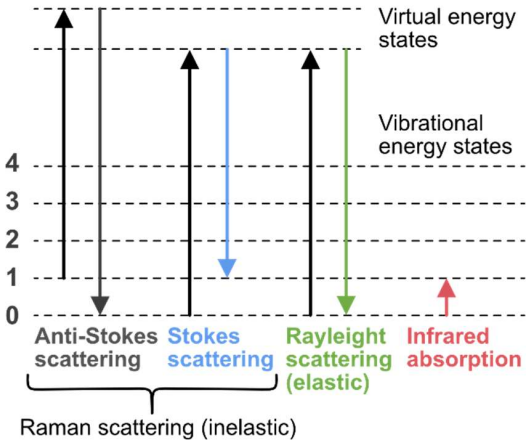

Figure 11. Energy level diagram of the states involved in Raman spectroscopy.

Raman spectroscopy is a useful technique to study the local water structure of aqueous electrolytes, and by investigating the OH-stretching vibrations (2800-4000 cm^{-1}) the relative amount of free water in the electrolyte can be determined. By spectral fitting and peak deconvolution, the spectra can be broken down and analyzed, as the contributions of different OH vibrations are distinguished. Authors differ in how many

peaks they assign, typically varying from two to five Gaussians, and Sun assigned five bands: 3005 cm^{-1}, 3226 cm^{-1}, 3434 cm^{-1}, 3573 cm^{-1}, and 3640 cm^{-1} to O-H vibrations engaged in DAA, DDAA, DA, and DDA hydrogen-bonding, and free O-H vibrations, where D stand for a proton donor and A refer to a proton acceptor [134]. The analysis is typically done by comparing the intensities and areas of the DA and DDAA peaks, and increased ratios indicate a decreased amount of free bulk water in the electrolyte. We used a Dilor XY 800 to record the spectra with either an Ar-Kr laser (BeamLok 2060, Spectra-Physics) or a 50 mW solid-state laser (Hübner Photonics), both 514.5 nm and vertically polarized in a 90° scattering configuration.

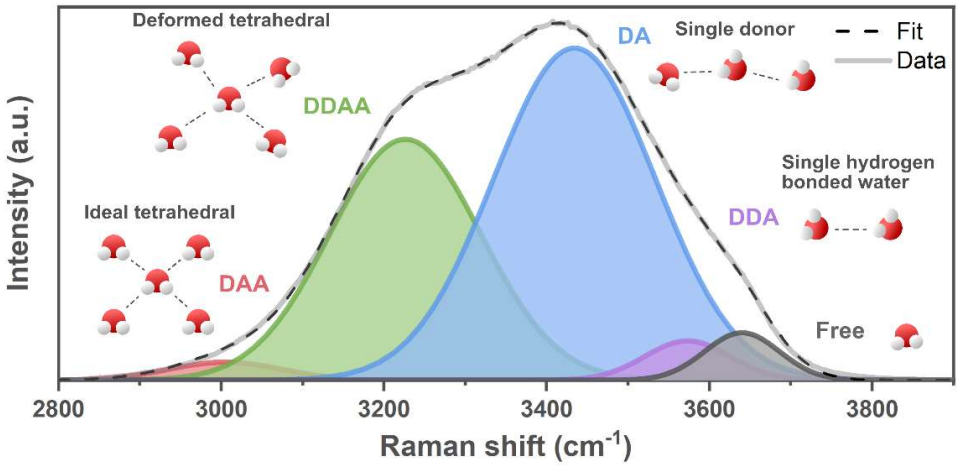

Figure 12. Raman spectra in the O-H stretching vibration region and the corresponding peak deconvolution of pure water [134] [193]. ***[I]***.

3.4.2 Fourier-transform infrared spectroscopy

IR uses radiation in the infrared portion of the electromagnetic spectrum to measure the interaction with matter by absorption, emission, or reflection, and it is used to study and identify compounds or functional groups in solids, liquids, or gases. As molecules above 0 K are non-stationary, they vibrate and absorb frequencies characteristic of their structure. For the sample to be IR active, the vibrational modes need to be associated with a dipole moment change. A common sampling technique used with IR is attenuated total reflection (ATR), where an evanescent wave arises from an infrared beam having total internal reflection in the ATR crystal. The sample is situated next to the crystal, in this case a germanium crystal due to its high refractive index, and the sample absorbs light which is later registered in the detector.

Herein, Bruker Alpha ATR Fourier-transform IR (FTIR) and NicoletTM iSTM 5 FTIR (Thermo Fisher Scientific) spectrometers were used, where all the infrared frequencies are measured simultaneously, enabling fast measurements. By introducing an interferometer with a beam splitter, the infrared beam is split into two, and in short, they are reflected by mirrors, interact with each other, and when returning to the beam splitter they have travelled different distances. The resulting interferogram is then Fourier transformed into an IR spectrum, where the peaks can be associated with functional groups in the sample.

3.4.3 Ultraviolet-visible spectroscopy

Ultraviolet-visible (UV-Vis) spectroscopy measures the absorbance or reflectance of light in the UV-Vis region and is a technique used to identify and quantify compounds in a sample. The UV-Vis spectrophotometer passes a beam of light through the sample and measures the amount of light that is absorbed at each wavelength, where the amount is proportional to the concentration of the absorbing compound. The UV-Vis spectra were recorded on a Mettler Toledo UV5bio spectrometer with an absorption quartz cell from 200-800 nm (Hellma analytics, Quartz Glass High Performance 200-2500 nm, 1 mm optical path length).

3.4.4 Inductively coupled plasma atomic emission spectroscopy

Inductively coupled plasma atomic emission spectroscopy (ICP-AES) is an elemental analysis technique that uses inductively coupled plasma to excite atoms and ions which then emit radiation of particular wavelengths, characteristic of the elements present in the sample [135]. The equipment is made of two parts, the inductively coupled plasma source (often argon) and the atomic emission spectrometry detector. In short, the aqueous sample is nebulized to a mist and introduced to the plasma. The sample is then ionized and release radiation specific to the element and the intensity is proportional to the concentration of elements in the sample. Herein an ICP-OES iCAP™ PRO XP (Thermo Fisher Scientific) was used.

3.4.5 Powder X-ray diffraction

X-rays are electromagnetic radiation with a characteristic wavelength (λ) in the Ångström range (1 Å = 10^{-10} m). Photons of such high frequency are commonly used to characterize the crystal structure(s) of compounds by the diffraction phenomena, hence X-ray diffraction (XRD). A Bruker D8 Discover set-up with Cu radiation was used in a Bragg-Brentano geometry with a Ni filter to cut Cu K-β contributions. By directing the beam towards the sample in different angles (Θ), constructive interference is produced when Bragg's law is satisfied, according to

$$n\lambda = 2dsin\Theta, \qquad (Eq. 18)$$

where n is a positive and d relates to the lattice spacing in the crystal structure. The resulting diffractogram generates peaks on the 2θ x-axis with corresponding intensities, and the peak's positions can be seen as "fingerprints". By identifying each peak, the crystal phases present in the sample can be determined. This technique, as well as FTIR spectroscopy, were used on active material powders and *ex situ* to characterize electrodes in different state-of-charge, to study if, and how, the local environment of functional groups and the crystal structure were changed during cycling, respectively, as cations had been (de)intercalated.

3.5 Electrochemical characterization

3.5.1 Linear sweep voltammetry

The electrochemical stability of an electrolyte is important to be aware of, to know the voltage range the battery can operate in, and when unwanted side reactions such as water splitting start occurring. LSV was used to measure the ESW of the electrolytes; by applying a constant voltage rate in one direction at the time, the responding current is measured, and the voltage is swept until a set current density limit, defining the ESW (Figure 13). At this point the current from the chemical reactions is no longer negligible, and for absolute potentials higher than this the electrolyte is no longer considered electrochemically stable. However, defining the stability of an electrolyte and comparing ESWs is not straightforward. To begin with, the current density limit is not set in stone, it is often arbitrarily chosen and varies vastly among authors (0.01-5 mA cm^{-2}) [136], and is sometimes not communicated. Similarly, the scan rate often varies (0.1-100 mV s^{-1}), which influences the current response and induces overpotentials. Moreover, the cell dimensions and electrolyte volume – rarely discussed – also should be similar for a fair comparison to be made. Yet, one of the most influential factors regarding the onset of OER/HER is the WE. This is due to materials having inherent overpotentials, effectively moving the water-splitting reaction according to the catalytic nature of the surface [137]. A standardized cell is therefore desirable as discussed previously in section 3.2 (Figure 8). Finally, since the water-splitting reactions involve H^+/OH^- they are also heavily influenced by the pH in aqueous electrolytes, and the potential shift of the reactions can be approximated by the Nernst equation.

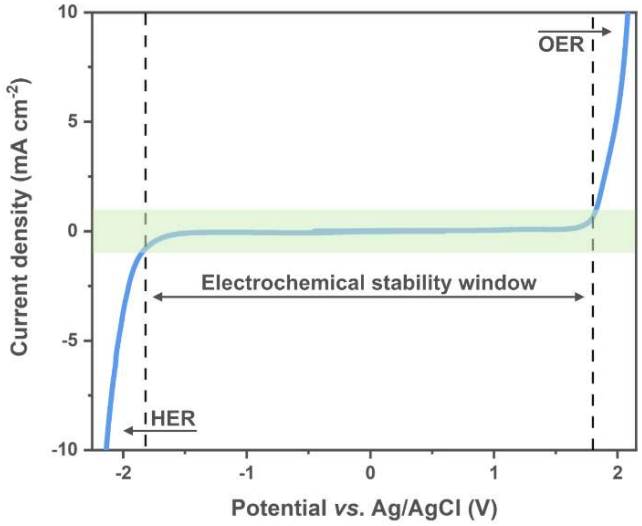

Figure 13. Voltammogram with the green region and dashed lines outlining the ESW.

3.5.2 Cyclic voltammetry

Similar to LSV, CV sweeps the set potential range of the WE and records the current response, but now in a cyclic manner. The resulting voltammogram visualizes the electrochemical behavior of the electrode and holds information about the charge storage mechanisms. By analyzing the voltammogram, it is possible to determine what kind of reactions occur, at what potentials the reactions occur, and of what magnitude the reactions occur. This was a crucial tool in the initial stages when characterizing the active materials, as

quick scans can be made to figure out the material's redox activity, before more elaborate electrochemical investigations.

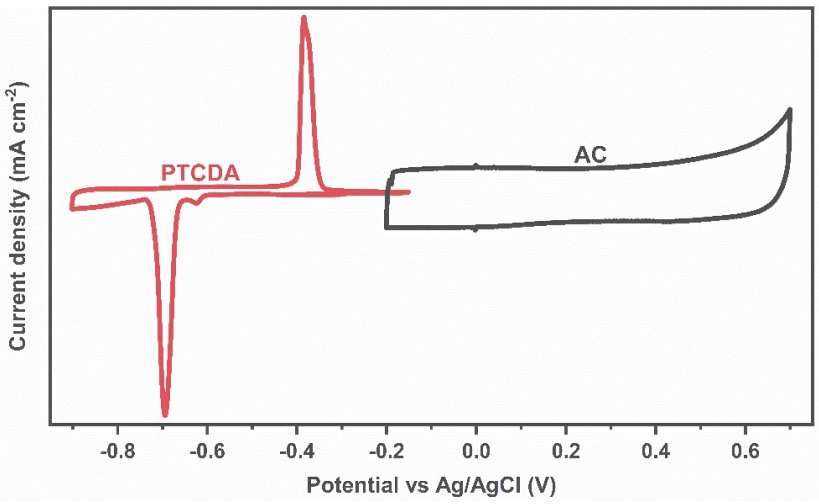

Figure 14. Cyclic voltammogram.

The characteristic Faradaic and non-Faradaic behaviours are illustrated for PTCDA and AC (Figure 14), where the former displays distinct redox peaks at specific potentials, while the latter has rectangularly shaped profiles throughout the entire voltammogram. This is a result of the different charge storage mechanisms, where electron flow from oxidation and reduction reactions generate peaks [138], while the rectangular shapes originate from the continuously forming electric double layer at the electrode surface.

In CV, the scan speed is chosen depending on what material and what mechanism is studied. Slower speeds (<0.5 mV s^{-1}) are often applied when characterizing redox active materials, and especially new materials, as the peaks will be sharper and more easily interpreted. Faster speeds (>10 mV s^{-1}) are typically applied for supercapacitor materials, or when the behavior and performance of the system is to be analyzed and put to a test. Only higher scan rates may reveal if the charge storage mechanism is fast, if the peaks for Faradaic materials will remain sharp and with small separation, which is important for high power applications. In this work a variety of scan speeds have been utilized, ranging from 0.2 mV s^{-1} up to 50 mV s^{-1}, depending on what material and what mechanism were of interest.

Moreover, by sequentially applying a range of scan rates, the Faradaic and non-Faradaic current contributions can be determined. By plotting the logarithm of the peak current (i) *vs*. the sweep rate (v), the b parameter from

$$log\, i = b\, log v + log a \qquad (Eq.19)$$

can be extracted, and Faradaic reactions result in $b \approx 0.5$, while non-Faradaic give $b \approx 1.0$ [139]. The relationship between v and i can also be written as

$$i = k_1 + k_2 v^{1/2} \qquad (Eq.20)$$

where k_1 and k_2 are potential-dependent constants, and k_1v and $k_2v^{1/2}$ correspond to the non-Faradaic and the Faradaic current contributions of the total amount of charge, respectively.

3.5.3 Galvanostatic cycling

The most common electrochemical technique used to assess batteries and hybrid supercapacitors is potential limited GC. GC is essentially used to monitor how electrochemical charge storage devices operate; a constant current is applied, and the resulting voltage is recorded, creating charge/discharge curves (Figure 15), whereby the capacity of the electrode or cell can be obtained ($I \cdot t$). Faradaic materials typically show flat plateaus corresponding to the redox potentials of the redox reactions happening, whereas non-Faradaic materials instead have sloping profiles with linearly increasing capacity, a result of the continuous surface charge accumulation. Pseudo-capacitance, on the other hand, is a Faradaic process with fast surface/near-surface redox reactions, which ideally generates an electrical response (and b parameter) similar to capacitive materials [27].

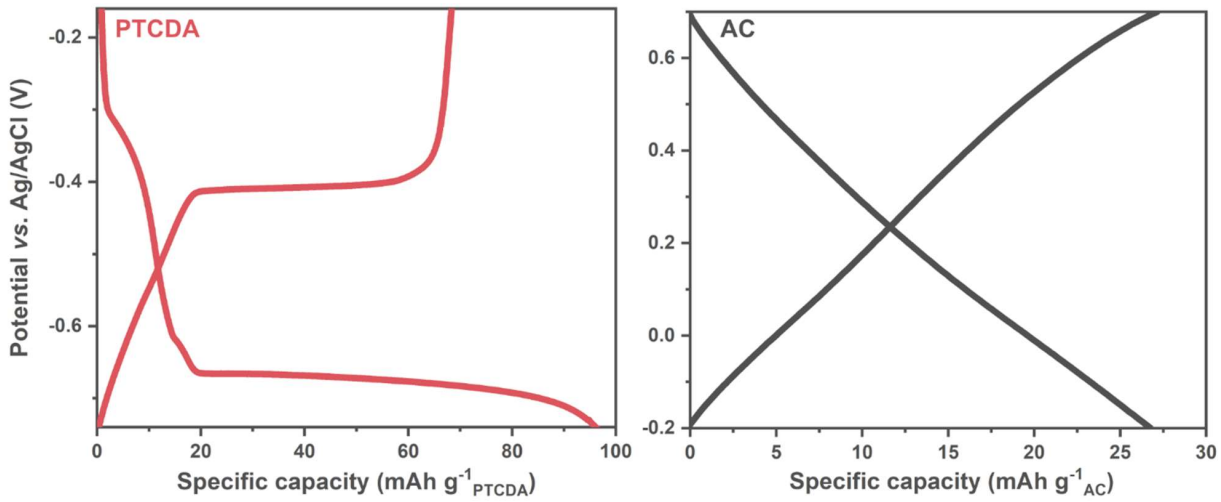

Figure 15. GC charge/discharge curves.

GC can also be used to calculate the energy/power densities by integrating the area (Figure 16a). They are popular performance metrics even outside the battery field and enable comparisons between different energy storage technologies.

3-electrode cell configurations are common when studying electrodes in half-cells, but it can also be useful when cycling full cells. By monitoring all electrode potentials simultaneously, the electrochemical behavior and the individual contributions of the electrodes can be distinguished (Figure 16a). This can *e.g.* reveal where unwanted side reactions occur, and it is particularly useful when capacity balancing cells for optimal full cell performance. As an example, by running the Na-HSCs in 3-electrode Swagelok cells, the charge/discharge profiles were monitored, and *e.g.*, if the absolute capacity (and thereby weight) of the AC electrode was not sufficiently high, this would instantaneously be illuminated as the voltage plateau of the PTCDA electrode would not be fully utilized. Well-balanced cells make use of the entirety of the plateau and deliver full cell capacities similar to the limiting stand-alone electrode.

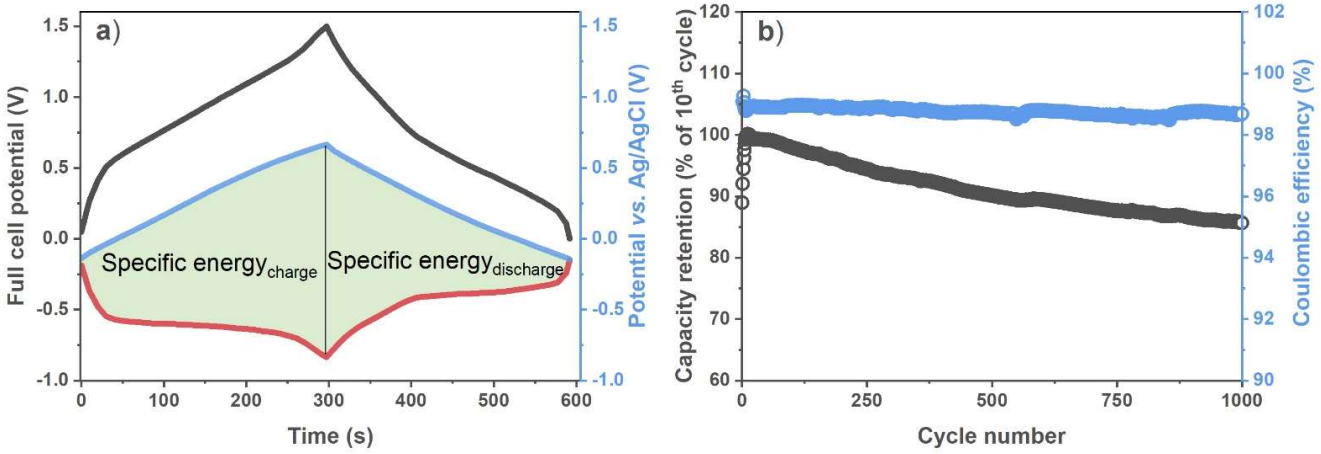

*Figure 16. a) GC charge/discharge curves and b) cycling stability test of a PTCDA||AC full cell. [**II**].*

GC is also used to study the cycling stability and efficiency (Figure 16b). The former is done by doing many galvanostatic cycles and recording the capacity at each cycle. The capacity retention can thus be calculated by dividing the remaining capacity by the initial capacity ($Q_{final}/Q_{initial}$). The corresponding Coulombic efficiency for each cycle, *i.e.*, $Q_{discharge}/Q_{charge}$ is another measure used to provide information on how much useful capacity that can be withdrawn. Last but not least, the energy efficiency of an electrode, or a full cell, can be calculated as the ratio of the specific energy during discharge *vs*. charge ($E_{discharge}/E_{charge}$), extracted from the areas in the charge/discharge plot (Figure 16a).

3.5.4 Electrochemical impedance spectroscopy

Finally, EIS was used as a tool to measure the resistances in the assembled cells. Typically, a sinusoidal voltage perturbation of ~5 mV is applied, and the phase and the magnitude of the current is recorded. The applied voltage must be small not to induce charging or discharging, and so the current responds linearly to the voltage. By doing this in a frequency sweep (*e.g.* 100 kHz – 100 mHz) a Nyquist plot can be created with the complex cell impedance $Z(f)$ as a function of frequency (Figure 17).

Choosing an equivalent circuit model for the experimental data is not straight forward and can require a lot of trial and error. By implementing the simple and commonly used Randles circuit cell model, physical properties such as the charge-transfer resistance (R_{ct}) and the electrolyte resistance (R_s) can be extracted from the Nyquist plot, where C_{dl} and Z_w represent the double layer capacitance and the Warburg diffusion element, respectively. EIS was done in Swagelok cells for the stand-alone electrodes, but to ensure more reproducible and comparable results, the full cells were studied in 2-electrode coin-cells where the applied pressure between the two electrodes is kept more constant.

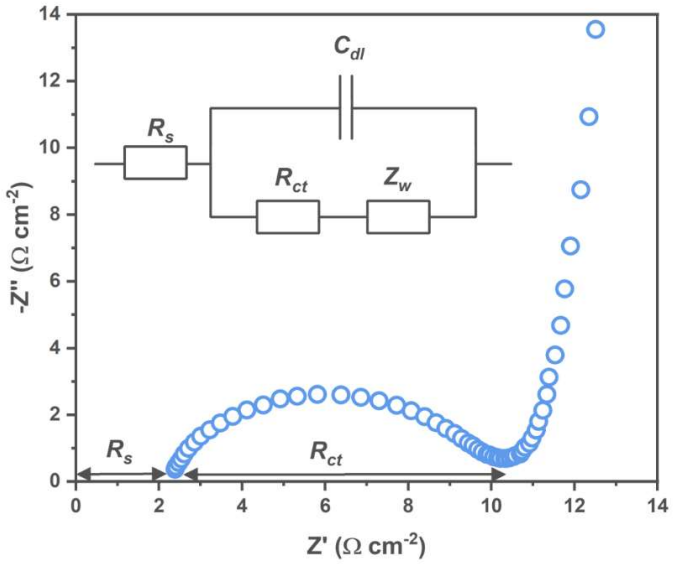

Figure 17. Nyquist plot and Randles circuit.

4 | Results & Discussion

4.1 Developing hybrid electrolytes

Starting from the standard and most used aqueous sodium-ion electrolyte 1 M $Na_2SO_{4(aq)}$, the idea was to find suitable additives that would enhance the ESW and suppress active material dissolution during cycling. This was an unexplored path which had (and have) a lot of potential as the stock solution of saturated (*ca.* 1.9-2.0 m) Na_2SO_4 has a very low viscosity (*ca.* 1.9 mPa·s) and high ionic conductivity (*ca.* 140 mS cm^{-1}) at 30°C. Thus, introducing additional components which in most cases increases the viscosity and decreases the ionic conductivity will most likely not be detrimental for the battery performance as 20 times the viscosity or one-hundredth of the ionic conductivity would be sufficient for practical use. The restrictions were not to incorporate compounds that would drastically affect cost, safety, or sustainability.

4.1.1 Gdm_2SO_4

The guanidinium cation ($C(NH_2)_3^+$ or $[Gdm]^+$) is known to denature proteins by interacting with the water molecules and altering the hydrogen bonding network [140], and the hypothesis was that the ESW could be broadened by binding the free water in the electrolyte with a guanidine salt. Gdm_2SO_4 was chosen to not introduce more than one component at once, and at first it seemed promising due to its high solubility. Even in saturated $Na_2SO_{4(aq)}$ the salt dissolves up to 9.0-10.0 m, creating a WIBE. When recording LSV curves with the commonly used rate 1 mV s^{-1} and setting the current limit to 1 mA cm^{-2}, the oxidation limit expands after adding the second salt with about 140 mV, whereas the opposite is true during reduction (Figure 18). Considering there is no formal convention regarding what current density limit to use we are here careful to draw any hard conclusions, because if the limit was chosen to be *e.g.* 0.25 mA cm^{-2} then the reduction stability would be unaffected (Figure 18a). During oxidation the profiles are similar but offset (Figure 18b), why changes in the kinetics (viscosity) might be the route cause, affecting the water diffusion and therefore the onset of gas evolution.

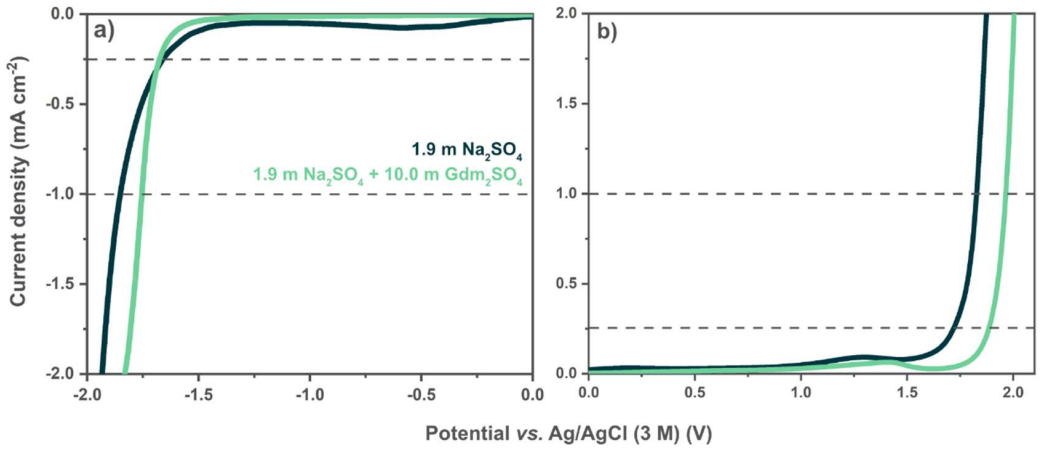

Figure 18. ESW of the aqueous electrolytes measured by LSV. A zoom-in of a) the reduction and b) the oxidation. Dashed lines mark the two stability limits.

Raman spectroscopy was thereafter applied to analyze the OH-stretching modes of the water molecules, situated at 2800-4000 cm^{-1}, to provide insight on the local structure. The overall intensity of the OH-stretching vibrations does decrease when adding 10.0 m Gdm_2SO_4 to the saturated $Na_2SO_{4(aq)}$ (Figure 19a), but after deconvolution, the peak intensity and area ratios (I_{ratio} and A_{ratio}, respectively) of the 3434 cm^{-1} and 3226 cm^{-1} are not increasing (Table 1), thus not indicating a decrease in the free water. Gdm^+ –NH stretching peaks are also present in this region which should make the I_{ratio} and A_{ratio} comparison invalid [141]. To further study the effect of Gdm_2SO_4, 9.0 m and 15.0 m were added to 1.0 m Na_2SO_4 and here the trends are even less pronounced (Figure 19b). The OH-stretching bands are remarkably unaffected by the increased Gdm_2SO_4 concentration and we attribute this to Gdm_2SO_4 ion-pairing, as observed before [142,143]. The Gdm_2SO_4-WIBEs were therefore disregarded and not analyzed further.

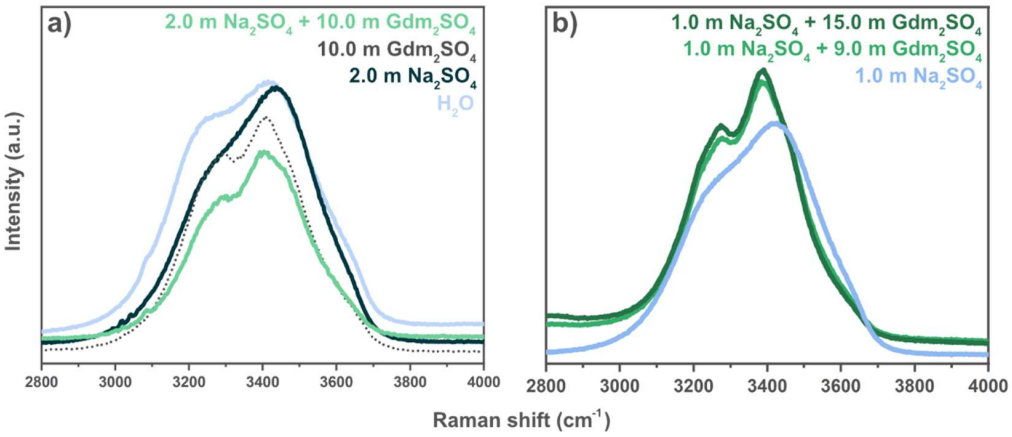

Figure 19. Raman spectra of Na_2SO_4 and Gdm_2SO_4 based aqueous electrolytes using a) Ar-Kr and b) solid state lasers.

4.1.2 Magnesium and calcium salts

The search for electrolyte additives continued, and the abundant elements Mg and Ca were considered. Several salts meeting the requirements were found and mixed with saturated Na_2SO_4. The Ca salts ($CaAc_2$ and $CaSO_4$) unfortunately have extremely low solubilities, while $MgAc_2$ and $MgSO_4$ dissolves much easier. When applying LSV, however, for the electrolytes with the former salt the acetate is oxidized before the OER, narrowing the ESW (Figure 20). The highest concentration (2.0 m Na_2SO_4 + 1.0 m $MgAc_2$) also has problems, as it did not completely dissolve and was therefore also disregarded.

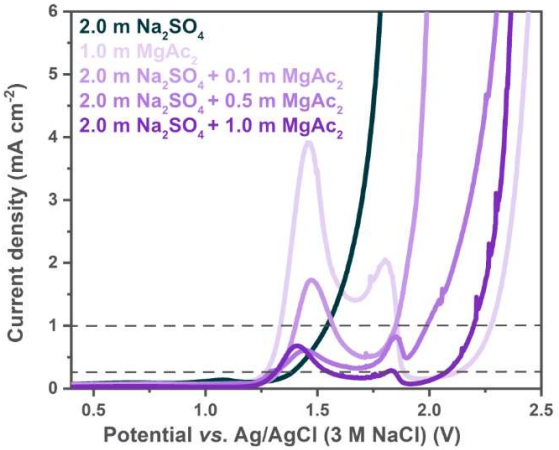

Figure 20. LSV of aqueous electrolytes based on Na_2SO_4 and $MgAc_2$.

$MgSO_4$ on the other hand not only dissolves to more than twice the concentration as compared to $MgAc_2$, but the newly made "Hybrid electrolyte" which consists of 1.9 m Na_2SO_4 + 2.4 m $MgSO_4$ also shows promising results with LSV (Figure 21).

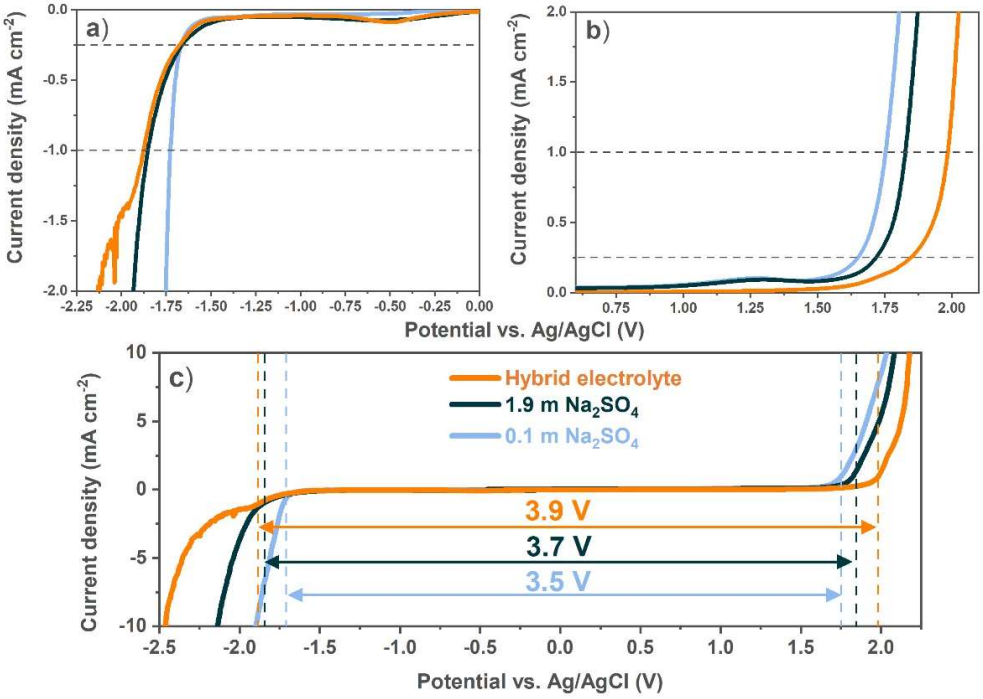

*Figure 21. ESW of the aqueous electrolytes measured by LSV. A zoom-in of a) the reduction and b) the oxidation and c) a depiction of the full window. Dashed lines to mark the stability limit. [**I**].*

The ESW expands from 3.5 V to 3.7 V by increasing the salt concentration from 0.1 m to 1.9 m, using the same scan rate and current density limit as before (Figure 21c). ESWs for 1 M Na_2SO_4 have been reported from 1.5-2 V on stainless steel at 0.1 mV/s to 2.2 V using Ti at 5 mV/s [144,145]. Compared to the literature our 1.9 m electrolyte ESW is large, and it is due to the reduced electrocatalytic properties of glassy carbon for HER/OER, resulting in overpotentials compared to a more practical set-up. Finding comparable data, however, is difficult as discussed in Section 3.5.1, and we here nevertheless solely intend to use these data for comparative purposes within this study to study the effect of salt concentration. The hybrid electrolyte results in an even wider ESW of 3.9 V, and the wave like current density increase at *ca.* 1.25 V during the oxidation is completely suppressed with the hybrid electrolyte, thus showing a considerable stability increase (Figure 21b).

From the LSV it is clear that there is some kind of substantial difference in the ESWs. Again, Raman spectroscopy was therefore applied to analyze the OH-stretching modes of water. A shift and a sharpening of the overall broad band envelope is seen as function of salt concentration, including the hybrid electrolyte (Figure 22a).

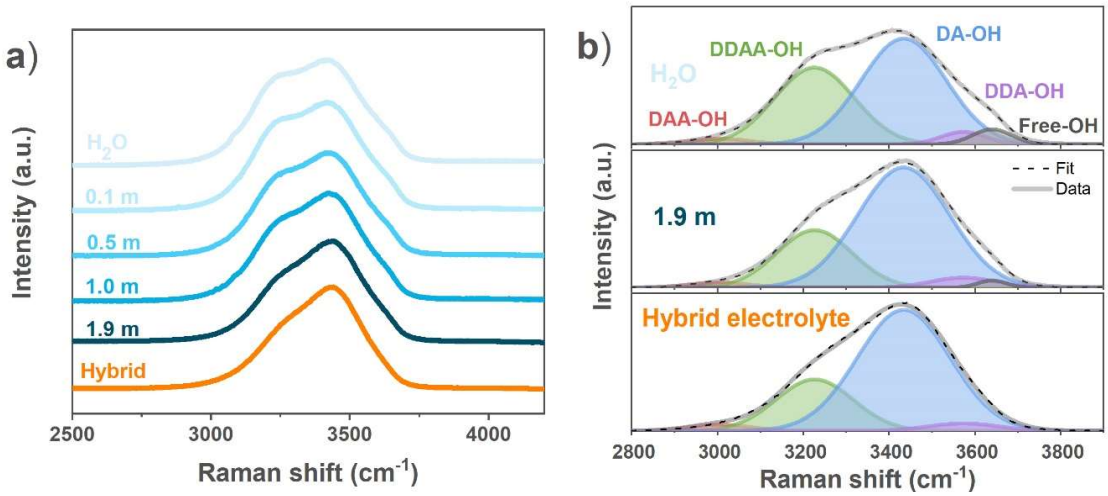

*Figure 22. a) Raman spectra in the O-H stretching vibration region and b) the corresponding peak deconvolution of the pure water, the 1.9 m Na_2SO_4 electrolyte, and the Hybrid electrolyte. **[I]**.*

The Raman spectra of pure H_2O, 1.9 m $Na_2SO_{4(aq)}$, and the Hybrid electrolyte were further deconvoluted into Gaussians (Figure 22b). A comparison of the I_{ratio} and A_{ratio} of the 3434 cm^{-1} and 3226 cm^{-1} bands clearly reveal the ratios to increase with increasing salt concentration (Table 1), indicating the hydrogen bonded "free" water contribution relatively decreases [134,146]. By their very compositions, the 1.9 m Na_2SO_4 and the Hybrid electrolytes have H_2O/cation ratios of 14.6 and 9.0, respectively, and as the Walden plot indicates similar ionicities (the degree of ion dissociation), the latter electrolyte should have less "free" water available (Figure 24). We therefore attribute the wider ESW to a combination of higher viscosity, a decreased amount of free water, and incorporating a more chaotropic cation. This was achieved by applying the mixed cation concept, as it increases the salt solubility by the increased entropy, making the liquid phase more stable and unlocking the possibility of more water-binding ions [147]. Yet, we are far from seeing the narrow ~3550 cm^{-1} peak that emerges for WISEs/WIBEs at very high salt concentrations (>20 m) and correspond to H_2O/Na^+ ratios of 2-3 [148].

Table 1. Intensity and peak area ratio of the deconvoluted peaks at 3434 cm^{-1} and 3226 cm^{-1} as well as the total OH-band area between 2800-4000 cm^{-1}, and the corresponding water concentration.

	I_{ratio}	A_{ratio}	A_{tot}	C_{water} (M)
H_2O	1.38	1.47	1.8446E7	55.51
1.9 m	2.09	2.55	1.8304E7	52.27
1.9 + 2.4 m*	2.35	2.81	1.7814E7	49.73
2.0 + 10 m**	2.02	2.36	5.8579E6	-

* $MgSO_4$. ** Gdm_2SO_4.

To further characterize the promising Hybrid electrolyte, the effect of salt concentration on the physico-chemical properties; ionic conductivity, viscosity, and density were studied for temperatures up to 80°C. The densities of the electrolytes increase more or less linearly as a function of salt concentration, while the viscosities increase exponentially, and as expected both decrease as a function of temperature (Figure 23). The Hybrid electrolyte displays a viscosity of *ca.* 9 mPa·s at 30°C, which is half an order of magnitude higher than for the most concentrated Na_2SO_4 based electrolyte (*ca.* 1.9 mPa·s at 30°C) but compared to WISEs, the Hybrid electrolyte is still very fluid; *e.g.* a 35 m NaFSI WISE renders 97 mPa·s [149].

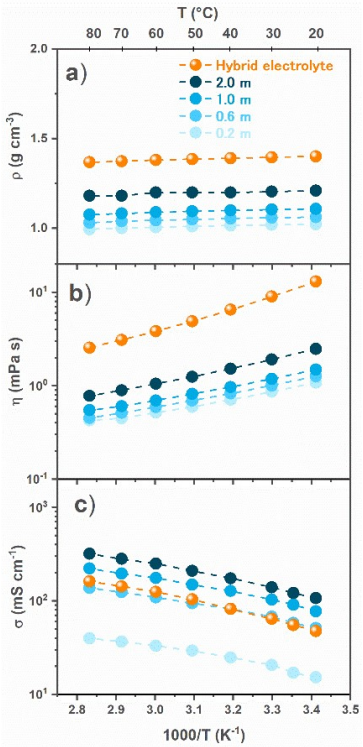

*Figure 23. Arrhenius plots of the: a) density, b) viscosity, and c) ionic conductivity for the Na_2SO_4-based aqueous electrolytes. Dashed lines to guide the eye only. **[I]**.*

The intrinsic high ionic conductivities of aqueous electrolytes are also witnessed here (Figure 23c), and in the same order of magnitude as NaTFSI, NaFSI and $NaClO_4$ based aqueous electrolytes [150]. Moreover, the ionic conductivity for the Hybrid electrolyte decreases less than what would be expected based on the increased viscosity, relative to the same Na_2SO_4 concentration, to 64 $mS \cdot cm^{-1}$ at 30°C, pointing to some synergy. There is clearly an increase in the charge carrier concentration, but perhaps also somewhat different structure and dynamics as the temperature dependence differs (Figure 23c).

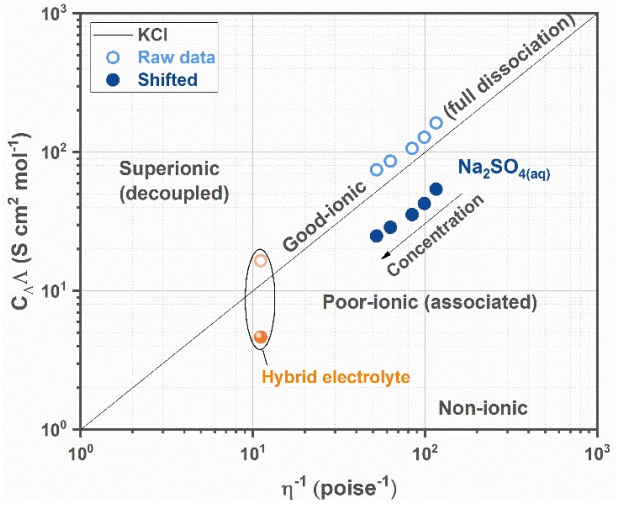

*Figure 24. Walden plot of the aqueous electrolytes at 30°C. [**I**].*

Finally, a Walden plot is made to study the relationship between the electrolytes' equivalent molar conductivities and viscosities [127], and qualitatively visualize their ionicities. The Na_2SO_4 based electrolytes, including the Hybrid electrolyte, are all relatively close to the ideal KCl line and thus the salts should dissociate to a large extent when immersed in water (Figure 24). Furthermore, as the slopes are close to unity, the activation energies for ionic conductivity and viscosity are similar, and hence the ion transport mechanism is very likely to be mainly vehicular [151].

Multivalent ions make comparisons with simple 1:1 salts more intricate, and it is not trivial how to properly represent the data in a Walden plot. Dave *et al.* compared aqueous Na_2SO_4 and $NaNO_3$ electrolytes and argued the higher ionicity of the former to originate from the stoichiometry difference [152]. Moreover, the highly charged and kosmotropic SO_4^{2-} could also make less solvent available for the cation, rendering smaller Na^+ first solvation shells. For a fairer comparison we apply a methodology previously used by Yang *et al.* where the ideal line of each electrolyte is shifted by a prefactor (C_Λ), derived in detail in section 3.3.2. Now, with $C_\Lambda(Na_2SO_4) = 2.84$ and C_Λ(Hybrid electrolyte) = 3.26, the ionicities of our electrolytes become akin to $NaTFSI_{(aq)}$ and $NaFSI_{(aq)}$ electrolytes [153]. On the other hand, considering a non-shifted ideal line, all the electrolytes can be classified as slightly superionic, *i.e.* the ionic conductivity and the viscosity are somewhat decoupled, thus the ions move faster than expected solely based on the viscosity [154].

4.1.3 GdmTFSI

The TFSI anion is indeed fluorinated to a large extent and expensive to make high purity salts with, but with the intention to use less lithium and to study the effect of a more chaotropic ion on the electrolyte stability, GdmTFSI was synthesized and characterized, and then electrolytes were created. Even though the water-breaking chaotropic effect is larger for anions [53], we do find similar trends to the recent findings of Reber *et al.* [120]. Their study found a strong correlation that more chaotropic anions result in electrolytes with larger electrochemical stabilities, and this correlation also seem to apply for the Gdm cation, as the ESW here expands by 0.25 V at 1.0 m and 0.1 V at 8.0 m (Figure 25), comparing pure aqueous solutions of LiTFSI *vs.* GdmTFSI.

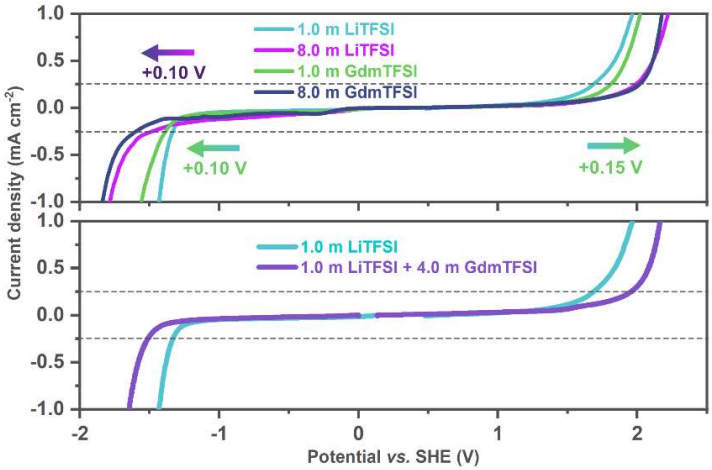

Figure 25. ESW of LiTFSI and GdmTFSI based aqueous electrolytes measured by LSV. 5 mV s^{-1} scan rate and a 0.25 mA cm^{-2} current density limit was used to define the ESW.

By again using the mixed cation concept, the TFSI-based hybrid electrolyte displays a 0.33 V broadened ESW compared to 1.0 m $LiTFSI_{(aq)}$ (Figure 25). We decided to not surpass 4.0 m of GdmTFSI as the IR and ionic conductivity investigations point to more prevalent ion-pairing at higher concentrations. More specifically, the lower frequency band at *ca.* 1125 cm^{-1} becomes pronounced for concentrations >4.0 m, and as it matches the one observed for solid GdmTFSI we assign this band to the vibration of $[TFSI]^-$ linked directly to $[Gdm]^+$, *i.e.* ion pairs (Figure 26a). Fewer available charge carrying ions should also yield a lower ionic conductivity, which is observed above 4.0 m up to saturation (Figure 26b). The increased viscosity is of course a contributing factor here as well. Moreover, the water stretching bands at 2800-4000 cm^{-1} show a reduced intensity as the concentration of the GdmTFSI is increased, giving way to more pronounced –NH stretching peaks from the Gdm^+. Again, these –NH bands make it difficult to conduct the I_{ratio} and A_{ratio} comparison of the 3434 cm^{-1} and 3226 cm^{-1} bands, yet the substantial decrease in the latter indicate a weakening of the hydrogen bonded network of water [155], which previously has been attributed to the water-breaking effect of chaotropic ions and at least partially could be the reason for the increased ESW [120].

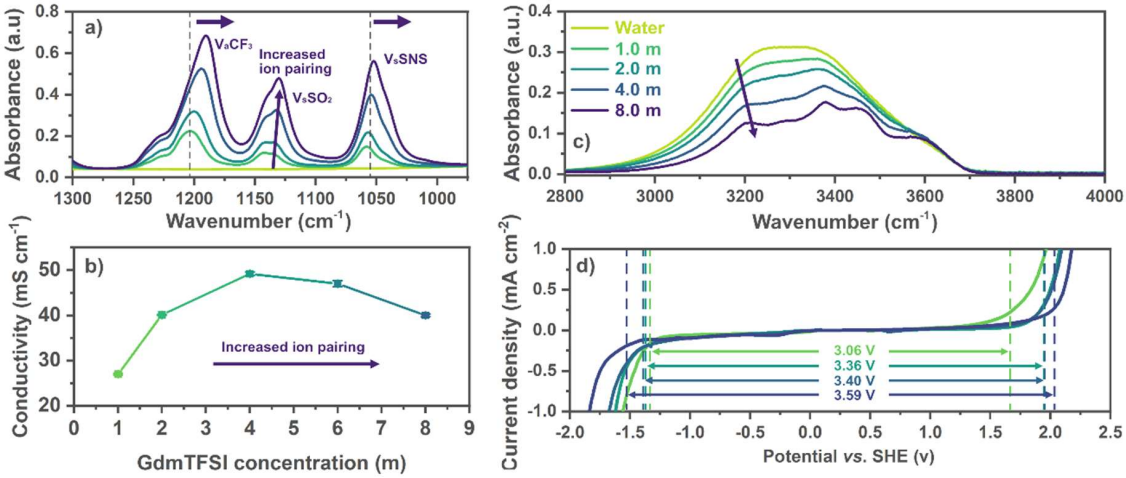

Figure 26. (a) 950-1300 cm^{-1} IR region, (b) ionic conductivity, (c) 2800-4000 cm^{-1} IR region, and (d) the ESW for GdmTFSI-based aqueous electrolytes.

4.2 Improving electrochemical performance

A considerable drawback of aqueous electrolytes is the high solubility of many electrode AMs. Here, we explore if modifying the conventional 1 M concentrated electrolytes can improve the cycling stability and rate performance. The investigated electrodes, using common ASIB/Na-HSC active materials (NTP, Fe-PBA, Mn-PBA, and AC), as well as PTCDA and PTCDI, were made more sustainable by using organic binders (CMC), separators (cellulose filter paper), and CCs (graphite foil).

4.2.1 Fe-PBA (Fennac)

First out, the commercial Fe-PBA Fennac ($Na_xFe[Fe(CN)_6]\cdot yH_2O$) was investigated by CV and GC. The rate capability tests with glassy carbon and Pt (not included here) CEs resulted in bad rate retentions, as the low surface area turned out to be a bottle neck for higher currents (Figure 27a). Instead, AC CEs with several times higher active material loading compared to the WE were used thereafter, significantly improving the rate capability (Figure 27b).

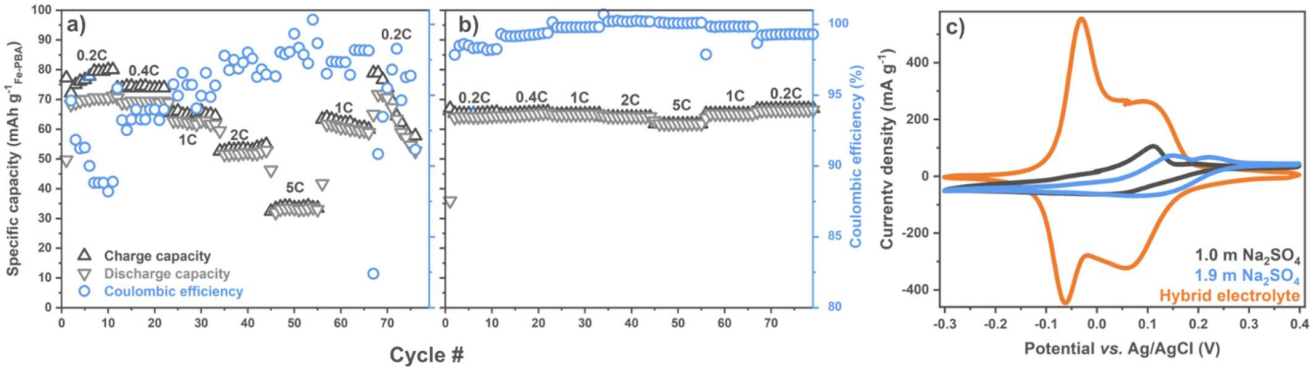

Figure 27. Fe-PBA electrode rate capability tests with a a) glassy carbon and a b) AC CE with the hybrid electrolyte between 0.4 and -0.3 V vs. *Ag/AgCl. c) Fe-PBA voltammograms at 0.2 mV s^{-1}.*

Voltammograms were recorded at 0.2 mV s^{-1} and during oxidation with 1.0 m $Na_2SO_{4(aq)}$ the Fe-PBA electrode has a predominant redox peak at *ca*. 0.1 V *vs*. Ag/AgCl and a minor peak *ca*. 0.1 V higher, denoted together as the 1st redox reaction (Figure 27c). During reduction the peak is broader, starting at *ca*. 0.025 V, without a clear "end". Fe-PBA behaves similarly with 1.0 m as with saturated $Na_2SO_{4(aq)}$, only differing with a slight Nernstian shift as is expected by the electrolyte concentration difference (Figure 27c). In contrast, with the Hybrid electrolyte it displays two adjacent redox peaks at *ca*. -0.03 V and 0.1 V *vs*. Ag/AgCl during oxidation and slightly down shifted during reduction (Figure 27c). The current density is more than five times higher, and the voltage profiles are significantly more symmetric with the Hybrid electrolyte suggesting an improved electrochemical behavior. This difference is most likely due to the higher electrolyte salt concentration and co-intercalation of Na^+ and Mg^+ as PBAs have shown to reversibility intercalate Mg^+ [156].

The GC charge/discharge curves and rate tests with 1.0 m $Na_2SO_{4(aq)}$, 1.9 m $Na_2SO_{4(aq)}$, and the Hybrid electrolytes differ to a large extent. The former fails to deliver a stable and reversible capacity (Figure 28ad), whereas with 1.9 m $Na_2SO_{4(aq)}$ Fe-PBA displays higher stability and reversibility, with capacities similar to other Fe-PBAs (Figure 28b) [157,158]. At 0.2C however, it fails to cycle with both electrolytes (inset Figure 28ab). In stark contrast, Fe-PBA with the Hybrid electrolyte exhibit excellent cycling stability, Coulombic efficiency (different 2nd y-axis), and capacity retention throughout all scan rates (Figure 28cf). In addition to Mg^{2+} co-intercalation, a peptization process resulting in colloidal active material particles could be the cause of the observed difference [157]. The reaction is thought to occur due to O_2 bubbling from the OER, and the higher viscosity and higher electrolyte stability of the Hybrid electrolyte could, in theory, suppress this reaction, but unfortunately the separators were not recovered post cycling which would have confirmed the presence or absence of blue colloidal particles.

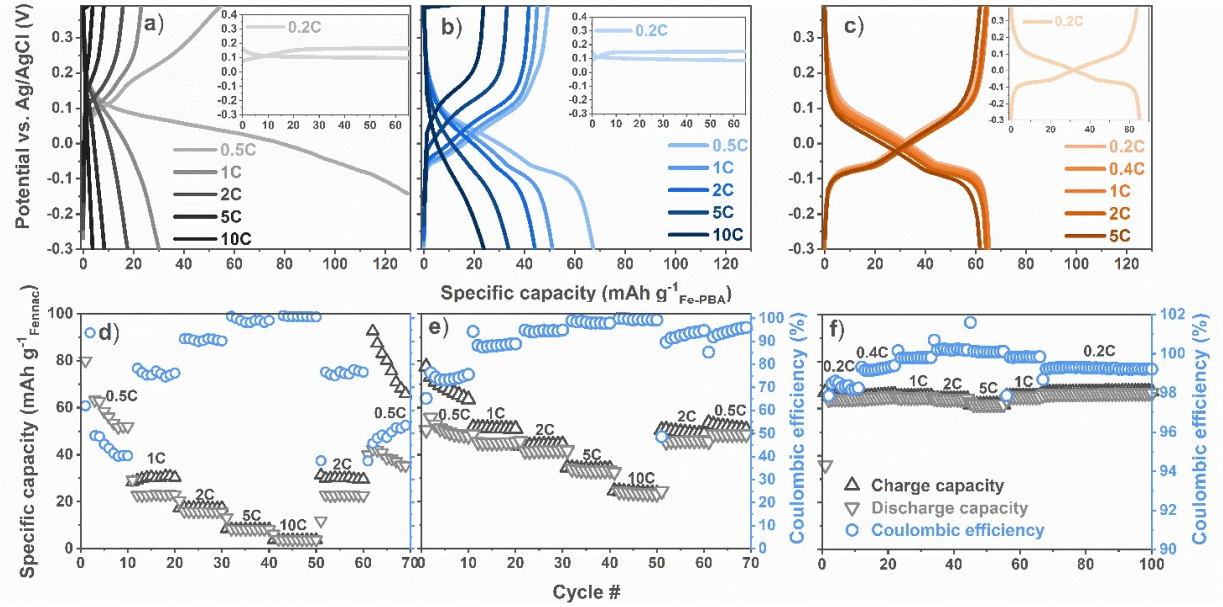

Figure 28. Fennac electrode rate capability tests with a,d) 1.0 m $Na_2SO_{4(aq)}$, b,e) 1.9 m $Na_2SO_{4(aq)}$, and c,f) the Hybrid electrolytes.

A 2nd reaction can be found at higher potentials, *ca.* 1.1 V during oxidation and *ca.* 0.75 V *vs.* Ag/AgCl during reduction when recording the voltammogram at 5 mV s^{-1} (Figure 29). Utilizing this peak is, however, problematic as current from the OER becomes significant at >1.15-1.2 V. To use it would require further developing the electrolyte to expand the oxidation limit or to use a completely different electrolyte with a larger ESW.

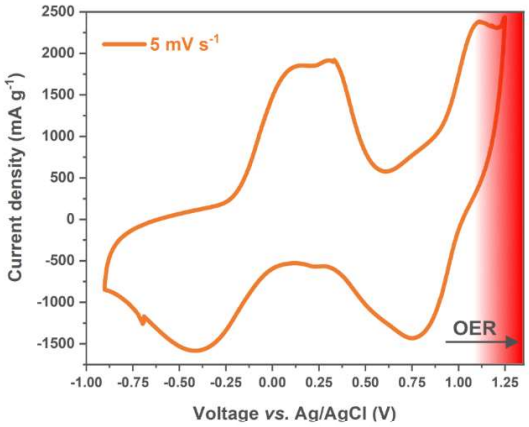

Figure 29. Voltammogram of a Fe-PBA electrode with the Hybrid electrolyte.

4.2.2 NTP

The negative electrode material NTP was studied with the Hybrid electrolyte *vs*. 1.0 m $Na_2SO_{4(aq)}$, and it displays sharp and closely situated redox peaks with both electrolytes at *ca*. -0.95 V and -1.03 V *vs*. Ag/AgCl for the oxidation and reduction, respectively (Figure 30ab), almost perfectly placed right at the edge of the ESWs. The current density with 1.0 m $Na_2SO_{4(aq)}$ is, however, only about half compared to the Hybrid electrolyte, and the latter is clearly more reversible, but still, the redox peaks diminish significantly already after 10 cycles. We here take a sidestep and bring in something completely different: the acetate WIBE 7.0 m NaAc + 20.0 m KAc studied by Khalid *et al*. produces much more stable peaks, also with a clear Nernstian peak shift from *ca*. -1.03 to -0.95 V *vs*. Ag/AgCl which can be attributed to the charge carrier concentration difference [159] (Figure 30c). The charge/discharge curves are in agreement with the voltammograms and NTP delivers *ca*. 130-140 mAh g^{-1} in the initial cycle with hybrid electrolyte and the WIBE, similar to the original work [81]. Although, the electrodes subsequently display severe capacity fading with low Coulombic efficiencies, as have been reported before due to Ti and P dissolution [86]. NTP with the WIBE performs best, with more capacity, higher Coulombic efficiency, and less capacity decay, similar to with $LiTi_2(PO_4)_3$ [159], but the cycling stability is still quite bad (inset Figure 30f).

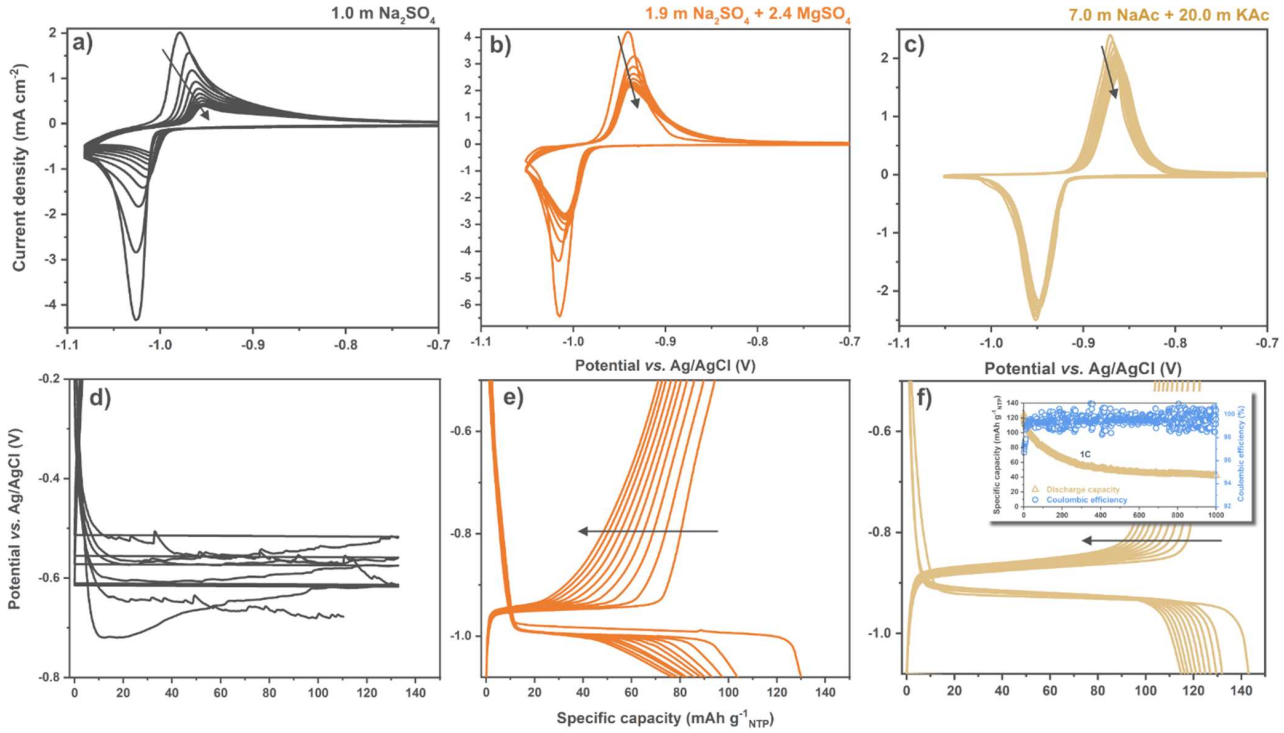

Figure 30. NTP a-c) voltammograms recorded at 0.2 mV s^{-1} and d-f) GC charge/discharge curves at 1C. f) Inset shows the long-term cycling of NTP with the WIBE.

Attempts were made to enhance the stability, *i*) binders such as Na-alginate and PVdF were used instead of CMC, *ii*) the graphite foil CC was swapped for Al, *iii*) sodium dodecyl sulfate (SDS) was added to the Hybrid electrolyte, and finally *iv*) 0.1-0.2 m NaOH was added to increase the pH to >12 to counteract the proposed degradation reaction of reduced NTP with dissolved O_2, where OH^- is a product [86]. Unfortunately, none of the above successfully improved the cycling stability and NTP remains unstable in the presence of O_2, which is the only real drawback hindering NTP from being an ideal negative electrode.

4.2.3 PTCDA

PTCDA was chosen as an alternative negative electrode active material, and the cyclic voltammogram reveals the PTCDA electrode to have a decreased current density already after 10 cycles with 1.0 m $Na_2SO_{4(aq)}$ (Figure 31a). It seems to work decently, but applying the Hybrid electrolyte produces much more stable and reversible reactions with higher current density (Figure 31b). The difference is most easily ascribed to the increased amount of charge carriers facilitating the redox reaction, and the reduced solubility of cation intercalated PTCDA by the lower water concentration, witnessed for WISEs [106] and discussed further on in more detail.

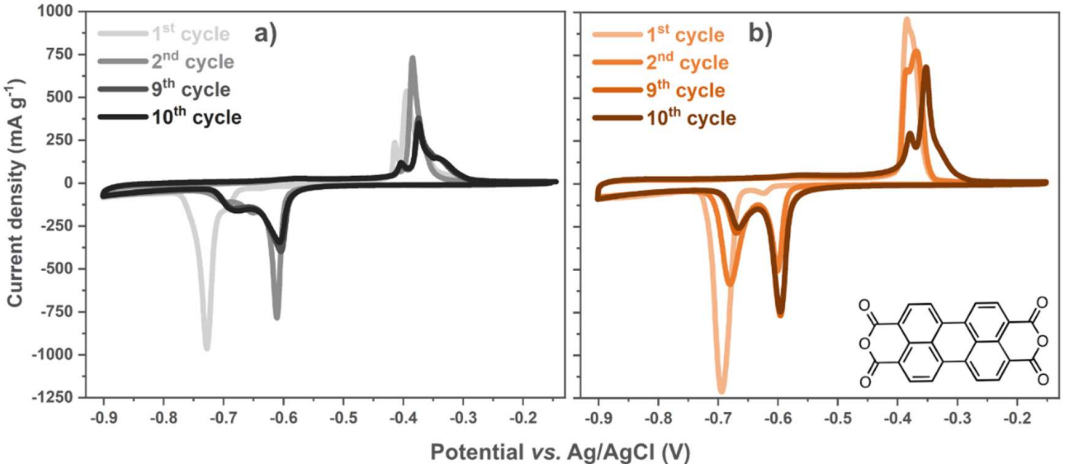

*Figure 31. CV of PTCDA electrodes using the a) 1.0 m $Na_2SO_{4(aq)}$ and b) Hybrid electrolytes, and the molecular structure of PTCDA. **[I]**.*

In the first cycle, one redox peak during reduction is seen at *ca.* -0.7 V, and likewise one during oxidation, at *ca.* -0.4 V *vs*. Ag/AgCl for both electrolytes (Figure 31). This is very similar to what has been observed for PTCDA using non-aqueous electrolytes, where also, after an electrochemical conditioning process during the initial cycle(s) [99,106] *i.e.* an activation phase, the peaks are split into several consecutive, stable, redox peaks (Figure 31). In contrast, for PTCDA using aqueous electrolytes with other cations, the CVs differ either in the number of peaks and/or in the redox potentials [106–108]. Therefore, we believe(d) this strongly indicates(ed) that Na^+ is the primarily active cation with our electrolytes.

In accordance with the CVs, the GC charge/discharge profiles display extended voltage plateaus with the Hybrid electrolyte, reaching initial charge and discharge capacities of 97 and 68 mAh g^{-1}, respectively (Figure 32b). After activation, which seems to involve *ca.* 30 mAh g^{-1} of irreversible cation intercalation, a stable capacity of *ca*. 70 mAh g^{-1} is achieved with excellent cycling stability (98.7%@100 with 0.2C from 2nd cycle) (Figure 32b & Figure 33f). In stark contrast, most cells fail completely to cycle with 1.0 m $Na_2SO_{4(aq)}$ using GC, and for the ones who do not fail, there are still severe problems already in the initial cycles (Figure 32a). This, again, is attributed to PTCDA continuously being dissolved in the electrolyte due to the low salt concentration (Figure 34).

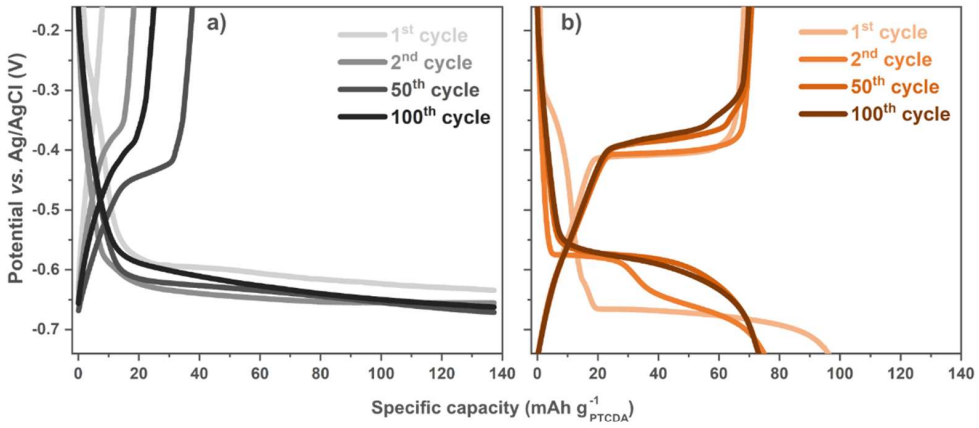

*Figure 32. GC charge and discharge curves of PTCDA at 0.2C using a) the 1 m $Na_2SO_{4(aq)}$ and b) the Hybrid electrolytes. [**I**].*

The rate capability tests reveal drastically impaired Coulombic efficiencies for the low C-rates with the 1 m Na_2SO_4 based electrolyte cells (Figure 33a). On the other hand, PTCDA with the Hybrid electrolyte displays cells with remarkable rate capabilities and Coulombic efficiencies throughout the entire C-rate sweep, despite its much higher viscosity (Figure 33d, different y-axes). The 100 cycle tests also confirm the Hybrid electrolyte to outperform 1.0 m Na_2SO_4 (Figure 33bcef), where the former displays acceptable Coulombic efficiencies and capacity retention at 0.2C, which further improves at 1C (98.9%@100 with 1C from 2nd cycle) (Figure 33e). To put it in context, β-PTCDA with a 30 m KFSI WISE provided *ca*. 88–90%@100 using significantly higher current density (x14) which may hide/reduce parasitic reactions and contribute to the stability [106].

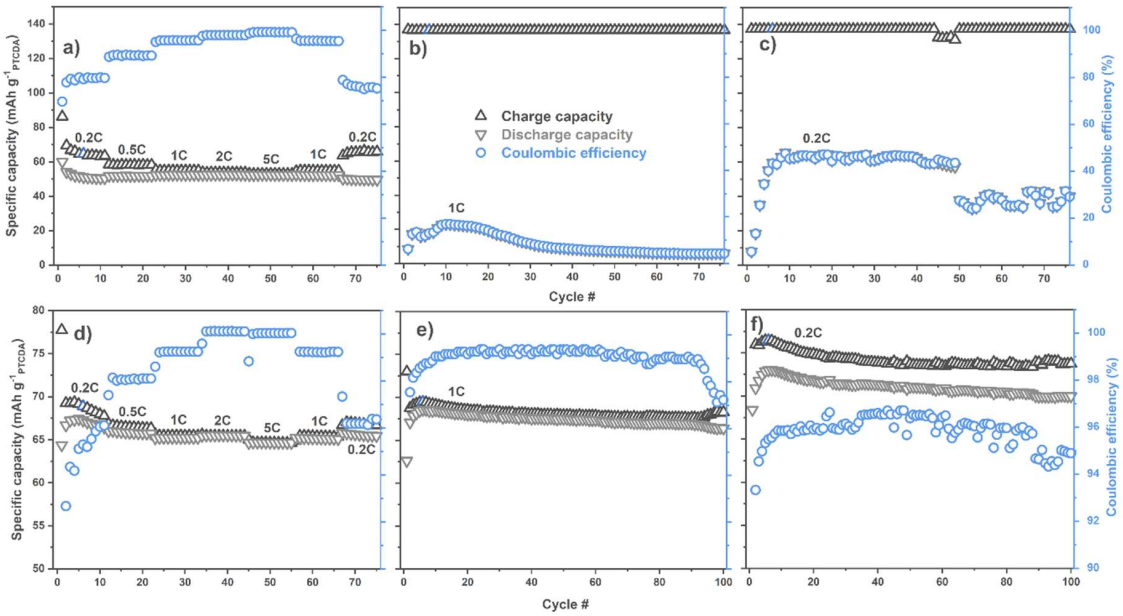

*Figure 33. PTCDA electrode a,d) rate capability test and b,c,e,f) GC with a-c) 1 m $Na_2SO_{4(aq)}$ and d-f) the Hybrid electrolyte. Note the right and left y-axis scale differences between a-c and d-f. [**I**].*

To validate whether suppressed dissolution of reduced PTCDA is the cause of the clear outperformance or not, the separators were recovered from the cells after the 100 cycle GC test. Indeed, no sign of any red colour indicating dissolved PTCDA [107,108] is seen on the separators with the Hybrid electrolyte (Figure 34ab), quite unlike the situation with 1 m $Na_2SO_{4(aq)}$ (Figure 34cd). A discharged PTCDA electrode was also immersed in water, dying the water dark red, verifying the polarity increase of PTCDA in its reduced state (Figure 34e). The separators were further immersed in 1 ml 2 m $NaOH_{(aq)}$, where dissolved PTCDA turns green when the structure is destroyed by OH^- [106,107]. Again, the separators from the hybrid electrolyte cells remain colourless (Figure 34f), supporting the notion of suppressed PTCDA dissolution.

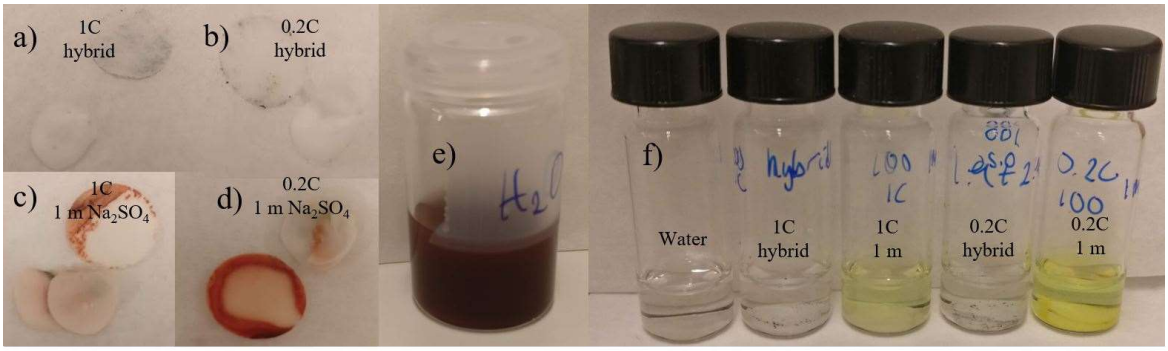

*Figure 34. PTCDA dissolution investigation. a-d) Separators after 100 galvanostatic cycles. The smaller, cut separators were barriers to the RE and the black 'dirt' originates from the AC CE. e) A PTCDA electrode discharged to -0.8 V vs. Ag/AgCl then put in water. f) Separators after a couple of days in 1 ml 2 m NaOH. [**I**].*

The lower water concentration is probably a largely contributing factor in the Hybrid electrolyte, but Yue *et al.* also showed that the dissolution kinetics are highly dependent on the viscosity [160], which is very reasonable since for the process to continue, the dissolved active material needs to be transported away as the electrode/electrolyte interface becomes saturated.

Nimkar *et al*. recently published a response to Paper **I** where they investigate the anion effect on the cycling stability of PTCDA [161]. Their thesis is that the chaotropicity of the anion is one of the most important factors, and that the more chaotropic the anion used is, the better the electrochemical performance. Other than SO_4^{2-}, to our confusion, they applied (to the best of our knowledge) the never-used CO_3^{2-}, the highly corrosive Cl^-, and the costly and unsafe ClO_4^-, at cycling rates of 10 A g^{-1} (*ca.* 73C). To extend their investigation we therefore also want to include anions that are typically used for ASIBs, namely Ac^-, NO_3^-, FSI^-, and $TFSI^-$, that they must have forgotten to investigate from the Hofmeister series. Using these anions and at a more reasonable cycling speed, we unfortunately fail to find any such correlation for PTCDA (Figure 35). On the contrary, in the first few hundred cycles the more kosmotropic anions perform better, yet they all experience severe capacity decay past cycle 500. Nevertheless, it might be so that the 1.0 m electrolyte concentrations are too low for the chaotropic/kosmotropic effects to be distinguishable, considering PTCDA's high solubility in water and the local water stretching signature differences between 1.0 m (Figure 19b) and 8.0-10.0 m [120] (similar trends for aqueous lithium-ion electrolytes in Figure 37b).

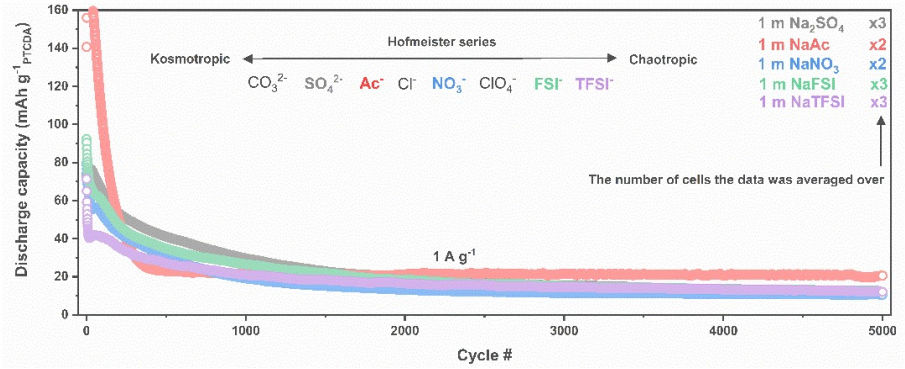

Figure 35. PTCDA cycling stability test with various aqueous electrolytes.

The electrochemical performance of PTCDA was furthermore studied for HSC applications with much higher scan rates [**II**]. The CV analysis using speeds from 1-50 mV s^{-1} reveal a mix of Faradaic (b = 0.5) and non-faradaic (b = 1.0) charge transfer reactions to occur, and/or partly also pseudocapacitive (ideally b = 1.0) [27], as the b-value from Equation 19 equal between 0.5-0.75 (Figure 36a). The fast charge storage is furthermore visualized in the rate capability test with almost all capacity retained up to 10 A g^{-1} (*ca.* 119C calculated based on the practical capacity). The capacity delivered by the electrode is *ca.* 30% more than before and it is attributed to the lower (1/3) electrode mass loading, also making the rather large graphite CC areal weight variance influence the calculated mAh g^{-1}, whereas the power performance of PTCDA is facilitated and made possible by the simple redox reaction involving enolization of the carboxyl group by cation coordination (C=O → C–O-cation) (Figure 36b) [99]. The slower rates do lack a bit of Coulombic efficiency, but we speculate it will improve with longer cycling and by not pairing PTCDA with an oversized AC CE that catalyses the water splitting reactions [162].

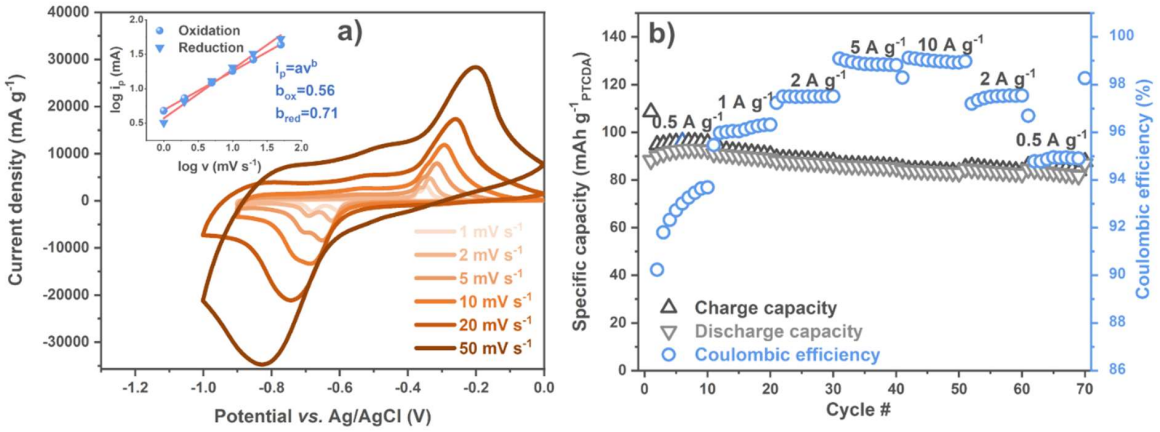

Figure 36. a) Voltammograms and b) rate capability test for the PTCDA electrodes with the Hybrid electrolyte. Inset in a) shows log i_p vs. log v.

4.2.4 PTCDI

The very similar molecule PTCDI, with imide instead of anhydride end groups, was for the first time investigated with aqueous lithium-ion electrolytes [**III**]. Unlike for PTCDA, for which the cycling stability seems solely/mostly to be affected by the electrolyte concentration, the electrochemical performance of PTCDI is also very influenced by the choice of anion (Figure 37a).

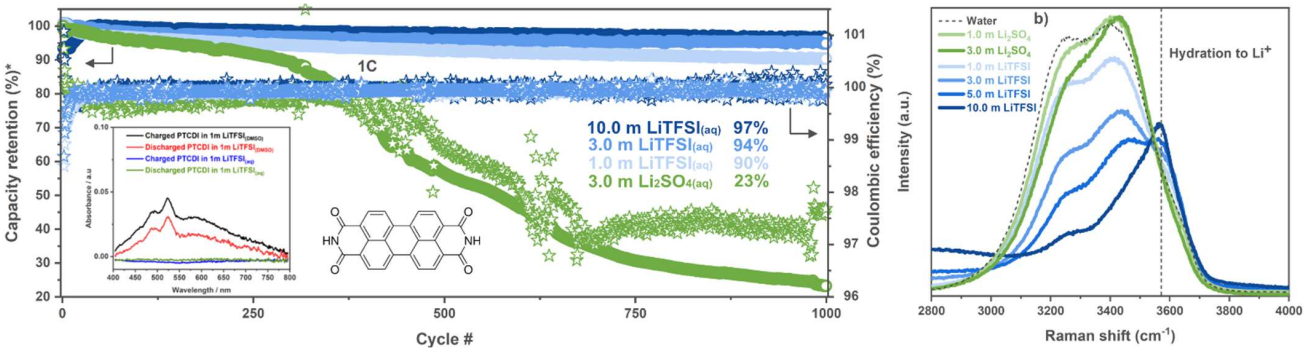

*Figure 37. a) GC long-term stability test of PTCDI electrodes with aqueous electrolytes. Inset shows a UV-Vis solubility test of (dis)charged PTCDI with 1.0 m LiTFSI$_{(DMSO)}$ and 1.0 m LiTFSI$_{(aq)}$, and the molecular structure of PTCDI. * The 10 m LiTFSI$_{(aq)}$ cell's capacity retention was calculated from the 50th cycle. b) Raman spectra in the O-H stretching vibration region of aqueous electrolytes. [**III**].*

While 1.0 m $Li_2SO_{4(aq)}$ barely is cyclable, PTCDI performs quite well up to a few hundred cycles by increasing the concentration to 3.0 m, and when switching anions to TFSI there is almost no capacity loss when approaching WISE concentrations (10.0 m: >100%@1000 from 1st cycle, 97%@1000 from 50th cycle with 1C) (Figure 37a). The electrodes deliver *ca.* 115-120 mAh g^{-1}, and even with 1.0 m the capacity retention is very good (90%@1000 with 1C) with an excellent Coulombic efficiency (>99.75%), and this is mostly attributed to the insolubility of PTCDI with LiTFSI$_{(aq)}$ (inset Figure 37a). The LiTFSI *vs.* Li_2SO_4 outperformance can also be an effect of the changes in the local water structure by the more 'water-breaking' chaotropic [TFSI]$^-$, seen in the Raman spectra as decreased intensity and up shift in wavenumbers of the OH-bands (Figure 37b), disrupting the hydrogen bonded network, and possibly also due to the more hydrophobic [TFSI]$^-$ that does not directly interact as much with the cations and water molecules as the SO_4^{2-} does, but instead can migrate and form a protective hydrophobic layer at the electrode/electrolyte interface preventing electrode detachment [44,161]. Compared with PTCDI using other aqueous electrolytes, LiTFSI$_{(aq)}$ offers one of the best capacity retentions reported so far [102,103,105,163–166], and this is achieved without resorting to the extreme WISE concentrations and at a moderately low cycling rate.

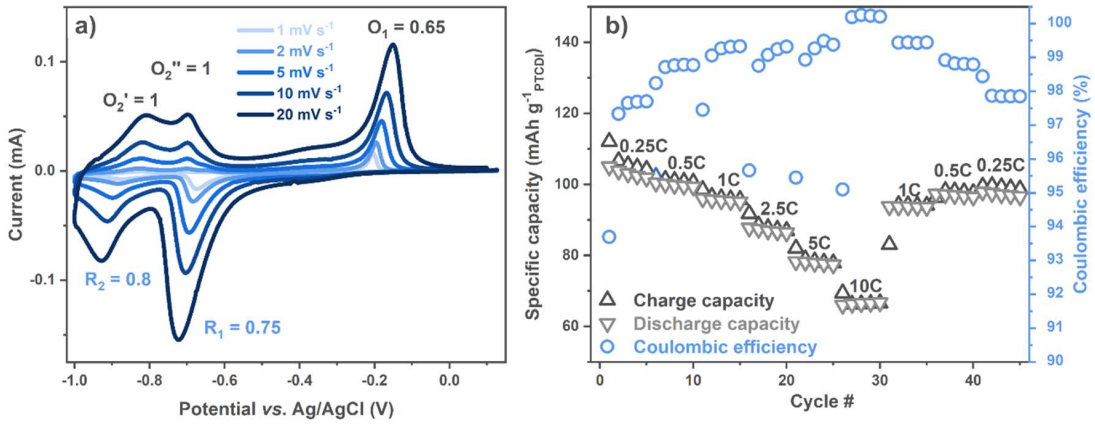

Figure 38. PTCDI electrode a) CV and b*-values, and b) rate capability test with 1.0 m LiTFSI$_{(aq)}$.*

Again, using the linear relations (Eq. 19), *b*-values were extracted and they demonstrate a mixture of current contributions from 1-20 mV s^{-1} (Figure 38a). The first reduction and oxidation peaks are more Faradaic, while the second peaks are more non-faradaic/pseudocapacitive. This is in agreement with previous PTCDI studies using aqueous Na^+ and Zn^{2+} electrolytes [167,168], and the influence of more capacitive/pseudocapacitive reaction mechanisms should enable the PTCDI electrode to have a strong rate performance. The rate capability of PTCDI turns out to be quite good, retaining large amounts of capacity up to 5 and 10C (Figure 38b). While it is worse than for PTCDA, it is very comparable with previous studies using PTCDI with aqueous electrolytes, yet few other studies use C-rates <1C [102,105,164]. It is also possible that the rate performance is affected by the CE, since LFP was used here instead of AC.

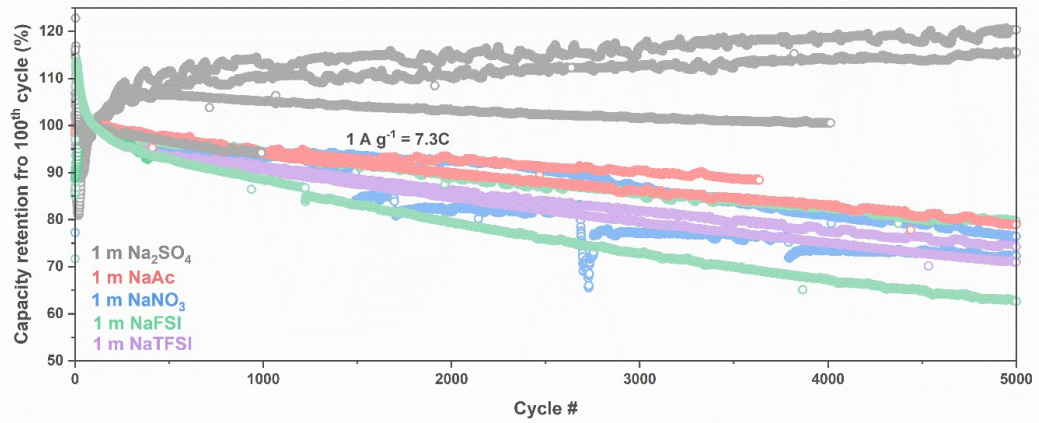

Figure 39. PTCDI cycling stability test with various Na-based aqueous electrolytes.

PTCDI has previously been reported with saturated NaTFSI$_{(aq)}$, a salty & sweet NaTFSI + erythritol electrolyte, and very recently with 1 M $Na_2SO_{4(aq)}$ in full cells [104,167,169], but to the best of our knowledge there are no available data just looking at PTCDI. With this in mind, we also here set out to investigate the anion's effect on the cycling stability for ASIBs. In contrary to with lithium-ions is the significant outperformance of $[TFSI]^-$ *vs.* SO_4^{2-} not present here at all, and instead all the electrolytes cycle very well (Figure 39). For all the electrolytes more and more of the available PTCDI in the electrode seem to be unlocked, or reached by the electrolyte by each successive cycle, and in a rather unusual fashion that process is still ongoing at cycle 5000 for two of the four $Na_2SO_{4(aq)}$ cells, while for the others a maximum

is reached around cycle 20. More cells are certainly needed to confirm if these two are extreme outliers or not. Nevertheless, with sodium cations we can with certainty say that PTCDI has a similar cycling stability irrespective of the anion chaotropicity.

4.2.5 Mn-PBA

Mn-PBA has been subject to extensive investigation and used to create more than a handful of different ASIBs [48,76,80,120,170–172]. It still, however, suffers from transition metal dissolution during cycling, where Jahn–Teller distortion is thought to deform the structure and the disproportionation reaction of Mn^{3+} results in Mn^{2+} dissolution in the electrolyte [173,174]. This results in bad capacity retentions and previously it has only partly been mitigated with WISEs. We, therefore, in paper **IV** set out to find a more sustainable and less costly electrolyte formulation to overcome the dissolution issue and to enable stable cycling of the very promising positive electrode material.

By developing our Hybrid electrolyte into a 'triple electrolyte', by adding a third sulfate salt ($MnSO_4$), the idea was to drive the dissolution reaction backwards in accordance with Le Chatelier's principle [175]. By preparing an electrolyte with pre-dissolved Mn species, the chemical equilibrium of the dissolution reaction should shift in the direction of inhibiting electrode material dissolution [173], and it indeed works like a charm. The triple electrolyte, consisting of the Hybrid electrolyte + 0.3 m $MnSO_4$ showcases excellent cycling stabilities and Columbic efficiencies at both 0.2C and 1C, whereas the Hybrid electrolyte cells display severe capacity decay right from the start and continuing throughout (Figure 40d), more similar to previous studies of Mn-PBA using 17.0 m $NaClO_{4(aq)}$ WISEs [76,170–172].

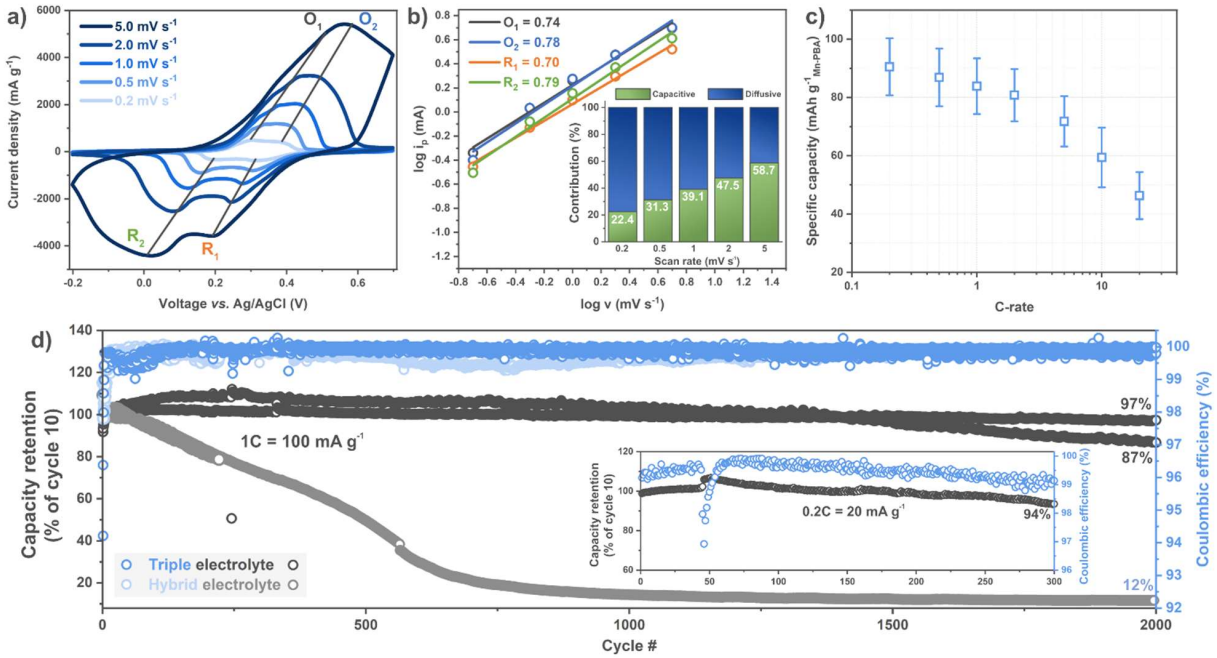

*Figure 40. Mn-PBA electrode (a) voltammogram at different scan rates, (b) the corresponding $\log i_p$ vs. $\log v$, (c) rate capability (mean and standard deviation of 10 cells), and (d) long-term cycling tests with (a–d) the triple and (d) the Hybrid electrolytes. (b and d) Insets show the current contributions at the different scan rates and the long-term cycling at 0.2C, respectively. [**IV**]*

By recovering the cells' separators *post mortem* the instability with the Hybrid electrolyte becomes evident, whereas for the triple electrolyte there are no signs of parasitic side-reactions (Figure 41). ICP-AES was furthermore used to quantify the amount of dissolved material and after 1000 cycles a Hybrid electrolyte cell's separator contained 112 mg Mn. Fe was present in a comparable amount, which also Jiang *et al.* observed, and therefore developing the electrolyte into a quadruple electrolyte could potentially improve the cycling stability even further.

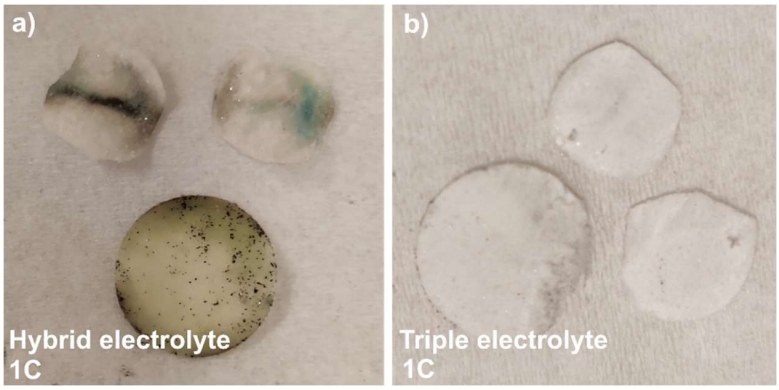

Figure 41. Separators from Mn-PBA half-cells after 200 galvanostatic cycles at 1C. The smaller, cut separators were barriers to the RE and the black 'spots' originates from the AC CE.

Mn-PBA also incorporates a mix of current contributions, with increasingly more capacitive behavior at higher C-rates, and displays a good rate capability up to 20C using the first reaction (Figure 40a-c). Similar to Fe-PBA, Mn-PBA has two redox plateaus and here we only used the first as the second is situated right on the edge of the electrolyte's ESW (Figure 42a). We did, however, witness a peculiar behavior when increasing the cut-off voltage. Over twenty cycles, the first $Fe^{II/III}$ redox reaction gradually diminishes and thereafter the material exchanges electrons mainly *via* the $Mn^{II/III}$ redox pair (Figure 42b). The emerging peaks are positioned very favourably, *ca.* 0.5 V higher compared to the $Fe^{II/III}$ redox reaction and almost entirely within the ESW. Being so close to the ESW edge will, however, inevitably mean some OER to occur and as a result yield lower Coulombic efficiency.

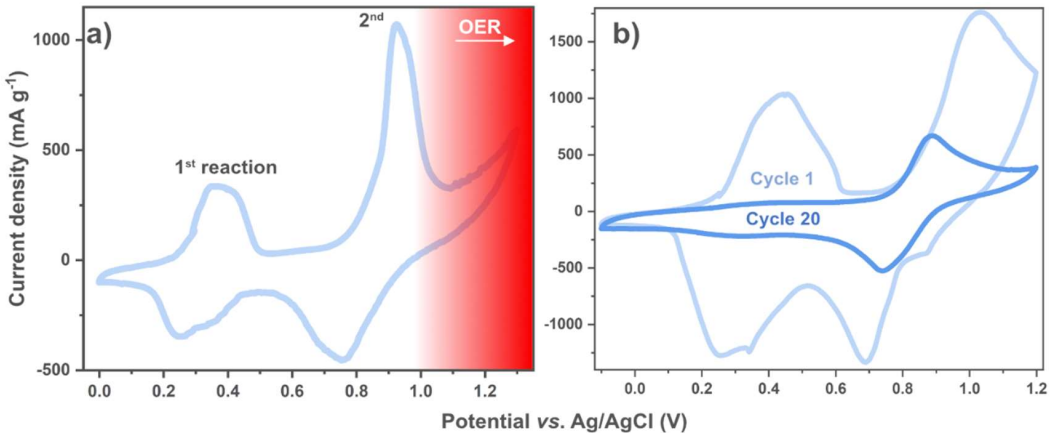

Figure 42. Mn-PBA electrode voltammograms at a) 0.2 mV s^{-1} and b) 1.0 mV s^{-1} with the triple electrolyte.

To sum it up, all the investigated electrodes except NTP perform well with the aqueous electrolytes at hand. More specifically, the Hybrid electrolyte greatly improves electrochemical performance of Fe-PBA, PTCDA, and by adding a third salt Mn-PBA can also be used as a high-performing electrode. PTCDI works well with low-to-medium-concentrated lithium- and sodium-ion electrolytes and it is therefore a very promising negative electrode material for low-cost and sustainable aqueous batteries.

4.3 Reversibility, mechanism, and active charge carrier(s)

To get a deeper understanding about what is happening in the battery cells during cycling, the Mn-PBA, PTCDA, and PTCDI electrodes were investigated further with a series of *ex situ* and *in situ* techniques.

4.3.1 Mn-PBA & PTCDA

First, FTIR is applied to study the oxidation state of the transition metals in the Mn-PBA. The *ex situ* investigation suggest Fe to participate in the redox reaction as the Fe^{II}–CN–Mn^{II} vibration (2070 cm^{-1}) decreases while the Fe^{III}–CN–Mn^{II} band (2145 cm^{-1}) appears after oxidizing (charging) the material (Figure 43a & Figure 44a) [176]. Moreover, a reversible cycling behavior is witnessed with the bands returning to their original states when discharged. Unlike for $K_2Ni[Fe(CN)_6]$ using aqueous K-ion and Mg-ion electrolytes [177], our Mn-PBA does not seem to co-intercalate water during charge as the OH-stretching bands at 2800-3600 cm^{-1} remain unaffected (Figure 43a).

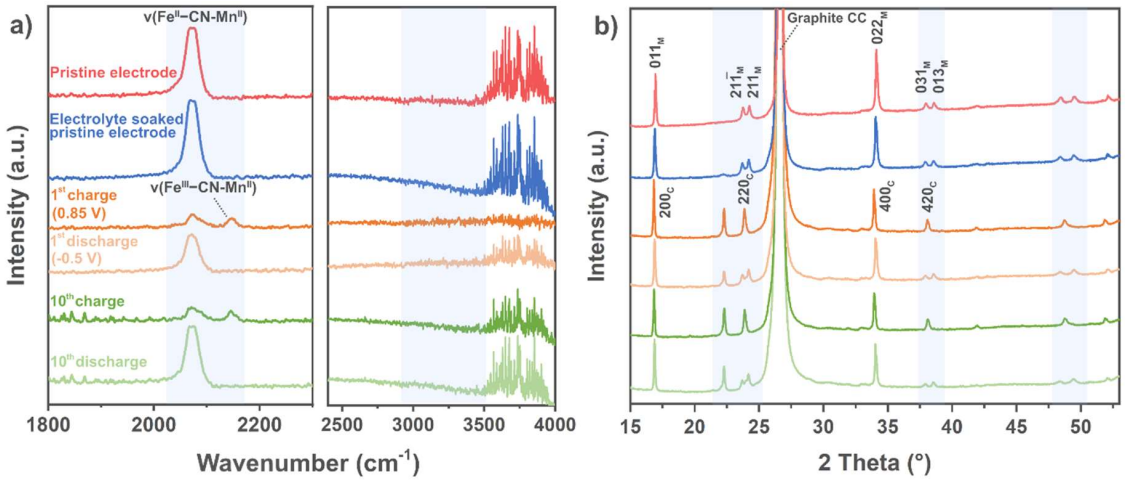

Figure 43. Ex situ *(a) FTIR and (b) XRD of Mn-PBA electrodes cycled by GC with the Hybrid electrolyte. The noisy peaks in (a) originate from the ambient air gases. [**IV**]*

A change from the monoclinic to a cubic phase is revealed during charging in the *ex situ* X-ray diffractograms, where, also, a new peak appears during the first cycle at around 22° (Figure 43b). Its intensity decreases/increases in the following cycles which at first very much confused us, especially since it was not observed for *e.g.* Mn-PBA with (9 m NaOTf + 22 m TEAOTf)$_{(aq)}$ [80]. Graphite has previously been used as a positive electrode material storing anions [167], and the new peak could therefore be due to SO_4^{2-} intercalation into the graphite foil CC. Indeed, and as previously observed [178], sulfate intercalation seems

to occur here as an "empty" piece of CC displays the 22° peak when oxidized, yet the process should be of no concern since the capacity is very insignificant (Figure 44bc). Reassuringly, the *ex situ* XRD data also point to a reversible cation (de)intercalation process with the highlighted peaks changing accordingly (Figure 43b).

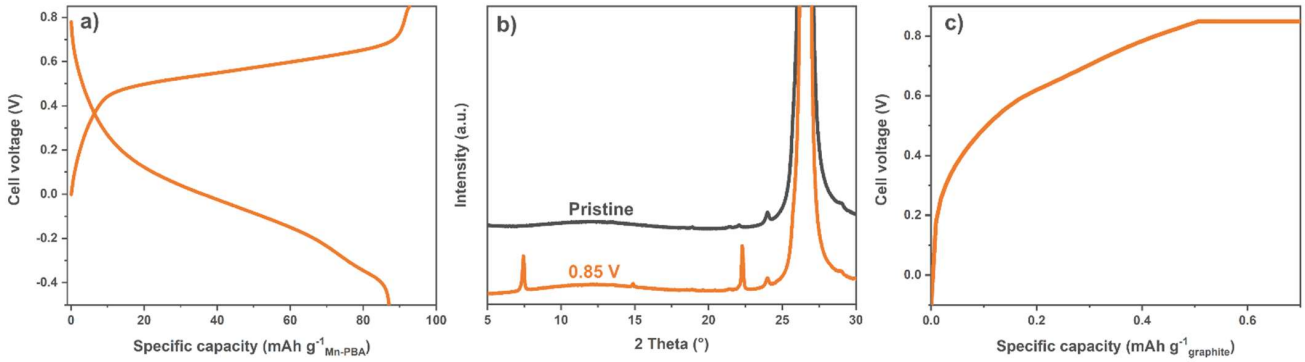

Figure 44. a) Typical charge/discharge curves for the Mn-PBA ex situ *characterizations using a two electrode AC||Mn-PBA pseudo half-cell. b) X-ray diffractograms of pristine and oxidized graphite current collectors and c) the corresponding voltage profile (right). **[IV]***

Although its organic nature, PTCDA orders itself in a crystalline structure and can therefore also be studied with XRD. The *ex situ* investigation suggests both reversible and irreversible structural changes to occur. More specifically, during charge the 9.5° peak almost completely disappears and a new broad peak emerges at lower angles, similar to with non-aqueous electrolytes (Figure 45) [179]. When charging the electrode, the 9.5° peak reappears, whereas parts of the new broad peak remain during discharge. The latter indicates an irreversible change that previously has been associated with the PTCDA activation in the initial cycle(s) [99], which is in accordance with the irreversible capacity of the first charge (Figure 32b).

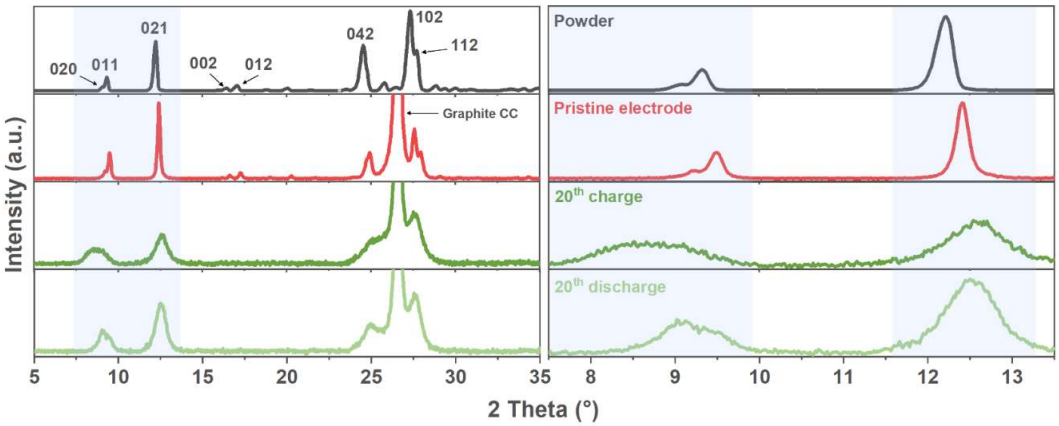

*Figure 45. XRD diffractograms (shifted and not in scale w.r.t. intensity) of the PTCDA powder (black), the pristine electrode (red), and electrodes in discharged (blue) and charged (green) states after 20 CV cycles. **[II]***

The *ex situ* FTIR spectra of PTCDA point to the oxygen of the carbonyl groups to be interacted with in the charged states, seeing that the C=O vibration intensity at *ca.* 1770 cm^{-1} decreases/increases during charge/discharge (Figure 46), and previously attributed to an enolization reaction (C=O → C–O-cation) [99]. The signal to noise ratio of the cycled electrodes is not amazing, however, a lot of the diminished peak intensities seen in the charged states are recovered during discharge which allude to a reversible charge

storage. Moreover, the spectrum at the 1st discharge is a bit different compared to the pristine electrode and suggests structural changes to have occurred, possibly due to the material activation where cations partially remain.

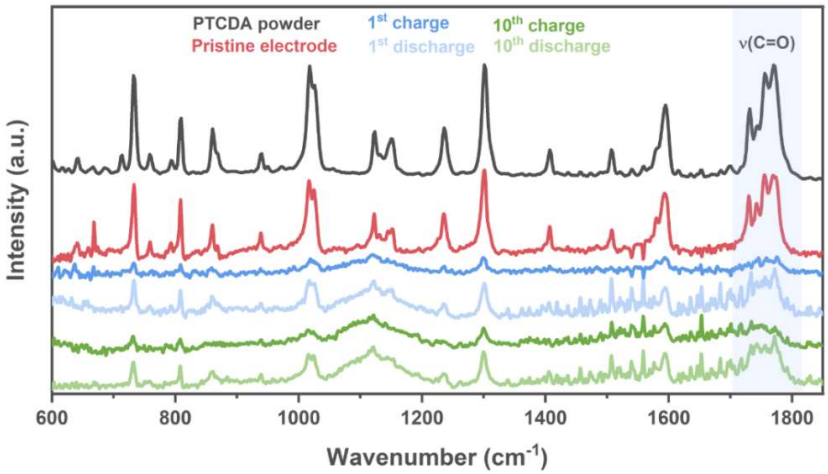

Figure 46. FTIR spectra of PTCDA powder and electrodes cycled with the Hybrid electrolyte, cycled with GC Ex situ*. The noisy peaks in originate from the ambient air gases.*

Continuing, the Nernst equation can be used to predict the potential shift of a redox reaction as a function of charge carrier concentration, according to $\Delta V_{Nernst} = \frac{RT}{zF} ln \frac{C_1}{C_2}$. At room temperature, *active* mono/divalent charge species are expected to shift the reaction +59/29 mV per logarithmic decade of increasing salt concentration. By using CV and looking at the peak position(s) of the redox reaction(s), the increasing amounts of charge carriers in the electrolytes point to neither Mn-PBA nor PTCDA to involve protons in the charge transfer as the redox potentials remain constant when changing the [H^+] by more than x10000 (Figure 47ad). This is unlike some other PBAs [177] and PTCDA with 1 M $H_2SO_{4(aq)}$ (pH<1) [107], but we do not find it implausible as our conditions are certainly milder, and by having additional charge carriers present, here Na^+ and Mg^{2+}, the selectivity/competitiveness of proton intercalation has previously been witnessed to drastically decrease [169].

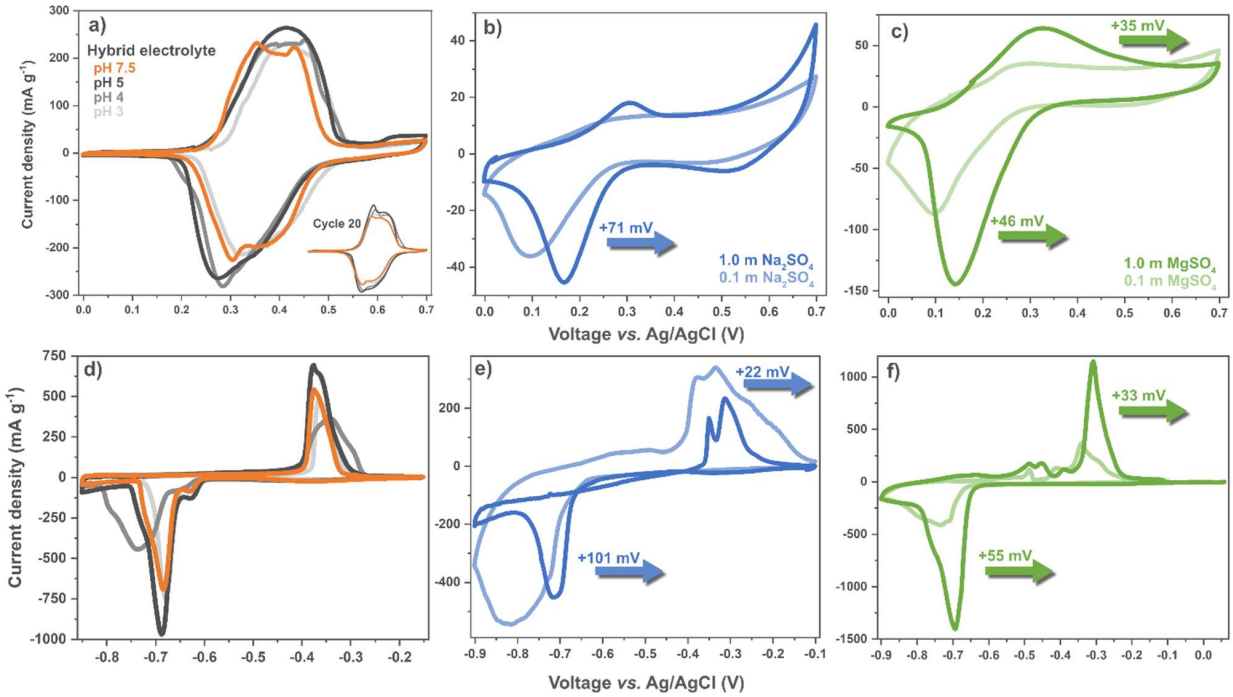

Figure 47. a-c) Mn-PBA and d-f) PTCDA electrode voltammograms (cycle 1, 0.2 mV s^{-1}) at different ad) pH, be) [Na^+], and cf) [Mg^{2+}]. Inset in a) shows cycle 20.

The CV studies instead suggest that Mn-PBA and PTCDA (de)intercalate Na^+ and Mg^{2+}, as the redox potentials shift roughly in line with the Nernst equation (Figure 47bcef). A bit of discrepancy from the approximation is to be expected since the 1.0 m concentrations exceed the dilute regime (activity coefficients ≠ 1) and we also pass a net current through the electrodes which affects the activity and introduce overpotential and resistive loss terms. Interestingly both electrodes have low current densities when the electrolyte only contains Na_2SO_4. They seem to require the more chaotropic Mg^{2+} and/or a higher amount of charge carriers to accommodate more extensive redox reactions.

4.3.2 PTCDI

Last but not least, we continue the study of PTCDI and begin with applying FTIR to gain insights on the vibrations of the functional groups – to understand the material changes (if any) at different SOC and to elucidate what redox mechanism occur. By reducing (charging) PTCDI, there are shifts and intensity changes throughout most of the spectra. The large reduction of the C=O and aromatic C–H bands as well as the red shift of the perylene band point to an enolization reaction of the carbonyl group (C=O → C–O-cation) and a decreased π-electron delocalization of the conjugated rings by cation coordination, as previously observed (Figure 48a) [180]. During discharge most bands recover their peak intensities and positions, indicating de-enolization and a reversible redox reaction. However, by overlaying the spectra a slight difference is seen; the 1685 cm^{-1} C=O band merging to a single peak is similar to with organic electrolytes [181], and the new peak positioned at 1065 cm^{-1} that remains during discharge has previously been ascribed to a C–O bond (Figure 48b) [182]. At the same time, the intensity decrease of the C=C vibration (875 cm^{-1}) suggests a potential change to the delocalization of the structure (Figure 48b). These

spectral changes between the pristine and the following discharged states, also taking into account the irreversible capacity of the first cycle (inset Figure 48b), indicate that some Li^+ remain during discharge, and similar to PTCDA this is probably connected to the PTCDI electrode activation.

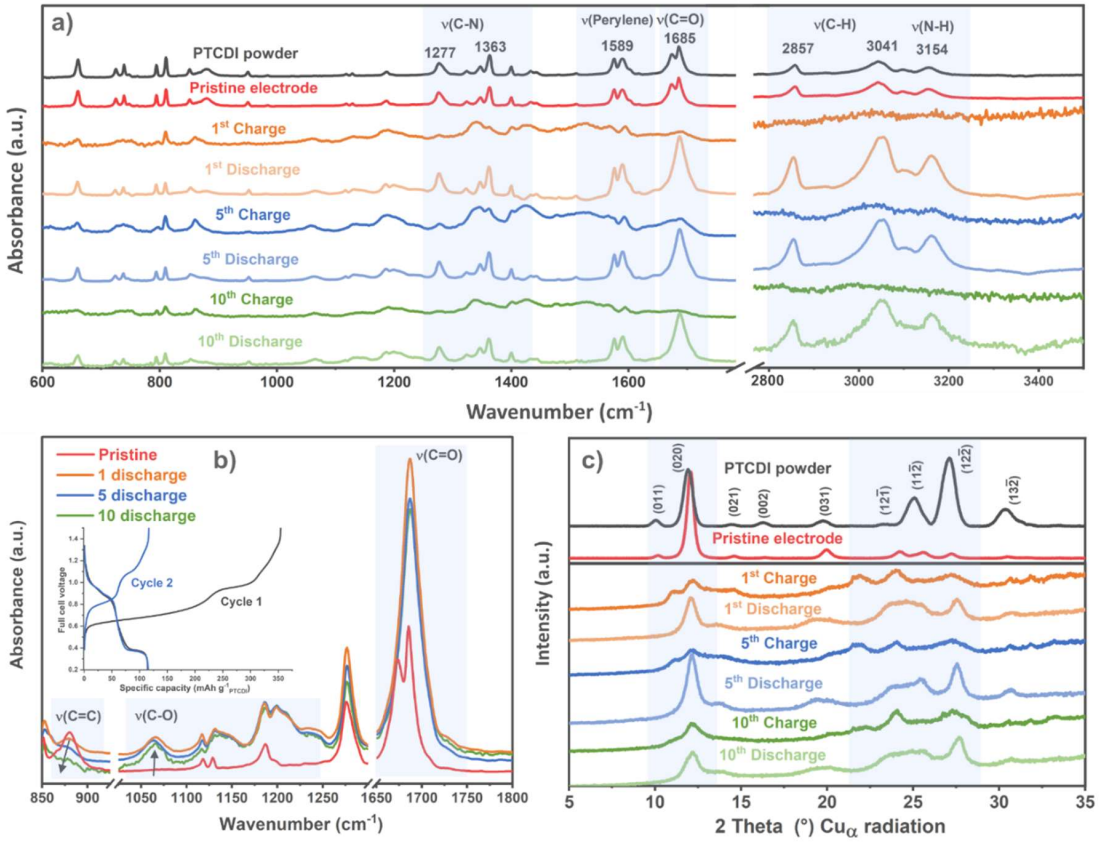

Figure 48. Ex situ *FTIR spectra in the a) 600-3500 cm^{-1} and b) 850-1800 cm^{-1} region, and c)* ex situ *X-ray diffractograms of free-standing PTCDI electrodes cycled with 1.0 m $LiTFSI_{(aq)}$. Inset in b) shows the 1st and 2nd GC cycle of a PTCDI||LFP cell.*

The *ex situ* diffractograms display the already quite broad peaks to shift and become even broader, indicating a loss of crystallinity during charge when ions are intercalated/coordinated. They all, however, return to their original positions after discharge, displaying good reversibility. A slight change between the pristine and the following discharged patterns is observed, and this we attribute to a slight alteration in the crystal structure but whether it originates from the activation process or pre-measurement cleaning remains an open question.

Which charge carrier(s) that participate in the charge storage mechanism was further investigated by *in situ* EQCM-R and by monitoring the Nernstian peak shifts with CV. The former measures the motional resistance and frequency fluctuations of the WE and can be correlated to a mass increase/decrease of the electrode during cycling. In the first cycle, a large irreversible frequency decrease/mass increase is seen with 1.0 m $LiTFSI_{(aq)}$ and 1.0 m $Li_2SO_{4(aq)}$ which we attribute to electrode swelling by the electrolyte [183] and/or the structural activation of PTCDI involving irreversibly intercalated ions (Figure 49ad).

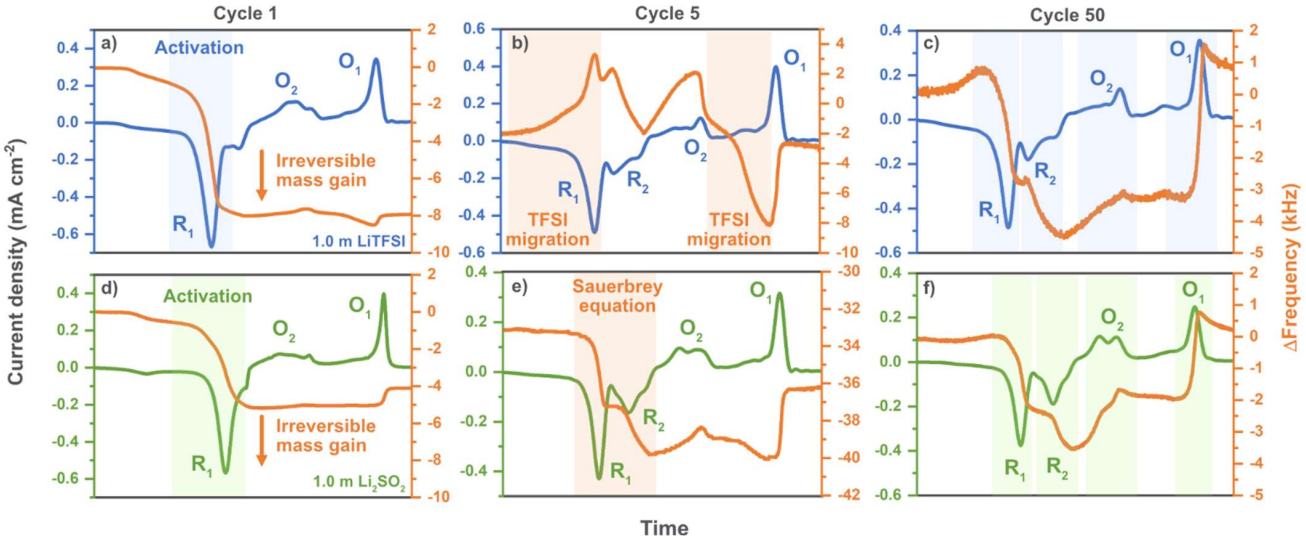

Figure 49. PTCDI EQCM response of the ad) 1st, bc) 5th, and cf) 10th CV cycle at 5 mV s^{-1} with a-c) 1.0 m $LiTFSI_{(aq)}$ and d-f) 1.0 m $Li_2SO_{4(aq)}$. $O_{1,2}$ and $R_{1,2}$ are the 1st and 2nd oxidation and reduction peaks, respectively.

By cycle 5 the TFSI-based electrolyte displays an unexpected response for R_1/O_1: mass loss during reduction and mass gain during oxidation, indicating a process not involving typical cation (de)intercalation/coordination (Figure 49b). Or put in other words, the electrode loses mass when cation intercalation is expected and thereafter gains mass when cation deintercalation is expected. Instead, we theorize it is due to the more hydrophobic/chaotropic nature of $[TFSI]^-$, which makes it interact less with the cations and the water molecules, and rather migrates to and from the electrode surface to charge compensate. A recently study with PTCDA in dilute sodium-ion electrolytes showed that chaotropic anions had a much larger presence at the electrode surface compared to the more kosmotropic anions [161], and in our case the electrostatic interactions between PTCDI and $[TFSI]^{-1}$ could be the origin of the unexpected mass changes in cycle 5. Especially as it does not occur for the kosmotropic SO_4^{2-} (Figure 49e). Nevertheless, by cycle 50 the EQCM responses represent typical two-step cation (de)intercalation/coordination processes with both electrolytes (Figure 49cf). In the 5th cycle with $Li_2SO_{4(aq)}$ the Sauberey equation (Eq. 11) is applicable since $\Delta f/\Delta R_m > 25$ Hz/Ω, whereas for lower ratios the mass-frequency linearity can be disrupted and make the approximation invalid [124,125]. The calculated "molecular weights" equal to 71 g mol^{-1} and 75 g mol^{-1} for R_1 and R_2, respectively, which likely correspond to the weights of solvated Li^+ with 3.6 and 3.8 water molecules on average, remembering that the Li^+ coordination number in aqueous solutions is 4 [184].

Continuing, and as we saw for PTCDA, PTCDI does not seem to involve protons as active charge species either when another cation is present in the electrolyte, considering no clear up-shift is observed when changing the $[H^+]$ by two orders of magnitude (Figure 50). In contrast, the $[LiTFSI_{(aq)}]$ increase from 1.0 to 3.0 m results in +16 mV (+12 mV expected), +30 mV (+23 mV expected) and +30 mV (+23 mV expected) for R_1, O_1, and O_2, respectively. Similarly, for $Li_2SO_{4(aq)}$ the shifts are +5 mV (+13 mV expected), +30 mV (+26 mV expected) and +30 mV (+26 mV expected) for R_1, O_1, and O_2, respectively. Altogether, these CV studies monitoring the mass and redox potential changes strongly point to Li^+ being the active charge carrier, and as no other species are present, we must conclude solvated Li^+ to single-handedly participate in the redox reactions with PTCDI using aqueous electrolytes.

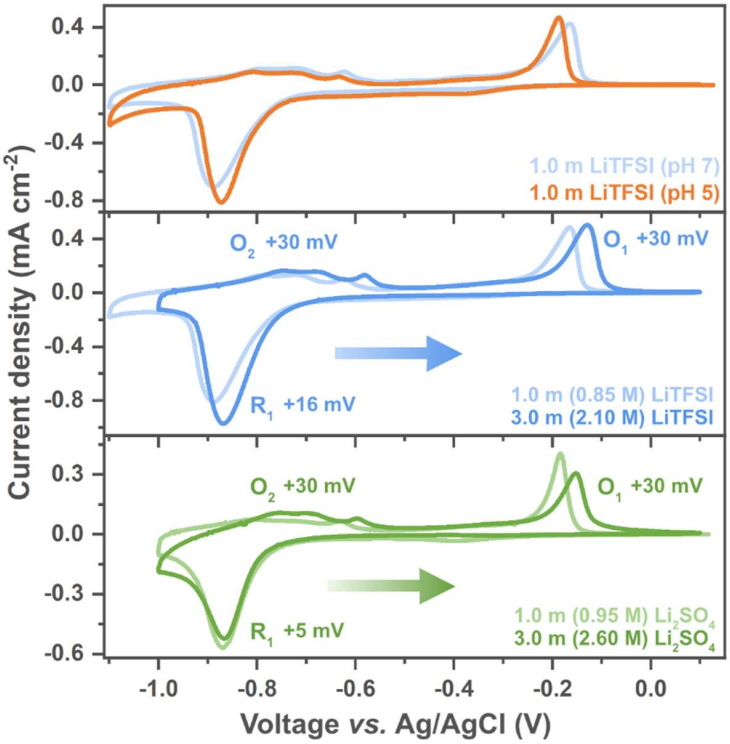

Figure 50. 1st CV cycle of PTCDI with different a) pH, b) [$LiTFSI_{(aq)}$] and c) [$Li_2SO_{4(aq)}$].

4.4 Electrochemical full cells

Here in the final part of the thesis we pair the studied electrodes to create novel cell chemistries and evaluate their electrochemical performance. Considering the promising rate capability of PTCDA seen in Chapter 4.2.3 , PTCDA||AC cells are assembled to assess how well the material can perform in a HSC. A 1:3-3.5 electrode weight ratio is used to balance the capacity, and the cells deliver a capacity of *ca*. 22 mAh $g^{-1}_{PTCDA+AC}$ at 0.5 A g^{-1} after the activation process (Figure 51a). The large weight of the AC electrode does limit the capacity, yet the cycling stability is on par or exceeds that of the best comparable all-organic aqueous energy storage devices in the literature, having 86%@1000 with 1 A g^{-1} from the 10th cycle with a Coulombic efficiency >98.5% [95,116,185–187] (Figure 51c).

From the Nyquist plot, and by implementing the simple and commonly used Randles circuit cell model, slightly modified with constant phase elements to appropriately fit the data, the charge-transfer resistance (R_{ct}, 18.3 Ω cm^{-2}) and the electrolyte resistance (R_s, 2.1 Ω cm^{-2}) were extracted before cycling (Figure 51b). The former drastically decreases after cycling, indicating that the activation process improves the charge transport kinetics and conductivity. The energy and power densities are for the HSC 17 Wh $kg^{-1}_{PTCDA+AC}$ (at 0.5 A g^{-1}) and 4.5 kW $kg^{-1}_{PTCDA+AC}$ (at 50 A g^{-1}), respectively, performing in between the typical aqueous batteries/supercapacitors (Figure 54c). It is by no means as well performing as the PNTCDA||carbon microspheres Na-HSC mentioned in Chapter 2.5, yet it was never the intention since we here aim to prioritize the cost and sustainability by exclusively using organic materials. We acknowledge that neither water nor the salts used are organic, but the point pushed is the implication that these are safer, lower cost, and more sustainable/ecological.

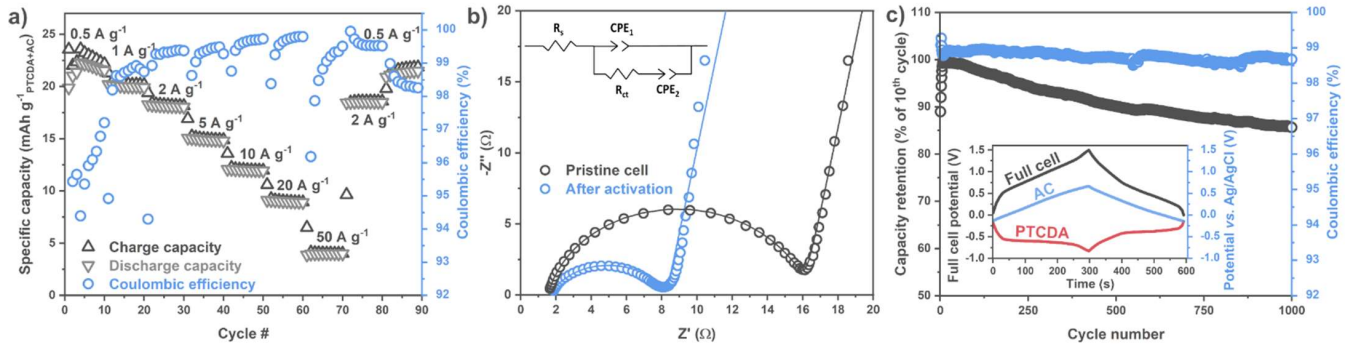

*Figure 51. a) Rate capability test, b) Nyquist plot of the HSC with a modified Randles circuit, and c) GC stability test at 1 A g^{-1} with the Hybrid electrolyte. Inset in c) shows the corresponding charge/discharge curves of the 100th cycle. **[II]**.*

With the hopes of simplifying the EOL, the biodegradability of the all-organic device was evaluated and after 4 weeks in a kitchen pre-compost *Bokashi 2.0* the original structure was intact. After 8 more weeks dug down in soil the separator and parts of the electrode were degraded, whereas the graphite CCs remained unaffected (Figure 52). Considering that cellulose filter paper and CMC are known to biodegrade, whereas PTCDA is classified as "not rapidly biodegradable" (OECD 301F test), these observations are in line with previous knowledge [188,189]. Moreover, graphite is one of carbon's most stable allotrope and AC is a known biodegradation catalyst, why 8 weeks is probably far too short of a time frame to expect any substantial degradation [190]. As a conservative estimation we approximate the degree of biodegradation with the separator's weight, equal to -13%, and an energy storage device completely biodegradable within a reasonable time frame therefore probably cannot consist of neither graphite CCs nor AC electrodes.

*Figure 52. a 5 x 5 cm HSC (left) before and (right) after the biodegradability test. **[II]***

With the intention to increase the capacity and energy density, the organic active materials polyaniline, polypyrrole, poly(3-vinyl-N-methylphenothiazine), and a few oxalates and triflimides were made electrodes with and considered at the positive side. Unfortunately, no all-organic batteries were made since all of them failed in at least one of the following aspects: *i*) to be compatible with the electrode fabrication process, *ii*) have stable cycling, *iii*) have more capacity than AC, or *iv*) have a redox potential 0.2-0.8 V *vs*. Ag/AgCl. To not give up on the overarching aim of making functional battery cells we therefore decided to broaden the scope and also allow the less costly and more benign transition metals Fe and Mn in the positive electrode.

Consequently, AC was swapped out for Fe-PBA, and the first cycle of the Fe-PBA half-cell reveals the structure to only partially be filled with Na^+ which should affect the balancing and performance of the full cell (Figure 53c), yet, with an 1:1 electrode weight balancing (PTCDA:Fe-PBA) it performs surprisingly well (Figure 53ab). After a few initial cycles at 5C the capacity stabilizes, most likely incorporating excess cations from the electrolyte, and the cell delivers a capacity almost double that of the PTCDA||AC HSC (>40 mAh $g^{-1}_{PTCDA+Mn-PBA}$). However, even when a part of the 2nd redox plateau is used the voltage remains rather low, limiting the energy density to 20 Wh $kg^{-1}_{PTCDA+Mn-PBA}$ (Figure 53a). Slower cycling was accompanied by severe OER resulting in (even) lower Coulombic efficiencies than for 5C, and a decreased cycling stability. We therefore decided to look for alternative candidates to pair PTCDA with.

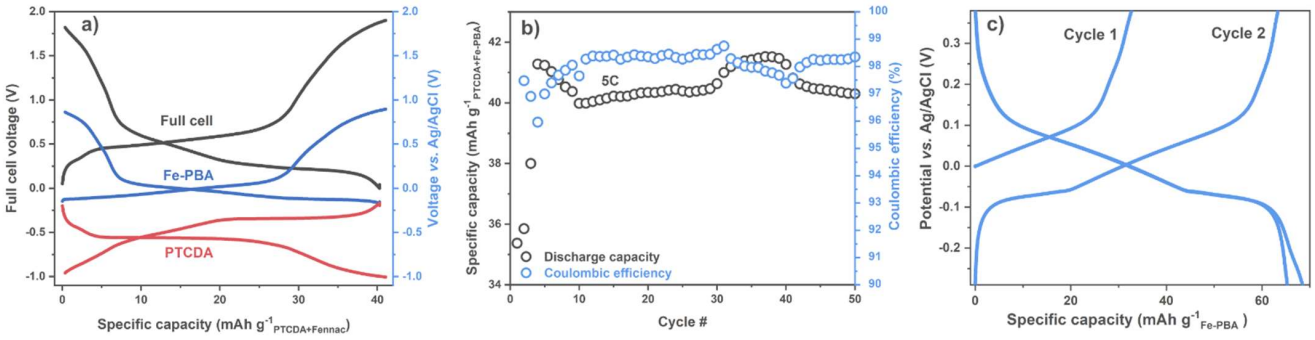

Figure 53. GC a) charge/discharge curves of the 10th cycle and b) the cycling stability of PTCDA||Fe-PBA with the Hybrid electrolyte. c) AC||Fe-PBA half-cell at 0.2C with the hybrid electrolyte. All in Swagelok cells.

Considering the promising characteristics of Mn-PBA, *i.e.* the "very low" critical raw material risk classification of Mn [18], the high capacity, good rate performance, well positioned redox plateaus, and the improved cycling stability with the triple electrolyte, it seemed like an appropriate choice as positive electrode to pair with PTCDA. When cutting the voltage at 1.3-1.5 V to exclude the 2nd redox reaction, the PTCDA||Mn-PBA cells deliver *ca.* 35 mA h $g^{-1}_{PTCDA+Mn-PBA}$ at 0.2C, and they display an excellent cycling stability with the triple electrolyte at both 1C (86%@1000, n = 3) and 0.2C (89%@800, n = 2) with Coulombic efficiencies ≥99.5% (Figure 54a). The large standard deviation is due to the graphite CC areal weight variance. Moreover, they retain a large amount of capacity even up to 20-50C, slightly better than previous Mn-PBA batteries [48,80,171,172], and this we attribute to either the good rate capability of PTCDA, not acting as a bottle neck, and/or the lower electrolyte concentration applied here compared to WISEs, which should enable faster charge/discharge rates due to the lower viscosity and higher ionic conductivity (Figure 54b). The energy density and power density are 35 Wh $kg^{-1}_{PTCDA+Mn-PBA}$ at 0.2C and 1700 W $kg^{-1}_{PTCDA+Mn-PBA}$ at 50C, respectively. In terms of energy dense cells this PTCDA-combination performs the best so far, and are in the same range as previously reported PBA-based ASIBs (Figure 54c) [73–76,80,120,170,171], while the latter also highlights the suitable electrochemical traits of Mn-PBA and PTCDA, capable of both energy and power.

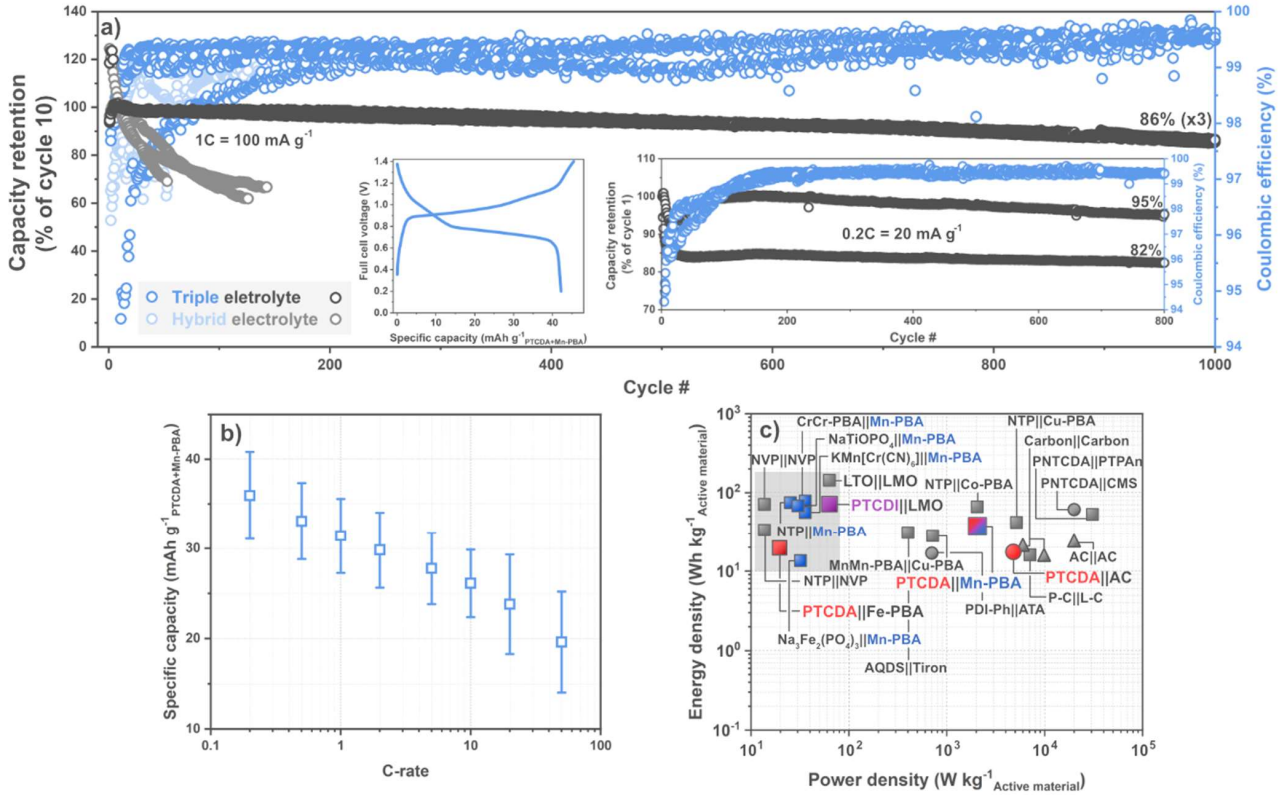

*Figure 54. a) Long-term cycling and b) rate capability of PTCDA||Mn-PBA (mean and standard deviation of 8 cells) with a-b) the triple and a) Hybrid electrolytes. c) Ragone plot of aqueous metal-ion energy storage devices. Square = battery, circle = HSC, and triangle = supercapacitor. Left and right a) insets show the typical charge/discharge curves at 0.2C and the long-term cycling performance at 0.2C, respectively. The grey area papers in c) did not report a powder density. [**IV**].*

The cell voltage without the 2nd reaction is similar to the $NaTi_2(PO_4)_3$ | 32 m KAc + 8 m NaAc | Mn-PBA and the $Na_3Fe_2(PO_4)_3$ | 17 m $NaClO_4$ | Mn-PBA chemistries [48,170], but in general in the lower range of previous Mn-PBA batteries as they tend to use both reactions (inset Figure 54a). If desired, however, the voltage can be tuned. As we saw in the cyclic voltammogram, by increasing the cut-off voltage the 1st redox reaction involving $Fe^{II/III}$ gradually decreases, and by cycle 20 Mn-PBA exchanges electrons mainly *via* the $Mn^{II/III}$ redox pair (Figure 42b). This greatly increases the cell voltage, but at the same time decreases the Coulombic efficiency due to some OER (Figure 55). Similar to with Fe-PBA, to cycle these cells with a high cut-off voltage in a Coulombic efficient manner requires further electrolyte modification to expand the oxidation stability a couple of hundred millivolts.

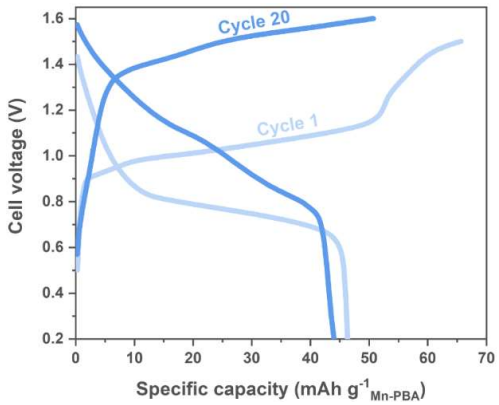

*Figure 55. PTCDA||Mn-PBA charge/discharge curves at 1C with the triple electrolyte. **[IV]**.*

Last out, PTCDI is paired with LMO and cycled with 1.0, 3.0, and 5.0 m $LiTFSI_{(aq)}$ to explore the possibility of implementing PTCDI for ALIBs. To not too much of a surprise does the latter cell have the best cycling stability of the three, and the not-so-good capacity retention is attributed to the instability of LMO – experiencing Mn dissolution during cycling [191,192] (Figure 56). The PTCDI||LMO chemistry performs very similarly to the best performing WISE SIBs having an average discharge voltage of 1.47 V, 71 Wh $kg^{-1}_{(PTCDI+LMO,\ 10th\ cycle)}$, and a capacity retention of 74%@500 at 1C with 'only' a 5.0 m concentration (Figure 56 & Figure 54c). Yet, it is not very competitive in comparison to recent 'aqueous' co-solvent LIBs using $Li_4Ti_5O_{12}$ at the anode side, as they have *ca.* 2.5 V and double the energy density [62,63]. Nevertheless, such batteries require heavily engineered electrolytes to cycle in a stable manner and high purity Ti-precursors, both coming with large price tags, and to some extent their design more resemble traditional LIBs as compared to the lower cost and more sustainable energy storage device that the aqueous battery was thought to be.

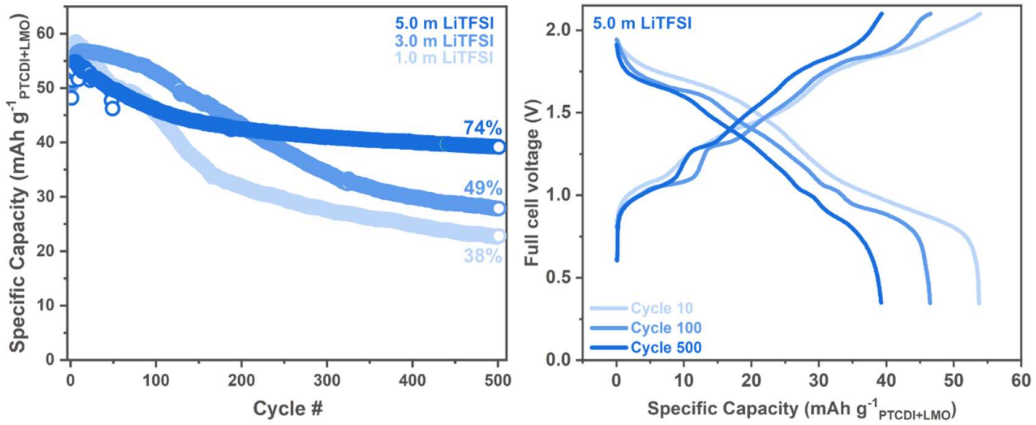

Figure 56. 1C long-term cycling of balanced PTCDI||LMO full cells and the corresponding potential curves for 5.0 m $LiTFSI_{(aq)}$.

5 | Conclusions & Outlook

In all we here, by direct design of new materials and components, show AMIBs to be well-functioning and a promising avenue to develop more sustainable energy storage.

In further detail, the herein developed aqueous hybrid electrolytes display promising physico-chemical properties and more importantly can be used together with several active materials to improve their electrochemical performance. Not only to increase their rate retention, but also to enable slow rate and long-term cycling. The latter is also achieved for Mn-PBA by taking advantage of le Chatelier's principle, and altogether this is done without resorting to the extreme concentrations of WISEs or co-solvent strategies.

The ion intercalation/coordination selectivity of Li^+/ Na^+/ Mg^{2+} for PTCDA, PTCDI, and Mn-PBA seems to be favoured over protons, even under acidic conditions, and the corresponding redox mechanisms are fast and reversible – making the electrodes suitable for both batteries and HSCs. The cycling stability of the organic molecules, in stark contrast to previous studies, is not unanimously affected by the anion chaotropicity, but instead it is very active material and cation dependent. Finally, the herein assembled PTCDA & PTCDI based AMIBs/HSCs work well and exhibit excellent long-term stabilities – while admittedly they have slightly limited energy densities compared to the state-of-the-art. Still, by assembling them with constituents of solely benign character the aim of the thesis has been achieved, *i.e.* to create unconventional energy storage devices using more sustainable materials.

Going forward, more work can be done on the electrolyte and positive electrode side. For example, finding an organic positive electrode active material to create an *all*-organic AMIB is yet to be done, and if not found, an attempt can be made to expand the electrolyte oxidation stability to improve the cell energy densities by enabling the use of the PBAs' 2^{nd} redox reaction in a Coulombic efficient manner. Lastly, the next development-oriented step would be to go from the Swagelok and coin-cells used herein to larger prototype pouch cells, with the intention to increase the absolute capacity so that currents needed for practical applications can be drawn from the cells.

6 | Acknowledgements

First of all, I would like to express my appreciation towards the Swedish Research Council for Sustainable Development (FORMAS) and the Swedish Research Council (VR) for supporting this work.

I very much thank my supervisor Prof. Patrik Johansson for giving me the opportunity to be a part of his excellent research group, for giving me the freedom and resources to pursue my ideas, and for supporting me with knowledge and insights both inside and outside of the academic world.

I would also like to give a special thank you to Dr. Roza Bouchal and Dr. Ezio Zanghellini, for helping me getting started, for your expertise, your patience and for always helping me in the lab, even though I am a bit stubborn… I could not have done this without you!

A shoutout to my great colleagues for making the weeks fly by, for putting up with me and my stupid jokes, and of course to my friends for making life very enjoyable!

Finally, to my family, whom I never see nearly enough. Thank you for all the love and support throughout the years, I am truly grateful for everything.

7 | Bibliography

[1] S. Wang, Q. Li, C. Fang, C. Zhou, The relationship between economic growth, energy consumption, and CO2 emissions: Empirical evidence from China, Sci. Total Environ. 542 (2016) 360–371. https://doi.org/10.1016/j.scitotenv.2015.10.027.

[2] Data overview - IEA, (n.d.). https://www.iea.org/data-and-statistics (accessed November 3, 2021).

[3] UN, Transforming Our World by 2030: A New Agenda For Global Action, 2015.

[4] B. Dunn, H. Kamath, J.M. Tarascon, Electrical energy storage for the grid: A battery of choices, Science (80-.). 334 (2011) 928–935. https://doi.org/10.1126/science.1212741.

[5] H. Pan, Y.S. Hu, L. Chen, Room-temperature stationary sodium-ion batteries for large-scale electric energy storage, Energy Environ. Sci. 6 (2013) 2338–2360. https://doi.org/10.1039/c3ee40847g.

[6] M.S. Ziegler, J.E. Trancik, Re-examining rates of lithium-ion battery technology improvement and cost decline, Energy Environ. Sci. 14 (2021) 1635–1651. https://doi.org/10.1039/D0EE02681F.

[7] Democratic Republic of Congo: "This is what we die for": Human rights abuses in the Democratic Republic of the Congo power the global trade in cobalt | Amnesty International, (n.d.). https://www.amnesty.org/en/documents/afr62/3183/2016/en/ (accessed September 8, 2021).

[8] L.J. Vimmerstedt, S. Ring, C.J. Hammel, Current status of environmental, health, and safety issues of lithium ion electric vehicle batteries, Golden, CO, 1995. https://doi.org/10.2172/135056.

[9] A. Hammami, N. Raymond, M. Armand, Runaway risk of forming toxic compounds, Nat. 2003 4246949. 424 (2003) 635–636. https://doi.org/10.1038/424635b.

[10] D. Larcher, J.M. Tarascon, Towards greener and more sustainable batteries for electrical energy storage, Nat. Chem. 7 (2015) 19–29. https://doi.org/10.1038/nchem.2085.

[11] UPDATE-T&E's analysis of electric car lifecycle CO_2 emissions by Transport & Environment, 2022.

[12] N. Tapia-Ruiz, A.R. Armstrong, H. Alptekin, M.A. Amores, H. Au, J. Barker, R. Boston, W.R. Brant, J.M. Brittain, Y. Chen, M. Chhowalla, Y.-S. Choi, S.I.R. Costa, M.C. Ribadeneyra, S.A. Cussen, E.J. Cussen, W.I.F. David, A. V Desai, S.A.M. Dickson, E.I. Eweka, J.D. Forero-Saboya, C.P. Grey, J.M. Griffin, P. Gross, X. Hua, J.T.S. Irvine, P. Johansson, M.O. Jones, M. Karlsmo, E. Kendrick, E. Kim, O. V Kolosov, Z. Li, S.F.L. Mertens, R. Mogensen, L. Monconduit, R.E. Morris, A.J. Naylor, S. Nikman, C.A. O'Keefe, D.M.C. Ould, R.G. Palgrave, P. Poizot, A. Ponrouch, S. Renault, E.M. Reynolds, A. Rudola, R. Sayers, D.O. Scanlon, S. Sen, V.R. Seymour, B. Silván, M.T. Sougrati, L. Stievano, G.S. Stone, C.I. Thomas, M.-M. Titirici, J. Tong, T.J. Wood, D.S. Wright, R. Younesi, 2021 roadmap for sodium-ion batteries, J. Phys. Energy. 3 (2021) 031503. https://doi.org/10.1088/2515-7655/AC01EF.

[13] V.A. Oltean, S. Renault, M. Valvo, D. Brandell, Sustainable materials for sustainable energy storage: Organic Na electrodes, Materials (Basel). 9 (2016). https://doi.org/10.3390/ma9030142.

[14] A. Richelli, M. Salem, L. Colalongo, A Review of Fully Integrated and Embedded Power Converters for IoT, Energies 2021, Vol. 14, Page 5419. 14 (2021) 5419. https://doi.org/10.3390/EN14175419.

[15] A. Richelli, L. Colalongo, S. Tonoli, Z.M. Kovács-Vajna, A 0.2-1.2 V DC/DC boost converter for power harvesting applications, IEEE Trans. Power Electron. 24 (2009) 1541–1546. https://doi.org/10.1109/TPEL.2009.2013224.

[16] H.S. Hirsh, Y. Li, D.H. S Tan, M. Zhang, E. Zhao, Y. Shirley Meng, Sodium-Ion Batteries Paving the Way for Grid Energy Storage, Adv. Energy Mater. 10 (2020) 2001274. https://doi.org/10.1002/AENM.202001274.

[17] A. Ponrouch, D. Monti, A. Boschin, B. Steen, P. Johansson, M.R. Palacín, Non-aqueous electrolytes for sodium-ion batteries, J. Mater. Chem. A. 3 (2014) 22–42. https://doi.org/10.1039/C4TA04428B.

[18] E. Commission, I. Directorate-General for Internal Market Entrepreneurship and SMEs, M. Grohol, C. Veeh, Study on the critical raw materials for the EU 2023 – Final report, Publications Office of the European Union, 2023. https://doi.org/doi/10.2873/725585.

[19] BloombergNEF, Electric Vehicle Outlook 2023, 2023.

[20] L. Suo, O. Borodin, T. Gao, M. Olguin, J. Ho, X. Fan, C. Luo, C. Wang, K. Xu, "Water-in-salt" electrolyte enables high-voltage aqueous lithium-ion chemistries, Science (80-.). 350 (2015) 938–943. https://doi.org/10.1126/science.aab1595.

[21] Oxford Dictionary of English, Oxford Dict. English. (2010). https://doi.org/10.1093/ACREF/9780199571123.001.0001.

[22] A.J. Bard, L.R. Faulkner, H.S. White, Electrochemical methods : fundamentals and applications, 3rd editio, 2022.

[23] electrode potential, E, IUPAC Compend. Chem. Terminol. (2008). https://doi.org/10.1351/GOLDBOOK.E01956.

[24] redox potential, IUPAC Compend. Chem. Terminol. (2008). https://doi.org/10.1351/GOLDBOOK.RT06783.

[25] A. Rudola, A.J.R. Rennie, R. Heap, S.S. Meysami, A. Lowbridge, F. Mazzali, R. Sayers, C.J. Wright, J. Barker, Commercialisation of high energy density sodium-ion batteries: Faradion's journey and outlook, J. Mater. Chem. A. 9 (2021) 8279–8302. https://doi.org/10.1039/D1TA00376C.

[26] K. Krishnamoorthy, P. Pazhamalai, S. Sahoo, J.H. Lim, K.H. Choi, S.J. Kim, A High-Energy Aqueous Sodium-Ion Capacitor with Nickel Hexacyanoferrate and Graphene Electrodes, ChemElectroChem. 4 (2017) 3302–3308. https://doi.org/10.1002/celc.201700690.

[27] A. González, E. Goikolea, J.A. Barrena, R. Mysyk, Review on supercapacitors: Technologies and materials, Renew. Sustain. Energy Rev. 58 (2016) 1189–1206. https://doi.org/10.1016/J.RSER.2015.12.249.

[28] B. Zhao, D. Chen, X. Xiong, B. Song, R. Hu, Q. Zhang, B.H. Rainwater, G.H. Waller, D. Zhen, Y. Ding, Y. Chen, C. Qu, D. Dang, C.P. Wong, M. Liu, A high-energy, long cycle-life hybrid supercapacitor based on graphene composite electrodes, Energy Storage Mater. 7 (2017) 32–39. https://doi.org/10.1016/J.ENSM.2016.11.010.

[29] N. Yabuuchi, K. Kubota, M. Dahbi, S. Komaba, Research development on sodium-ion batteries, Chem. Rev. 114 (2014) 11636–11682. https://doi.org/10.1021/cr500192f.

[30] K. Chayambuka, G. Mulder, D.L. Danilov, P.H.L. Notten, Sodium-Ion Battery Materials and Electrochemical Properties Reviewed, Adv. Energy Mater. 8 (2018) 1800079. https://doi.org/10.1002/aenm.201800079.

[31] A. Rudola, A.J.R. Rennie, R. Heap, S.S. Meysami, A. Lowbridge, F. Mazzali, R. Sayers, C.J. Wright, J. Barker, Commercialisation of high energy density sodium-ion batteries: Faradion's journey and outlook, J. Mater. Chem. A. 9 (2021) 8279–8302. https://doi.org/10.1039/D1TA00376C.

[32] Smart Sodium Storage System - Australian Renewable Energy Agency (ARENA), (2016). https://arena.gov.au/projects/smart-sodium-storage-system-for-renewable-energy-storage/ (accessed December 2, 2021).

[33] Z. Nannan, China First Demonstrates the 100 kWh Na-Ion Battery System for Energy Storage, Chinese Acad. Sci. (2019). https://english.cas.cn/newsroom/research_news/201904/t20190401_207399.shtml (accessed December 2, 2021).

[34] Y. Cao, L. Xiao, W. Wang, D. Choi, Z. Nie, J. Yu, L. V. Saraf, Z. Yang, J. Liu, Reversible Sodium Ion Insertion in Single Crystalline Manganese Oxide Nanowires with Long Cycle Life, Adv. Mater. 23 (2011) 3155–3160. https://doi.org/10.1002/ADMA.201100904.

[35] A. Rudola, C.J. Wright, J. Barker, Reviewing the Safe Shipping of Lithium-Ion and Sodium-Ion Cells: A Materials Chemistry Perspective, Energy Mater. Adv. 2021 (2021). https://doi.org/10.34133/2021/9798460.

[36] A. Bauer, J. Song, S. Vail, W. Pan, J. Barker, Y. Lu, The Scale-up and Commercialization of Nonaqueous Na-Ion Battery Technologies, Adv. Energy Mater. 8 (2018) 1702869. https://doi.org/10.1002/aenm.201702869.

[37] R. Mogensen, A. Buckel, S. Colbin, R. Younesi, A Wide-Temperature-Range, Low-Cost, Fluorine-Free Battery Electrolyte Based on Sodium Bis(Oxalate)Borate, Chem. Mater. 33 (2021) 1130–1139. https://doi.org/10.1021/ACS.CHEMMATER.0C03570.

[38] S.E. Sloop, J.K. Pugh, S. Wang, J.B. Kerr, K. Kinoshita, Chemical Reactivity of PF_5 and $LiPF_6$ in Ethylene Carbonate/Dimethyl Carbonate Solutions, Electrochem. Solid-State Lett. 4 (2001) A42. https://doi.org/10.1149/1.1353158.

[39] G.L. Henriksen, K. Amine, J. Liu, Materials cost evaluation report for high-power Li-ion batteries., Argonne, IL (United States), 2003. https://doi.org/10.2172/808426.

[40] W. Li, J.R. Dahn, D.S. Wainwright, Rechargeable Lithium Batteries with Aqueous Electrolytes, Science (80-.). 264 (1994) 1115–1118. https://doi.org/10.1126/SCIENCE.264.5162.1115.

[41] D. Pahari, S. Puravankara, Greener, Safer, and Sustainable Batteries: An Insight into Aqueous Electrolytes for Sodium-Ion Batteries, ACS Sustain. Chem. Eng. 8 (2020) 10613–10625. https://doi.org/10.1021/acssuschemeng.0c02145.

[42] Y. Liang, Y. Yao, Designing modern aqueous batteries, Nat. Rev. Mater. 2022 82. 8 (2022) 109–122.

https://doi.org/10.1038/s41578-022-00511-3.

[43] Y. Yamada, K. Usui, K. Sodeyama, S. Ko, Y. Tateyama, A. Yamada, Hydrate-melt electrolytes for high-energy-density aqueous batteries, Nat. Energy. 1 (2016) 1–9. https://doi.org/10.1038/nenergy.2016.129.

[44] L. Droguet, A. Grimaud, O. Fontaine, J.M. Tarascon, Water-in-Salt Electrolyte (WiSE) for Aqueous Batteries: A Long Way to Practicality, Adv. Energy Mater. 10 (2020) 2002440. https://doi.org/10.1002/AENM.202002440.

[45] T. Liang, R. Hou, Q. Dou, H. Zhang, X. Yan, T.T. Liang, R.L. Hou, Q.Y. Dou, X.B. Yan, H. Zhang, H.Z. Zhang, The Applications of Water-in-Salt Electrolytes in Electrochemical Energy Storage Devices, Adv. Funct. Mater. 31 (2021) 2006749. https://doi.org/10.1002/ADFM.202006749.

[46] D.P. Leonard, Z. Wei, G. Chen, F. Du, X. Ji, Water-in-Salt Electrolyte for Potassium-Ion Batteries, ACS Energy Lett. 3 (2018) 373–374. https://doi.org/10.1021/acsenergylett.8b00009.

[47] M.R. Lukatskaya, J.I. Feldblyum, D.G. Mackanic, F. Lissel, D.L. Michels, Y. Cui, Z. Bao, Concentrated mixed cation acetate "water-in-salt" solutions as green and low-cost high voltage electrolytes for aqueous batteries, Energy Environ. Sci. 11 (2018) 2876–2883. https://doi.org/10.1039/c8ee00833g.

[48] J. Han, H. Zhang, A. Varzi, S. Passerini, Fluorine-Free Water-in-Salt Electrolyte for Green and Low-Cost Aqueous Sodium-Ion Batteries, ChemSusChem. 11 (2018) 3704–3707. https://doi.org/10.1002/cssc.201801930.

[49] C. Zhang, J. Holoubek, X. Wu, A. Daniyar, L. Zhu, C. Chen, D.P. Leonard, I.A. Rodríguez-Pérez, J.X. Jiang, C. Fang, X. Ji, A ZnCl2 water-in-salt electrolyte for a reversible Zn metal anode, Chem. Commun. 54 (2018) 14097–14099. https://doi.org/10.1039/C8CC07730D.

[50] F. Hofmeister, Zur Lehre von der Wirkung der Salze - Dritte Mittheilung, Arch. Für Exp. Pathol. Und Pharmakologie. 25 (1888) 1–30. https://doi.org/10.1007/BF01838161/METRICS.

[51] B. Hribar, N.T. Southall, V. Vlachy, K.A. Dill, How ions affect the structure of water, J. Am. Chem. Soc. 124 (2002) 12302–12311. https://doi.org/10.1021/JA026014H.

[52] A.S. Thomas, A.H. Elcock, Molecular dynamics simulations of hydrophobic associations in aqueous salt solutions indicate a connection between water hydrogen bonding and the hofmeister effect, J. Am. Chem. Soc. 129 (2007) 14887–14898. https://doi.org/10.1021/JA073097Z/.

[53] Y. Marcus, Effect of ions on the structure of water: Structure making and breaking, Chem. Rev. 109 (2009) 1346–1370. https://doi.org/10.1021/CR8003828/.

[54] P. Jungwirth, P.S. Cremer, Beyond Hofmeister, Nat. Chem. 2014 64. 6 (2014) 261–263. https://doi.org/10.1038/nchem.1899.

[55] H. Ao, C. Chen, Z. Hou, W. Cai, M. Liu, Y. Jin, X. Zhang, Y. Zhu, Y. Qian, Electrolyte solvation structure manipulation enables safe and stable aqueous sodium ion batteries, J. Mater. Chem. A. 8 (2020) 14190–14197. https://doi.org/10.1039/D0TA04800C.

[56] J. Zhang, C. Cui, P.F. Wang, Q. Li, L. Chen, F. Han, T. Jin, S. Liu, H. Choudhary, S.R. Raghavan, N. Eidson, A. Von Cresce, L. Ma, J. Uddin, D. Addison, C. Yang, C. Wang, "Water-in-salt" polymer electrolyte for Li-ion batteries, Energy Environ. Sci. 13 (2020) 2878–2887. https://doi.org/10.1039/d0ee01510e.

[57] X. He, B. Yan, X. Zhang, Z. Liu, D. Bresser, J. Wang, R. Wang, X. Cao, Y. Su, H. Jia, C.P. Grey, H. Frielinghaus, D.G. Truhlar, M. Winter, J. Li, E. Paillard, Fluorine-free water-in-ionomer electrolytes for sustainable lithium-ion batteries, Nat. Commun. 9 (2018) 1–8. https://doi.org/10.1038/s41467-018-07331-6.

[58] J. Zhao, J. Zhang, W. Yang, B. Chen, Z. Zhao, H. Qiu, S. Dong, X. Zhou, G. Cui, L. Chen, "Water-in-deep eutectic solvent" electrolytes enable zinc metal anodes for rechargeable aqueous batteries, Nano Energy. 57 (2019) 625–634. https://doi.org/10.1016/J.NANOEN.2018.12.086.

[59] J. Xie, Z. Liang, Y.C. Lu, Molecular crowding electrolytes for high-voltage aqueous batteries, Nat. Mater. 2020 199. 19 (2020) 1006–1011. https://doi.org/10.1038/s41563-020-0667-y.

[60] J. Hao, L. Yuan, C. Ye, D. Chao, K. Davey, Z. Guo, S.Z. Qiao, Boosting Zinc Electrode Reversibility in Aqueous Electrolytes by Using Low-Cost Antisolvents, Angew. Chemie Int. Ed. 60 (2021) 7366–7375. https://doi.org/10.1002/ANIE.202016531.

[61] H. Bi, X. Wang, H. Liu, Y. He, W. Wang, W. Deng, X. Ma, Y. Wang, W. Rao, Y. Chai, H. Ma, R. Li, J. Chen, Y. Wang, M. Xue, H. Bi, X. Wang, H. Liu, Y. Chai, H. Ma, M. Xue, Y. He, X. Ma, Y. Wang, W. Wang, W. Deng, R. Li, W. Rao, J. Chen, A Universal Approach to Aqueous Energy Storage via Ultralow-Cost Electrolyte with Super-Concentrated Sugar as Hydrogen-Bond-Regulated Solute, Adv. Mater. 32 (2020) 2000074. https://doi.org/10.1002/ADMA.202000074.

[62] J. Xu, X. Ji, J. Zhang, C. Yang, P. Wang, S. Liu, K. Ludwig, F. Chen, P. Kofinas, C. Wang, Aqueous electrolyte design for super-stable 2.5 V LiMn2O4 || Li4Ti5O12 pouch cells, Nat. Energy 2022 72. 7 (2022) 186–193. https://doi.org/10.1038/s41560-021-00977-5.

[63] Y. Wang, T. Ou, Y. Dong, L. Chen, Y. Huang, D. Sun, W. Qiang, X. Pei, Y. Li, Y. Tan, A Green Asymmetric Bicyclic Co-Solvent Molecule for High-Voltage Aqueous Lithium-Ion Batteries, Adv. Mater. (2024) 2311009. https://doi.org/10.1002/ADMA.202311009.

[64] Y. Sun, Z. Xu, X. Xu, Y. Nie, J. Tu, A. Zhou, J. Zhang, L. Qiu, F. Chen, J. Xie, T. Zhu, X. Zhao, Low-cost and long-life Zn/Prussian blue battery using a water-in-ethanol electrolyte with a normal salt concentration, Energy Storage Mater. 48 (2022) 192–204. https://doi.org/10.1016/J.ENSM.2022.03.023.

[65] J.F. Whitacre, A. Tevar, S. Sharma, Na4Mn9O18 as a positive electrode material for an aqueous electrolyte sodium-ion energy storage device, Electrochem. Commun. 12 (2010) 463–466. https://doi.org/10.1016/j.elecom.2010.01.020.

[66] J.F. Whitacre, T. Wiley, S. Shanbhag, Y. Wenzhuo, A. Mohamed, S.E. Chun, E. Weber, D. Blackwood, E. Lynch-Bell, J. Gulakowski, C. Smith, D. Humphreys, An aqueous electrolyte, sodium ion functional, large format energy storage device for stationary applications, J. Power Sources. 213 (2012) 255–264. https://doi.org/10.1016/j.jpowsour.2012.04.018.

[67] L. Zhang, T. Huang, A. Yu, Carbon-coated Na3V2(PO4)3 nanocomposite as a novel high rate cathode

material for aqueous sodium ion batteries, J. Alloys Compd. 646 (2015) 522–527. https://doi.org/10.1016/J.JALLCOM.2015.05.126.

[68] D. Bin, F. Wang, A.G. Tamirat, L. Suo, Y. Wang, C. Wang, Y. Xia, Progress in Aqueous Rechargeable Sodium-Ion Batteries, Adv. Energy Mater. 8 (2018) 1703008. https://doi.org/10.1002/aenm.201703008.

[69] C.W. Mason, F. Lange, Aqueous ion battery systems using sodium vanadium phosphate stabilized by titanium substitution, ECS Electrochem. Lett. 4 (2015) A79–A82. https://doi.org/10.1149/2.0011508EEL.

[70] H. Gao, J.B. Goodenough, An Aqueous Symmetric Sodium-Ion Battery with NASICON-Structured Na3MnTi(PO4)3, Angew. Chemie - Int. Ed. 55 (2016) 12768–12772. https://doi.org/10.1002/ANIE.201606508.

[71] S. Qiu, Y. Xu, X. Wu, X. Ji, Prussian Blue Analogues as Electrodes for Aqueous Monovalent Ion Batteries, Electrochem. Energy Rev. 1 (2021) 3. https://doi.org/10.1007/s41918-020-00088-x.

[72] C. Ling, J. Chen, F. Mizuno, First-principles study of alkali and alkaline earth ion intercalation in iron hexacyanoferrate: The important role of ionic radius, J. Phys. Chem. C. 117 (2013) 21158–21165. https://doi.org/10.1021/JP4078689.

[73] X. Wu, M. Sun, S. Guo, J. Qian, Y. Liu, Y. Cao, X. Ai, H. Yang, Vacancy-Free Prussian Blue Nanocrystals with High Capacity and Superior Cyclability for Aqueous Sodium-Ion Batteries, ChemNanoMat. 1 (2015) 188–193. https://doi.org/10.1002/CNMA.201500021.

[74] M. Pasta, C.D. Wessells, N. Liu, J. Nelson, M.T. McDowell, R.A. Huggins, M.F. Toney, Y. Cui, Full open-framework batteries for stationary energy storage, Nat. Commun. 2014 51. 5 (2014) 1–9. https://doi.org/10.1038/ncomms4007.

[75] X.Y. Wu, M.Y. Sun, Y.F. Shen, J.F. Qian, Y.L. Cao, X.P. Ai, H.X. Yang, Energetic Aqueous Rechargeable Sodium-Ion Battery Based on Na2CuFe(CN)6–NaTi2(PO4)3 Intercalation Chemistry, ChemSusChem. 7 (2014) 407–411. https://doi.org/10.1002/CSSC.201301036.

[76] J. Chen, C. Liu, Z. Yu, J. Qu, C. Wang, L. Lai, L. Wei, Y. Chen, High-energy-density aqueous sodium-ion batteries enabled by chromium hexacycnochromate anodes, Chem. Eng. J. 415 (2021) 129003. https://doi.org/10.1016/J.CEJ.2021.129003.

[77] Y. Zeng, Y. Wang, Z. Huang, H. Luo, H. Tang, S. Dong, P. Luo, Nano-Ni/Co-PBA as high-performance cathode material for aqueous sodium-ion batteries, Nanotechnology. 34 (2023) 475403. https://doi.org/10.1088/1361-6528/ACF224.

[78] J. Song, L. Wang, Y. Lu, J. Liu, B. Guo, P. Xiao, J.J. Lee, X.Q. Yang, G. Henkelman, J.B. Goodenough, Removal of interstitial H2O in hexacyanometallates for a superior cathode of a sodium-ion battery, J. Am. Chem. Soc. 137 (2015) 2658–2664. https://doi.org/10.1021/JA512383B/.

[79] L. Wang, J. Song, R. Qiao, L.A. Wray, M.A. Hossain, Y. De Chuang, W. Yang, Y. Lu, D. Evans, J.J. Lee, S. Vail, X. Zhao, M. Nishijima, S. Kakimoto, J.B. Goodenough, Rhombohedral Prussian white as cathode for rechargeable sodium-ion batteries, J. Am. Chem. Soc. 137 (2015) 2548–2554. https://doi.org/10.1021/JA510347S/.

[80] L. Jiang, L. Liu, J. Yue, Q. Zhang, A. Zhou, O. Borodin, L. Suo, H. Li, L. Chen, K. Xu, Y.S. Hu, High-Voltage Aqueous Na-Ion Battery Enabled by Inert-Cation-Assisted Water-in-Salt Electrolyte, Adv. Mater. 32 (2020) 1904427. https://doi.org/10.1002/ADMA.201904427.

[81] S. Il Park, I. Gocheva, S. Okada, J. Yamaki, Electrochemical Properties of NaTi2(PO4)3 Anode for Rechargeable Aqueous Sodium-Ion Batteries, J. Electrochem. Soc. 158 (2011) A1067. https://doi.org/10.1149/1.3611434.

[82] W. Wu, J. Yan, A. Wise, A. Rutt, J.F. Whitacre, Using Intimate Carbon to Enhance the Performance of NaTi 2 (PO 4) 3 Anode Materials: Carbon Nanotubes vs Graphite, J. Electrochem. Soc. 161 (2014) A561–A567. https://doi.org/10.1149/2.059404JES.

[83] B. He, K. Yin, W. Gong, Y. Xiong, Q. Zhang, J. Yang, Z. Wang, Z. Wang, M. Chen, P. Man, P. Coquet, Y. Yao, L. Sun, L. Wei, NaTi2(PO4)3 hollow nanoparticles encapsulated in carbon nanofibers as novel anodes for flexible aqueous rechargeable sodium-ion batteries, Nano Energy. 82 (2021) 105764. https://doi.org/10.1016/J.NANOEN.2021.105764.

[84] S. Zhang, Y. Liu, Q. Han, S. He, N. Zhang, J. Yang, Development and characterization of aqueous sodium-ion hybrid supercapacitor based on NaTi2(PO4)3//activated carbon, J. Alloys Compd. 729 (2017) 850–857. https://doi.org/10.1016/j.jallcom.2017.08.256.

[85] J.Y. Luo, W.J. Cui, P. He, Y.Y. Xia, Raising the cycling stability of aqueous lithium-ion batteries by eliminating oxygen in the electrolyte, Nat. Chem. 2 (2010) 760–765. https://doi.org/10.1038/nchem.763.

[86] G. Plečkaitytė, M. Petrulevičienė, L. Staišiūnas, D. Tediashvili, J. Pilipavičius, J. Juodkazytė, L. Vilčiauskas, Understanding and mitigation of NaTi2(PO4)3 degradation in aqueous Na-ion batteries, J. Mater. Chem. A. 9 (2021) 12670–12683. https://doi.org/10.1039/D1TA01215K.

[87] Y. Liu, B.H. Zhang, S.Y. Xiao, L.L. Liu, Z.B. Wen, Y.P. Wu, A nanocomposite of MoO3 coated with PPy as an anode material for aqueous sodium rechargeable batteries with excellent electrochemical performance, Electrochim. Acta. 116 (2014) 512–517. https://doi.org/10.1016/J.ELECTACTA.2013.11.077.

[88] P. Poizot, J. Gaubicher, S. Renault, L. Dubois, Y. Liang, Y. Yao, Opportunities and Challenges for Organic Electrodes in Electrochemical Energy Storage, Chem. Rev. 120 (2020) 6490–6557. https://doi.org/10.1021/ACS.CHEMREV.9B00482.

[89] S. Muench, A. Wild, C. Friebe, B. Häupler, T. Janoschka, U.S. Schubert, Polymer-Based Organic Batteries, Chem. Rev. 116 (2016) 9438–9484. https://doi.org/10.1021/acs.chemrev.6b00070.

[90] K. Qin, J. Huang, K. Holguin, C. Luo, Recent advances in developing organic electrode materials for multivalent rechargeable batteries, Energy Environ. Sci. 13 (2020) 3950–3992. https://doi.org/10.1039/D0EE02111C.

[91] G. Harper, R. Sommerville, E. Kendrick, L. Driscoll, P. Slater, R. Stolkin, A. Walton, P. Christensen, O. Heidrich, S. Lambert, A. Abbott, K. Ryder, L. Gaines, P. Anderson, Recycling lithium-ion batteries from electric vehicles, Nat. 2019 5757781. 575 (2019) 75–86. https://doi.org/10.1038/s41586-019-1682-5.

[92] H. Long, W. Zeng, H. Wang, M. Qian, Y. Liang, Z. Wang, Self-Assembled Biomolecular 1D Nanostructures for Aqueous Sodium-Ion Battery, Adv. Sci. 5 (2018) 1700634. https://doi.org/10.1002/advs.201700634.

[93] D. Jun Kim, Y. Hwa Jung, K. Kamala Bharathi, S. Hyun Je, D. Kyung Kim, A. Coskun, J. Wook Choi, D.J. Kim, Y.H. Jung, K.K. Bharathi, D.K. Kim, S.H. Je, A. Coskun, J.W. Choi, An Aqueous Sodium Ion Hybrid Battery Incorporating an Organic Compound and a Prussian Blue Derivative, Adv. Energy Mater. 4 (2014) 1400133. https://doi.org/10.1002/AENM.201400133.

[94] R. Wang, M. Shi, L. Li, Y. Zhao, L. Zhao, C. Yan, In-situ investigation and application of cyano-substituted organic electrode for rechargeable aqueous Na-ion batteries, Chem. Eng. J. 451 (2023) 138652. https://doi.org/10.1016/J.CEJ.2022.138652.

[95] Y. Zhang, P. Nie, C. Xu, G. Xu, B. Ding, H. Dou, X. Zhang, High energy aqueous sodium-ion capacitor enabled by polyimide electrode and high-concentrated electrolyte, Electrochim. Acta. 268 (2018) 512–519. https://doi.org/10.1016/j.electacta.2018.02.125.

[96] T. Gu, M. Zhou, M. Liu, K. Wang, S. Cheng, K. Jiang, A polyimide-MWCNTs composite as high performance anode for aqueous Na-ion batteries, RSC Adv. 6 (2016) 53319–53323. https://doi.org/10.1039/c6ra09075c.

[97] W. Deng, Y. Shen, J. Qian, H. Yang, A polyimide anode with high capacity and superior cyclability for aqueous Na-ion batteries, Chem. Commun. 51 (2015) 5097–5099. https://doi.org/10.1039/c5cc00073d.

[98] X. Zhu, X. Liu, W. Deng, L. Xiao, H. Yang, Y. Cao, Perylenediimide dyes as a cheap and sustainable cathode for lithium ion batteries, Mater. Lett. 175 (2016) 191–194. https://doi.org/10.1016/J.MATLET.2016.04.038.

[99] W. Luo, M. Allen, V. Raju, X. Ji, An Organic Pigment as a High-Performance Cathode for Sodium-Ion Batteries, Adv. Energy Mater. 4 (2014) 1400554. https://doi.org/10.1002/aenm.201400554.

[100] X. Han, C. Chang, L. Yuan, T. Sun, J. Sun, Aromatic carbonyl derivative polymers as high-performance Li-ion storage materials, Adv. Mater. 19 (2007) 1616–1621. https://doi.org/10.1002/adma.200602584.

[101] M. Hara, A. Satoh, N. Takami, T. Ohsaki, Structural and Electrochemical Properties of Lithiated Polymerized Aromatics. Anodes for Lithium-Ion Cells, J. Phys. Chem. 99 (1995) 16338–16343. https://pubs.acs.org/sharingguidelines (accessed December 15, 2023).

[102] L. Jiang, Y. Lu, C. Zhao, L. Liu, J. Zhang, Q. Zhang, X. Shen, J. Zhao, X. Yu, H. Li, X. Huang, L. Chen, Y.S. Hu, Building aqueous K-ion batteries for energy storage, Nat. Energy. 4 (2019) 495–503. https://doi.org/10.1038/s41560-019-0388-0.

[103] J. Ge, L. Fan, A.M. Rao, J. Zhou, B. Lu, Surface-substituted Prussian blue analogue cathode for sustainable potassium-ion batteries, Nat. Sustain. 2021 53. 5 (2021) 225–234. https://doi.org/10.1038/s41893-021-00810-7.

[104] Z. Huang, T. Wang, X. Li, H. Cui, G. Liang, Q. Yang, Z. Chen, A. Chen, Y. Guo, J. Fan, C. Zhi, Z. Huang, T. Wang, X. Li, H. Cui, G. Liang, Q. Yang, Z. Chen, A. Chen, Y. Guo, J. Fan, C. Zhi, Small-Dipole-Molecule-Containing Electrolytes for High-Voltage Aqueous Rechargeable Batteries, Adv.

Mater. 34 (2022) 2106180. https://doi.org/10.1002/ADMA.202106180.

[105] B. Wen, C. Yang, J. Wu, J. Liu, W. Wang, J. Yang, X. Chi, Y. Liu, Water-induced 3D MgMn2O4 assisted by unique nanofluidic effect for energy-dense and durable aqueous magnesium-ion batteries, Chem. Eng. J. 435 (2022) 134997. https://doi.org/10.1016/J.CEJ.2022.134997.

[106] H. Chen, Z. Zhang, Z. Wei, G. Chen, X. Yang, C. Wang, F. Du, Use of a water-in-salt electrolyte to avoid organic material dissolution and enhance the kinetics of aqueous potassium ion batteries, Sustain. Energy Fuels. 4 (2019) 128–131. https://doi.org/10.1039/c9se00545e.

[107] X. Wang, C. Bommier, Z. Jian, Z. Li, R.S. Chandrabose, I.A. Rodríguez-Pérez, P.A. Greaney, X. Ji, Hydronium-Ion Batteries with Perylenetetracarboxylic Dianhydride Crystals as an Electrode, Angew. Chemie Int. Ed. 56 (2017) 2909–2913. https://doi.org/10.1002/anie.201700148.

[108] I.A. Rodríguez-Pérez, Y. Yuan, C. Bommier, X. Wang, L. Ma, D.P. Leonard, M.M. Lerner, R.G. Carter, T. Wu, P.A. Greaney, J. Lu, X. Ji, Mg-Ion Battery Electrode: An Organic Solid's Herringbone Structure Squeezed upon Mg-Ion Insertion, J. Am. Chem. Soc. 139 (2017) 13031–13037. https://doi.org/10.1021/jacs.7b06313.

[109] X. Yin, S. Sarkar, S. Shi, Q.A. Huang, H. Zhao, L. Yan, Y. Zhao, J. Zhang, Recent Progress in Advanced Organic Electrode Materials for Sodium-Ion Batteries: Synthesis, Mechanisms, Challenges and Perspectives, Adv. Funct. Mater. 1908445 (2020) 1–21. https://doi.org/10.1002/adfm.201908445.

[110] D. Bresser, D. Buchholz, A. Moretti, A. Varzi, S. Passerini, Alternative binders for sustainable electrochemical energy storage – the transition to aqueous electrode processing and bio-derived polymers, Energy Environ. Sci. 11 (2018) 3096–3127. https://doi.org/10.1039/C8EE00640G.

[111] S.H. Farjana, N. Huda, M.A. Parvez Mahmud, R. Saidur, A review on the impact of mining and mineral processing industries through life cycle assessment, J. Clean. Prod. 231 (2019) 1200–1217. https://doi.org/10.1016/J.JCLEPRO.2019.05.264.

[112] S. V. Joshi, L.T. Drzal, A.K. Mohanty, S. Arora, Are natural fiber composites environmentally superior to glass fiber reinforced composites?, Compos. Part A Appl. Sci. Manuf. 35 (2004) 371–376. https://doi.org/10.1016/J.COMPOSITESA.2003.09.016.

[113] H.J. Becker, Low voltage electrolytic capacitor, US2800616A, 1954.

[114] H. Lu, X.S. Zhao, Biomass-derived carbon electrode materials for supercapacitors, Sustain. Energy Fuels. 1 (2017) 1265–1281. https://doi.org/10.1039/C7SE00099E.

[115] S. Lindberg, N.M. Ndiaye, N. Manyala, P. Johansson, A. Matic, A VO2 based hybrid super-capacitor utilizing a highly concentrated aqueous electrolyte for increased potential window and capacity, Electrochim. Acta. 345 (2020) 136225. https://doi.org/10.1016/j.electacta.2020.136225.

[116] X. Dong, H. Yu, Y. Ma, J.L. Bao, D.G. Truhlar, Y. Wang, Y. Xia, All-Organic Rechargeable Battery with Reversibility Supported by "Water-in-Salt" Electrolyte, Chem. – A Eur. J. 23 (2017) 2560–2565. https://doi.org/10.1002/CHEM.201700063.

[117] Q. Zhang, C. Liao, T. Zhai, H. Li, A High Rate 1.2V Aqueous Sodium-ion Battery Based on All NASICON Structured NaTi2(PO4)3 and Na3V2(PO4)3, Electrochim. Acta. 196 (2016) 470–478.

https://doi.org/10.1016/J.ELECTACTA.2016.03.007.

[118] T. Jin, X. Ji, P.F. Wang, K. Zhu, J. Zhang, L. Cao, L. Chen, C. Cui, T. Deng, S. Liu, N. Piao, Y. Liu, C. Shen, K. Xie, L. Jiao, C. Wang, High-Energy Aqueous Sodium-Ion Batteries, Angew. Chemie Int. Ed. 60 (2021) 11943–11948. https://doi.org/10.1002/ANIE.202017167.

[119] X. Wu, Y. Cao, X. Ai, J. Qian, H. Yang, A low-cost and environmentally benign aqueous rechargeable sodium-ion battery based on NaTi2(PO4)3-Na 2NiFe(CN)6 intercalation chemistry, Electrochem. Commun. 31 (2013) 145–148. https://doi.org/10.1016/j.elecom.2013.03.013.

[120] D. Reber, R. Grissa, M. Becker, R.-S. Kühnel, C. Battaglia, Anion Selection Criteria for Water-in-Salt Electrolytes, Adv. Energy Mater. 11 (2021) 2002913. https://doi.org/10.1002/AENM.202002913.

[121] J.M. Tarascon, W.R. McKinnon, F. Coowar, T.N. Bowmer, G. Amatucci, D. Guyomard, Synthesis Conditions and Oxygen Stoichiometry Effects on Li Insertion into the Spinel LiMn2 O 4, J. Electrochem. Soc. 141 (1994) 1421–1431. https://doi.org/https://doi.org/10.1149/1.2054941.

[122] T. Hosaka, T. Fukabori, H. Kojima, K. Kubota, S. Komaba, Effect of Particle Size and Anion Vacancy on Electrochemical Potassium Ion Insertion into Potassium Manganese Hexacyanoferrates, ChemSusChem. 14 (2021) 1166–1175. https://doi.org/10.1002/CSSC.202002628.

[123] T. Brousse, P.L. Taberna, O. Crosnier, R. Dugas, P. Guillemet, Y. Scudeller, Y. Zhou, F. Favier, D. Bélanger, P. Simon, Long-term cycling behavior of asymmetric activated carbon/MnO2 aqueous electrochemical supercapacitor, J. Power Sources. 173 (2007) 633–641. https://doi.org/10.1016/j.jpowsour.2007.04.074.

[124] P. Lemaire, T. Dargon, D. Alves Dalla Corte, O. Sel, H. Perrot, J.M. Tarascon, Making Advanced Electrogravimetry as an Affordable Analytical Tool for Battery Interface Characterization, Anal. Chem. 92 (2020) 13803–13812. https://doi.org/https://doi.org/10.1021/acs.analchem.0c02233.

[125] E. Bendadesse, A. V. Morozov, A.M. Abakumov, H. Perrot, J.M. Tarascon, O. Sel, Deciphering the Double-Layer Structure and Dynamics on a Model LixMoO3Interface by Advanced Electrogravimetric Analysis, ACS Nano. 16 (2022) 14907–14917. https://doi.org/https://doi.org/10.1021/acsnano.2c05784.

[126] K. -D Kreuer, A. Rabenau, W. Weppner, Vehicle Mechanism, A New Model for the Interpretation of the Conductivity of Fast Proton Conductors, Angew. Chemie Int. Ed. English. 21 (1982) 208–209. https://doi.org/10.1002/ANIE.198202082.

[127] P. Walden, Über organische Lösungs und Ionisierungsmittel. III. Teil: Innere Reibung und deren Zusammenhang mit dem Leitvermögen, Zeitschrift Für Phys. Chemie. 55 (1906) 207–246.

[128] C. Yang, J. Xia, C. Cui, T.P. Pollard, J. Vatamanu, A. Faraone, J.A. Dura, M. Tyagi, A. Kattan, E. Thimsen, J. Xu, W. Song, E. Hu, X. Ji, S. Hou, X. Zhang, M.S. Ding, S. Hwang, D. Su, Y. Ren, X.Q. Yang, H. Wang, O. Borodin, C. Wang, All-temperature zinc batteries with high-entropy aqueous electrolyte, Nat. Sustain. 2023 63. 6 (2023) 325–335. https://doi.org/10.1038/s41893-022-01028-x.

[129] W. Xu, E.I. Cooper, C.A. Angell, Ionic Liquids: Ion Mobilities, Glass Temperatures, and Fragilities, (2003). https://doi.org/10.1021/jp0275894.

[130] M.J. Kadhim, Estimation of the Diffusion Coefficient and Hydrodynamic Radius (Stokes Radius) for Inorganic Ions in Solution Depending on Molar Conductivity as Electro-Analytical Technique-A Rev... Estimation of the Diffusion Coefficient and Hydrodynamic Radius (Stokes Radius) for Inorganic Ions in Solution Depending on Molar Conductivity as Electro-Analytical Technique-A Review, J. Chem. Rev. 2 (2020) 182–188. https://doi.org/10.33945/SAMI/JCR.2020.3.5.

[131] P.C.F. Pau, J. 0 Berg, W.G. Mcmillan, Application of Stokes' Law to Ions in Aqueous Solution1, J. Phys. Chem. 94 (1990) 2671–2679. https://pubs.acs.org/sharingguidelines (accessed March 26, 2024).

[132] R. Heyrovská, Effective radii of alkali halide ions in aqueous solutions, crystals and in the gas phase and the interpretation of stokes radii, Chem. Phys. Lett. 163 (1989) 207–211. https://doi.org/10.1016/0009-2614(89)80036-3.

[133] J.R. Ferraro, K. Nakamoto, C.W. Brown, Introductory Raman Spectroscopy, (2003).

[134] Q. Sun, The Raman OH stretching bands of liquid water, Vib. Spectrosc. 51 (2009) 213–217. https://doi.org/10.1016/j.vibspec.2009.05.002.

[135] M. Thompson, J.N. Walsh, Handbook of Inductively Coupled Plasma Spectrometry, Springer US, Boston, MA, 1989. https://doi.org/10.1007/978-1-4613-0697-9.

[136] M.P.S. Mousavi, A.J. Dittmer, B.E. Wilson, J. Hu, A. Stein, P. Bühlmann, Unbiased Quantification of the Electrochemical Stability Limits of Electrolytes and Ionic Liquids, J. Electrochem. Soc. 162 (2015) A2250–A2258. https://doi.org/10.1149/2.0271512JES.

[137] J.D. Benck, B.A. Pinaud, Y. Gorlin, T.F. Jaramillo, Substrate selection for fundamental studies of electrocatalysts and photoelectrodes: Inert potential windows in acidic, neutral, and basic electrolyte, PLoS One. 9 (2014) e107942. https://doi.org/10.1371/journal.pone.0107942.

[138] F. Scholz, Electroanalytical methods: Guide to experiments and applications, Electroanal. Methods Guid. to Exp. Appl. (2010) 1–359. https://doi.org/10.1007/978-3-642-02915-8.

[139] H. Lindström, S. Södergren, A. Solbrand, H. Rensmo, J. Hjelm, A. Hagfeldt, S.E. Lindquist, Li+ ion insertion in TiO2 (anatase). 2. Voltammetry on nanoporous films, J. Phys. Chem. B. 101 (1997) 7717–7722. https://doi.org/10.1021/JP970490Q/.

[140] J.N. Scott, N. V. Nucci, J.M. Vanderkooi, Changes in water structure induced by the guanidinium cation and implications for protein denaturation, J. Phys. Chem. A. 112 (2008) 10939–10948. https://doi.org/10.1021/JP8058239.

[141] R.J. Sension, B. Hudson, P.R. Callis, Resonance raman studies of guanidinium and substituted guanidinium ions, J. Phys. Chem. 94 (1990) 4015–4025. https://doi.org/10.1021/J100373A026/.

[142] P.E. Mason, C.E. Dempsey, L. Vrbka, J. Heyda, J.W. Brady, P. Jungwirth, Specificity of ion-protein interactions: Complementary and competitive effects of tetrapropylammonium, guanidinium, sulfate, and chloride ions, J. Phys. Chem. B. 113 (2009) 3227–3234. https://doi.org/10.1021/JP8112232.

[143] C.E. Dempsey, P.E. Mason, P. Jungwirth, Complex ion effects on polypeptide conformational stability: Chloride and sulfate salts of guanidinium and tetrapropylammonium, J. Am. Chem. Soc. 133 (2011) 7300–7303. https://doi.org/10.1021/JA201349G.

[144] J. Han, M. Zarrabeitia, A. Mariani, Z. Jusys, M. Hekmatfar, H. Zhang, D. Geiger, U. Kaiser, R.J. Behm, A. Varzi, S. Passerini, Halide-free water-in-salt electrolytes for stable aqueous sodium-ion batteries, Nano Energy. 77 (2020) 105176. https://doi.org/10.1016/j.nanoen.2020.105176.

[145] L. Niu, L. Chen, J. Zhang, P. Jiang, Z. Liu, Revisiting the open-framework zinc hexacyanoferrate: The role of ternary electrolyte and sodium-ion intercalation mechanism, J. Power Sources. 380 (2018) 135–141. https://doi.org/10.1016/j.jpowsour.2018.01.083.

[146] T. Li, M. Li, H. Li, H. Zhao, High-voltage and long-lasting aqueous chlorine-ion battery by virtue of "water-in-salt" electrolyte, IScience. 24 (2021). https://doi.org/10.1016/j.isci.2020.101976.

[147] T. Hosaka, A. Noda, K. Kubota, K. Chiguchi, Y. Matsuda, K. Ida, S. Yasuno, S. Komaba, Superconcentrated NaFSA-KFSA Aqueous Electrolytes for 2 V-Class Dual-Ion Batteries, ACS Appl. Mater. Interfaces. 14 (2022) 23507–23517. https://doi.org/10.1021/ACSAMI.2C04289/.

[148] M.H. Lee, S.J. Kim, D. Chang, J. Kim, S. Moon, K. Oh, K.Y. Park, W.M. Seong, H. Park, G. Kwon, B. Lee, K. Kang, Toward a low-cost high-voltage sodium aqueous rechargeable battery, Mater. Today. 29 (2019) 26–36. https://doi.org/10.1016/j.mattod.2019.02.004.

[149] D. Reber, R. Figi, R.S. Kühnel, C. Battaglia, Stability of aqueous electrolytes based on LiFSI and NaFSI, Electrochim. Acta. 321 (2019) 134644. https://doi.org/10.1016/j.electacta.2019.134644.

[150] D. Reber, R.S. Kühnel, C. Battaglia, High-voltage aqueous supercapacitors based on NaTFSI, Sustain. Energy Fuels. 1 (2017) 2155–2161. https://doi.org/10.1039/c7se00423k.

[151] M.B. Herath, S.E. Creager, A. Kitaygorodskiy, D.D. DesMarteau, Perfluoroalkyl Phosphonic and Phosphinic Acids as Proton Conductors for Anhydrous Proton-Exchange Membranes, ChemPhysChem. 11 (2010) 2871–2878. https://doi.org/10.1002/cphc.201000184.

[152] A. Dave, K.L. Gering, J.M. Mitchell, J. Whitacre, V. Viswanathan, Benchmarking Conductivity Predictions of the Advanced Electrolyte Model (AEM) for Aqueous Systems, J. Electrochem. Soc. 167 (2020) 013514. https://doi.org/10.1149/2.0142001jes.

[153] Q. Zheng, S. Miura, K. Miyazaki, S. Ko, E. Watanabe, M. Okoshi, C. Chou, Y. Nishimura, H. Nakai, T. Kamiya, T. Honda, J. Akikusa, Y. Yamada, A. Yamada, Sodium- and Potassium-Hydrate Melts Containing Asymmetric Imide Anions for High-Voltage Aqueous Batteries, Angew. Chemie Int. Ed. 58 (2019) 14202–14207. https://doi.org/10.1002/anie.201908830.

[154] M. Mclin, C.A. Angelí, Contrasting Conductance/Viscosity Relations in Liquid States of Vitreous and Polymer "Solid" Electrolytes, 1988. https://pubs.acs.org/sharingguidelines (accessed February 19, 2021).

[155] S. Burikov, T. Dolenko, S. Patsaeva, Y. Starokurov, V. Yuzhakov, Raman and IR spectroscopy research on hydrogen bonding in water-ethanol systems, Mol. Phys. 108 (2010) 2427–2436. https://doi.org/10.1080/00268976.2010.516277.

[156] M.M. Huie, D.C. Bock, E.S. Takeuchi, A.C. Marschilok, K.J. Takeuchi, Cathode materials for magnesium and magnesium-ion based batteries, Coord. Chem. Rev. 287 (2015) 15–27. https://doi.org/10.1016/J.CCR.2014.11.005.

[157] A.J. Fernández-Ropero, M.J. Piernas-Muñoz, E. Castillo-Martínez, T. Rojo, M. Casas-Cabanas, Electrochemical characterization of NaFe2(CN)6 Prussian Blue as positive electrode for aqueous sodium-ion batteries, Electrochim. Acta. 210 (2016) 352–357. https://doi.org/10.1016/J.ELECTACTA.2016.05.176.

[158] L. Zhou, Z. Yang, C. Li, B. Chen, Y. Wang, L. Fu, Y. Zhu, X. Liu, Y. Wu, Prussian blue as positive electrode material for aqueous sodium-ion capacitor with excellent performance, RSC Adv. 6 (2016) 109340–109345. https://doi.org/10.1039/c6ra21500a.

[159] S. Khalid, N. Pianta, S. Bonizzoni, P. Mustarelli, R. Ruffo, The properties of highly concentrated aqueous CH3COOK/Na binary electrolyte and its use in sodium-ion batteries, (2021). https://doi.org/10.26434/CHEMRXIV-2021-1JXXP.

[160] J. Yue, L. Lin, L. Jiang, Q. Zhang, Y. Tong, L. Suo, Y. Hu, H. Li, X. Huang, L. Chen, Interface Concentrated-Confinement Suppressing Cathode Dissolution in Water-in-Salt Electrolyte, Adv. Energy Mater. 10 (2020) 2000665. https://doi.org/10.1002/aenm.202000665.

[161] A. Nimkar, K. Alam, G. Bergman, M.D. Levi, D.T. Major, N. Shpigel, D. Aurbach, Is 'Water in Salt' Electrolytes the Ultimate Solution? Achieving High Stability of Organic Anodes in Diluted Electrolyte Solutions Via a Wise Anions Selection, Angew. Chemie. (2023). https://doi.org/10.1002/ANGE.202311373.

[162] F. Rodríguez-Reinoso, The role of carbon materials in heterogeneous catalysis, Carbon N. Y. 36 (1998) 159–175. https://doi.org/10.1016/S0008-6223(97)00173-5.

[163] Y. Sun, Y. Zhang, Z. Xu, W. Gou, X. Han, M. Liu, C.M. Li, Dilute Hybrid Electrolyte for Low-Temperature Aqueous Sodium-Ion Batteries, ChemSusChem. 15 (2022) e202201362. https://doi.org/10.1002/CSSC.202201362.

[164] X. Wu, Y. Qi, J.J. Hong, Z. Li, A.S. Hernandez, X. Ji, Rocking-Chair Ammonium-Ion Battery: A Highly Reversible Aqueous Energy Storage System, Angew. Chemie Int. Ed. 56 (2017) 13026–13030. https://doi.org/10.1002/ANIE.201707473.

[165] T. Hosaka, R. Takahashi, K. Kubota, R. Tatara, Y. Matsuda, K. Ida, K. Kuba, S. Komaba, Origin of enhanced capacity retention of aqueous potassium-ion batteries using monohydrate-melt electrolyte, J. Power Sources. 548 (2022) 232096. https://doi.org/10.1016/J.JPOWSOUR.2022.232096.

[166] K. il Kim, L. Tang, J.M. Muratli, C. Fang, X. Ji, A Graphite‖PTCDI Aqueous Dual-Ion Battery, ChemSusChem. 15 (2022) e202102394. https://doi.org/10.1002/CSSC.202102394.

[167] Z. Huang, Y. Hou, T. Wang, Y. Zhao, G. Liang, X. Li, Y. Guo, Q. Yang, Z. Chen, Q. Li, L. Ma, J. Fan, C. Zhi, Manipulating anion intercalation enables a high-voltage aqueous dual ion battery, Nat. Commun. 2021 121. 12 (2021) 1–11. https://doi.org/10.1038/s41467-021-23369-5.

[168] N. Liu, X. Wu, Y. Zhang, Y. Yin, C. Sun, Y. Mao, L. Fan, N. Zhang, N. Liu, X. Wu, Y. Zhang, Y. Yin, C. Sun, Y. Mao, L. Fan, N. Zhang, Building High Rate Capability and Ultrastable Dendrite-Free Organic Anode for Rechargeable Aqueous Zinc Batteries, Adv. Sci. 7 (2020) 2000146. https://doi.org/10.1002/ADVS.202000146.

[169] Y. Li, H. Liu, J. Zang, W. Wang, Ionic Competition between Na+ and H+ in Aqueous Sodium-Ion

Battery Electrolytes, ACS Appl. Mater. Interfaces. 16 (2023) 4826. https://doi.org/10.1021/ACSAMI.3C16856.

[170] S. Qiu, X. Wu, M. Wang, M. Lucero, Y. Wang, J. Wang, Z. Yang, W. Xu, Q. Wang, M. Gu, J. Wen, Y. Huang, Z.J. Xu, Z. Feng, NASICON-type Na3Fe2(PO4)3 as a low-cost and high-rate anode material for aqueous sodium-ion batteries, Nano Energy. 64 (2019) 103941. https://doi.org/10.1016/J.NANOEN.2019.103941.

[171] K. Nakamoto, R. Sakamoto, Y. Sawada, M. Ito, S. Okada, K. Nakamoto, M. Ito, S. Okada, R. Sakamoto, Y. Sawada, Over 2 V Aqueous Sodium-Ion Battery with Prussian Blue-Type Electrodes, Small Methods. 3 (2019) 1800220. https://doi.org/10.1002/SMTD.201800220.

[172] K. Nakamoto, R. Sakamoto, M. Ito, A. Kitajou, S. Okada, Effect of Concentrated Electrolyte on Aqueous Sodium-ion Battery with Sodium Manganese Hexacyanoferrate Cathode, Artic. Electrochem. 85 (2017) 179–185. https://doi.org/10.5796/electrochemistry.85.179.

[173] H. Li, W. Zhang, K. Sun, J. Guo, K. Yuan, J. Fu, T. Zhang, X. Zhang, H. Long, Z. Zhang, Y. Lai, H. Sun, Manganese-Based Materials for Rechargeable Batteries beyond Lithium-Ion, Adv. Energy Mater. 11 (2021) 2100867. https://doi.org/10.1002/AENM.202100867.

[174] W. Li, C. Han, W. Wang, Q. Xia, S. Chou, Q. Gu, B. Johannessen, H. Liu, S. Dou, W. Li, C. Han, W. Wang, Q. Xia, S. Chou, H. Liu, S. Dou, Q. Gu, B. Johannessen, Stress Distortion Restraint to Boost the Sodium Ion Storage Performance of a Novel Binary Hexacyanoferrate, Adv. Energy Mater. 10 (2020) 1903006. https://doi.org/10.1002/AENM.201903006.

[175] H. Le Chatelier, On a general statement of the laws of chemical equilibrium, Comptes Rendus. 99 (1884) 786–789.

[176] H. Tokoro, S. Miyashita, K. Hashimoto, S.-I. Ohkoshi, Huge thermal hysteresis loop and a hidden stable phase in a charge-transfer phase transition of Rb 0.64 Mn †Fe"CN… 6 ‡ 0.88 · 1.7H 2 O, Phys. Rev. B. 73 (1724). https://doi.org/10.1103/PhysRevB.73.172415.

[177] A.I. Komayko, S. V. Ryazantsev, I.A. Trussov, N.A. Arkharova, D.E. Presnov, E.E. Levin, V.A. Nikitina, The Misconception of Mg2+ Insertion into Prussian Blue Analogue Structures from Aqueous Solution, ChemSusChem. 14 (2021) 1574–1585. https://doi.org/10.1002/CSSC.202002916.

[178] F.M. Alcorn, K.L. Kuntz, D.L. Druffel, S.C. Warren, Aqueous Intercalation of Graphite at a Near-Neutral pH, ACS Appl. Energy Mater. 1 (2018) 5062–5067. https://doi.org/10.1021/ACSAEM.8B01101/.

[179] G. Zhou, L. Mo, C. Zhou, Y. Wu, F. Lai, Y. Lv, J. Ma, Y.E. Miao, T. Liu, Ultra-strong capillarity of bioinspired micro/nanotunnels in organic cathodes enabled high-performance all-organic sodium-ion full batteries, Chem. Eng. J. 420 (2021) 127597. https://doi.org/10.1016/J.CEJ.2020.127597.

[180] X. Lei, Y. Zheng, F. Zhang, Y. Wang, Y. Tang, Highly stable magnesium-ion-based dual-ion batteries based on insoluble small-molecule organic anode material, Energy Storage Mater. 30 (2020) 34–41. https://doi.org/10.1016/J.ENSM.2020.04.025.

[181] J. Chen, S. Gu, R. Hao, K. Liu, Z. Wang, Z. Li, H. Yuan, H. Guo, K. Zhang, Z. Lu, Unraveling the Role of Aromatic Ring Size in Tuning the Electrochemical Performance of Small-Molecule Imide

Cathodes for Lithium-Ion Batteries, ACS Appl. Mater. Interfaces. 14 (2022) 44330–44337. https://doi.org/https://doi.org/10.1021/acsami.2c11138.

[182] P. Zhao, Y. Feng, T. Li, B. Li, L. Hu, K. Sun, C. Bao, S. Xiong, A. Matic, J. Song, Stable lithium metal anode enabled by high-dimensional lithium deposition through a functional organic substrate, Energy Storage Mater. 33 (2020) 158–163. https://doi.org/10.1016/J.ENSM.2020.08.025.

[183] S. Wang, F. Li, A.D. Easley, J.L. Lutkenhaus, Real-time insight into the doping mechanism of redox-active organic radical polymers, Nat. Mater. 2018 181. 18 (2018) 69–75. https://doi.org/10.1038/s41563-018-0215-1.

[184] S. Varma, S.B. Rempe, Coordination numbers of alkali metal ions in aqueous solutions, Biophys. Chem. 124 (2006) 192–199. https://doi.org/10.1016/J.BPC.2006.07.002.

[185] N. Patil, A. Mavrandonakis, C. Jérôme, C. Detrembleur, N. Casado, D. Mecerreyes, J. Palma, R. Marcilla, High-performance all-organic aqueous batteries based on a poly(imide) anode and poly(catechol) cathode, J. Mater. Chem. A. 9 (2021) 505–514. https://doi.org/10.1039/D0TA09404H.

[186] Y. Zhang, Y. An, L. Wu, H. Chen, Z. Li, H. Dou, V. Murugadoss, J. Fan, X. Zhang, X. Mai, Z. Guo, Metal-free energy storage systems: combining batteries with capacitors based on a methylene blue functionalized graphene cathode, J. Mater. Chem. A. 7 (2019) 19668–19675. https://doi.org/10.1039/C9TA06734E.

[187] Yadi Zhang, Yufeng An, Bo Yin, Jiangmin Jiang, Shengyang Dong, Hui Dou, Xiaogang Zhang, A novel aqueous ammonium dual-ion battery based on organic polymers, J. Mater. Chem. A. 7 (2019) 11314–11320. https://doi.org/10.1039/C9TA00254E.

[188] M. Vikman, J. Vartiainen, I. Tsitko, P. Korhonen, Biodegradability and Compostability of Nanofibrillar Cellulose-Based Products, J. Polym. Environ. 23 (2015) 206–215. https://doi.org/10.1007/S10924-014-0694-3.

[189] C.G. VanGinkel, S. Gayton, The biodegradability and nontoxicity of carboxymethyl cellulose (DS 0.7) and intermediates, Environ. Toxicol. Chem. 15 (1996) 270–274. https://doi.org/10.1002/ETC.5620150307.

[190] K. Yapsakli, F. Çeçen, Effect of type of granular activated carbon on DOC biodegradation in biological activated carbon filters, Process Biochem. 45 (2010) 355–362. https://doi.org/10.1016/J.PROCBIO.2009.10.005.

[191] P. Arora, R.E. White, M. Doyle, Capacity Fade Mechanisms and Side Reactions in Lithium-Ion Batteries, J. Electrochem. Soc. 145 (1998) 3647–3667. https://doi.org/10.1149/1.1838857.

[192] Y. Kim, J. Lim, S. Kang, Investigation on the dissolution of Mn ions from LiMn2O4 cathode in the application of lithium ion batteries: First principle molecular orbital method, Int. J. Quantum Chem. 113 (2013) 148–154. https://doi.org/10.1002/QUA.24314.

[193] Q. Hu, H. Zhao, X. Wu, Y. Liang, A temperature-dependent hydrating structure around SO42− investigated from Raman spectroscopy, J. Raman Spectrosc. 53 (2022) 1694–1703. https://doi.org/10.1002/JRS.6348.